ALMA MATER STUDIORUM - UNIVERSITÀ DI BOLOGNA

Scuola di Scienze
Dipartimento di Fisica e Astronomia
Corso di Laurea Magistrale in Astrofisica e Cosmologia

Galaxy-galaxy strong lensing as a probe of the inner structure of galaxy clusters

TESI DI LAUREA

Presentata da:
GUIDO DAVOLI

Relatore:
Chiar.mo Prof.
MASSIMO MENEGHETTI

Co-relatore:
Dott.
CARLO GIOCOLI

Sessione I
Anno accademico 2016/2017

ALMA MATER STUDIORUM - UNIVERSITÀ DI BOLOGNA

Scuola di Scienze
Dipartimento di Fisica e Astronomia
Corso di Laurea Magistrale in Astrofisica e Cosmologia

Galaxy-galaxy strong lensing as a probe of the inner structure of galaxy clusters

GUIDO DAVOLI

Sommario

La disponibilità di osservazioni profonde di ammassi di galassie, ottenute con telescopi spaziali, ha permesso la scoperta di diversi casi di lensing forte che coinvolgono una galassia d'ammasso e una sorgente retrostante (eventi di *galaxy-galaxy strong lensing*, GGSL). Ciononostante, questo tipo di eventi sembra essere molto raro nelle più recenti simulazioni idrodinamiche di ammassi di galassie. Questo apparente contrasto fra teoria e osservazioni è uno dei motivi che ci hanno spinto ad indagare sulla fenomenologia degli eventi di GGSL negli ammassi di galassie. Inoltre, lo studio delle sottostrutture presenti negli ammassi è di fondamentale importanza per vincolare le proprietà della materia oscura. In particolare, nella presente tesi abbiamo cercato di verificare la possibile esistenza di un collegamento fra le proprietà fisiche degli ammassi di galassie e la probabilità di osservare eventi di GGSL. Abbiamo quantificato questa probabilità definendo la sezione d'urto per il GGSL. Nel corso del lavoro sono state impiegate simulazioni numeriche di lensing da ammassi di galassie, le cui proprietà rispettano le predizioni del modello cosmologico ΛCDM. Nel corso della tesi abbiamo messo in luce come alcune proprietà degli ammassi, quali la pendenza del loro profilo di densità, la funzione di distribuzione radiale e la funzione di massa delle sottostrutture influenzino la sezione d'urto. Questi risultati sono stati confermati quando abbiamo applicato la nostra procedura all'ammasso MACSJ1149. Inoltre, grazie al nostro metodo, abbiamo potuto saggiare la validità di due modelli di massa, ottenuti da un'analisi di lensing forte degli ammassi MACSJ1149 e MACSJ1206, confrontando il numero di eventi di GGSL predetti dai modelli con quelli effettivamente osservati.

Abstract

The availability of deep, space based observations of galaxy clusters led to the discovery of many strong lensing events between cluster members and background sources (galaxy-galaxy strong lensing events, GGSL). Nevertheless, this kind of events seems to be very rare in the more recent hydrodynamical simulations of galaxy clusters. This apparent contrast between theory and observations is one of the reasons which lead us to analyze the phenomenology of GGSL events in galaxy clusters. Moreover, the study of substructures in clusters is fundamental in order to constrain dark matter properties. In particular, in this thesis we investigate on the existence of a link between the physical properties of clusters and the likelihood to observe these galaxy-galaxy strong lensing (GGSL) events. We quantify this probability defining the GGSL cross-section. We pursue our goal by employing numerical simulations of lensing by clusters whose properties are in agreement with the predictions of the ΛCDM cosmological model. We find that the inner slope of the cluster mass profile, the radial distribution function and the mass function of substructures influence the GGSL cross-section. These findings are confirmed when we apply our method to the cluster MACSJ1149. Moreover, thanks to our method, we are able to check the validity of two mass models, obtained through a strong lensing analysis of the clusters MACSJ149 and MACSJ1206, comparing the number of GGSL events predicted by the models and the number of observed events.

"*Ci sono più cose in cielo e in terra, Orazio, di quante ne sogni la tua filosofia.*"

William Shakespeare, *Amleto*

Acknowledgements

I would like to thank my supervisor Massimo Meneghetti, without whose help this work would have never been possible, and my co-supervisor Carlo Giocoli, always ready to give me precious advices.

Contents

List of Figures

List of Tables

Chapter 1

Cosmology

1.1 The homogeneous Universe

Modern cosmology rests on the solid base of Einstein's Theory of General Relativity. Within this framework, gravity is the manifestation of geometrical properties of space-time, which are determined by the matter-energy content of the latter. This quantities are related by the fundamental field equation

$$R_{\mu\nu} - \frac{1}{2}Rg_{\mu\nu} = \frac{8\pi G}{c^4}T_{\mu\nu} + \Lambda g_{\mu\nu} \tag{1.1}$$

where R is the curvature scalar, $R_{\mu\nu}$, $g_{\mu\nu}$ and $T_{\mu\nu}$ are respectively the Ricci, metric and energy-momentum tensors, and Λ is the cosmological constant. The presence of the cosmological constant in the field equation is not essential, from a mathematical point of view; the physical motivation of his presence is the observed accelerated expansion of the universe, as will be clarified later. Given a particular mass-energy distribution described by $T_{\mu\nu}$ and fixed Λ is, at least in principle, possible to solve this non-linear system of equations to find out the metric tensor, namely the gravitational field.

In cosmology, we are interested in the description of the universe on large scales, much larger than the typical intergalatic distance. Nowadays, thanks to the observations of the Cosmic Microwave Background (CMB) and to the measurements of galaxies distribution, we can assert that, on such large scales (a few hundreds Mpc), the universe is homogeneous and isotropic. If we assume that our position in the universe is not special, we can say that homogeneity and isotropy are fundamental properties of the universe, valid in every point. This statement is known as the *Cosmological Principle*. Under this circumstances, it can be shown (Weinberg, 1972) that $g_{\mu\nu}$ assumes a particularly simple and symmetric form, the so-called *Friedmann-Robertson-Walker* (FRW) metric, that defines a unique form of the line element $ds^2 = g_{\mu\nu}dx^\mu dx^\nu$:

$$ds^2 = c^2dt^2 - a^2(t)\left[\frac{dr^2}{1-kr^2} + r^2(d\theta^2 + \sin^2\theta d\phi^2)\right] \tag{1.2}$$

where $a(t)$ is the *scale factor* of the universe, an unknown function of time that determines the scaling of spatial coordinates r, θ, ϕ, and k is a constant that can only have the values $+1, 0, -1$. A metric of this type describes a space-time with a constant curvature scalar R, whose value determines k. Such a symmetric universe is necessarily filled with a *perfect fluid*, described with an energy-momentum tensor of the form

$$\widetilde{T_{\mu\nu}} \equiv T_{\mu\nu} + \frac{\Lambda c^4}{8\pi G}g_{\mu\nu} = (\tilde{\rho}c^2 + \tilde{P})v_\mu v_\nu - \tilde{P}g_{\mu\nu} \tag{1.3}$$

where $\tilde{\rho} = \rho + \rho_\Lambda = \rho + \frac{\Lambda c^2}{8\pi G}$ is the effective energy density, $\tilde{P} = P + P_\Lambda = P - \frac{\Lambda c^4}{8\pi G}$ is the effective pressure and v_μ is the velocity four-vector of the fluid. The effect of the cosmological constant is adding a positive energy and a negative pressure to the cosmic fluid.

The value of k defines the constant curvature of the universe, namely his geometry. It can be shown (Weinberg, 1972) that:

- if $k = 0$, (1.2) describes a flat, infinite space;
- if $k = +1$, (1.2) describes a closed space, whose geometry is that of a 3D sphere and whose volume is finite at every instant;
- if $k = -1$, (1.2) describes an open, infinite space, whose geometry is that of a 3D hyperboloid.

The value of k is not predicted by the Einsten equations (1.1), and it must be measured with experiments.

1.1.1 The expansion of the universe

Current observations show that spectra of distant galaxies experience a cosmological *redshift*, that is the frequency ν_s at which a photon is emitted from a distant source is higher than the frequency ν_o we observe on Earth. This phenomenon is quantified by the redshift z defined as

$$z = \frac{\nu_s - \nu_o}{\nu_o} \quad \Longrightarrow \quad 1 + z = \frac{\nu_s}{\nu_o}. \tag{1.4}$$

As demonstrated in Weinberg, 1972, $1 + z$ coincides with the ratio between the scale factor at the time t_o when the photon is observed and the scale factor at the time t_s when the photon is emitted, that is

$$1 + z = \frac{\nu_s}{\nu_o} = \frac{a(t_o)}{a(t_s)}. \tag{1.5}$$

The redshift z is positive, as observed, if and only if $a(t_o) > a(t_s)$, that is if the universe is expanding ($\dot{a} > 0$). In the limit of small distances between source and observer, namely when z is small, it can be shown that holds a simple relations between the redshift of light and the proper distance of the object from which light was emitted:

$$z = H_0 d_P \tag{1.6}$$

known as *Hubble law*. $H_0 = \dot{a}(t_0)/a(t_0)$ is called *Hubble constant*, but it is only the present-day value of the Hubble parameter $H(t) = \dot{a}(t)/a(t)$. However, if z and d_p are large, the redshift-distance relation is k-dependent.

The scale factor $a(t)$ can be expressed as a power series, if $t - t_0$ is small enough:

$$a(t) = a(t_0)\left[1 + H_0(t - t_0) - \frac{1}{2}q(t_0)H_0^2(t - t_0)^2 + ...\right] \tag{1.7}$$

where $q(t)$ is called *deceleration parameter* and quantify how much the universe's expansion is decelerated or accelerated. It's given by

$$q(t) = -\frac{\ddot{a}(t)a(t)}{\dot{a}^2(t)}. \tag{1.8}$$

1.1.2 Distances in cosmology

From the FRW metric (1.2) one can define the so called *proper distance* d_P between two points in the universe as the distance measured by a "chain of observers" between the two points, at the same cosmic time t. Choosing the reference system in which $d\phi = d\theta = 0$ one has

$$|ds| = a(t)\frac{dr}{\sqrt{1-kr^2}} \tag{1.9}$$

from which one defines

$$d_P = \int_0^r \frac{a(t)dr'}{\sqrt{1-kr^2}} = a(t)f(r) \tag{1.10}$$

with

$$f(r) = \begin{cases} \arcsin(r) & k = 1 \\ r & k = 0 \\ \operatorname{arcsinh}(r) & k = 0. \end{cases} \tag{1.11}$$

The proper distance between two points measured today is the *comoving distance* $d_C = d_P(t_0) = a(t_0)f(r) = \frac{a(t_0)}{a(t)}d_P(t)$. These kind of distances are not directly measurable, because it's not possible a simultaneous measurement of all length elements between us and a distant galaxy. However, it is possible to define other kinds of distances that are, at least in principle, measurable. But, since the universe is not necessarily flat and static, these definitions do not coincide and there is not a unique definition of length intervals. They are equivalent only in the local universe, where the effect of curvature and expansion is negligible. These definitions are:

Luminosity distance d_L defined as

$$d_L \equiv \left(\frac{L}{4\pi F}\right)^{1/2} \tag{1.12}$$

where L is the luminosity of the source at r, emitting light at time t, and F is the luminous flux measured by the observer at time t_0. Due to the expansion of the universe, photons are redshifted and time intervals between their arrivals are enlarged, so the measured flux drops by a factor $(a(t)/a(t_0))^2$:

$$F = \frac{L}{4\pi a^2(t_0)r^2}\left(\frac{a(t)}{a(t_0)}\right)^2 = \frac{L}{4\pi a^2(t_0)r^2}(1+z)^{-2} \tag{1.13}$$

thus

$$d_L = a(t_0)r(1+z). \tag{1.14}$$

Angular diameter distance d_A defined as

$$d_A = \frac{D_P}{\Delta\theta} = a(t)r \tag{1.15}$$

where $D_P = a(t)r\Delta\theta$ is the proper diameter of the light source in r at time t. From this follow that

$$d_A = d_L\frac{a^2(t)}{a^2(t_0)} = \frac{d_L}{(1+z)^2}. \tag{1.16}$$

Angular diameter distance is the distance definition that is naturally used in gravitational lensing studies, as will be clarified in chapter 2.

1.1.3 Friedmann equations

Inserting (1.2) and (1.3) in (1.1) one can find the two well-known *Friedmann equations*:

$$\left(\frac{\ddot{a}}{a}\right) = -\frac{4\pi G}{3}\left(\rho + \frac{3P}{c^2}\right) + \frac{\Lambda c^2}{3} = -\frac{4\pi G}{3}\left(\tilde{\rho} + \frac{3\tilde{P}}{c^2}\right) \tag{1.17a}$$

$$\left(\frac{\dot{a}}{a}\right)^2 = \frac{8\pi G}{3}\rho - \frac{kc^2}{a^2} + \frac{\Lambda c^2}{3} = \frac{8\pi G}{3}\tilde{\rho} - \frac{kc^2}{a^2}. \tag{1.17b}$$

The previous equations are not independent: they are related by the condition of covariant conservation of the energy-momentum tensor (1.3), namely by the condition of energy conservation in the universe:

$$\widetilde{T_{\mu\nu;\nu}} = 0 \quad \Longrightarrow \quad \frac{d}{dt}\left(a^3\rho c^2\right) - P\frac{da^3}{dt} = 0. \tag{1.18}$$

Rewriting the second Friedmann equation (1.17b) in terms of the Hubble parameter and for $t = t_0$ (today) we find

$$H_0^2\left(1 - \frac{\Lambda c^2}{3H_0^2} - \frac{8\pi G\rho_0}{3H_0^2}\right) = -\frac{kc^2}{a_0^2} \tag{1.19}$$

and defining today's *critical density* of the universe as $\rho_{c,0} = \frac{3H_0^2}{8\pi G}$ we can write

$$H_0^2\left(1 - \frac{\rho_{\Lambda,0}}{\rho_{c,0}} - \frac{\rho_0}{\rho_{c,0}}\right) = -\frac{kc^2}{a_0^2}. \tag{1.20}$$

Finally, introducing today's density parameters of the i-th component as $\Omega_{i,0} = \frac{\rho_{i,0}}{\rho_{c,0}}$ we can write

$$H_0^2\left(1 - \Omega_{\Lambda,0} - \Omega_0\right) = -\frac{kc^2}{a_0^2} \tag{1.21}$$

from which is evident that the curvature of the universe and his today's energy content are related as follows:

- $k = 0 \quad \Longleftrightarrow \Omega_{\Lambda,0} + \Omega_0 = \Omega_{tot,0} = \frac{\rho_{\Lambda,0}+\rho_0}{\rho_{c,0}} = 1$
- $k = 1 \quad \Longleftrightarrow \Omega_{\Lambda,0} + \Omega_0 = \Omega_{tot,0} = \frac{\rho_{\Lambda,0}+\rho_0}{\rho_{c,0}} > 1$
- $k = -1 \Longleftrightarrow \Omega_{\Lambda,0} + \Omega_0 = \Omega_{tot,0} = \frac{\rho_{\Lambda,0}+\rho_0}{\rho_{c,0}} < 1.$

Moreover, from (1.17a) it is easy to show that

$$\Lambda c^2 > 4\pi G\left(\rho + \frac{3P}{c^2}\right) \Longleftrightarrow \ddot{a} > 0 \tag{1.22}$$

that is to say that observed accelerated expansion of the universe is made possible by a positive cosmological constant.

1.1.4 Equation of state

With the two Friedmann equations alone we aren't able to find solutions for $\rho(t), P(t), a(t)$. For this purpose it's necessary to use an equation of state describing the perfect cosmic fluid. In standard cosmology it takes the general form

$$P = w\rho c^2 \tag{1.23}$$

where the value of the *state parameter* w depends on the particular component of the fluid we are considering. Indeed,

$$w = \begin{cases} 0 & \text{pressureless, non relativistic matter ("dust")} \\ 1/3 & \text{radiation, ultra-relativistic matter} \\ -1 & \text{cosmological constant} \end{cases} \tag{1.24}$$

so, from (1.18) and (1.23) it's possible to write a single expression for ρ in terms of a and w:

$$\rho_w \propto a^{-3(1+w)} \propto (1+z)^{3(1+w)} \tag{1.25}$$

which becomes, in the three cases:

- dust-dominated universe: $w = 0 \Longrightarrow \rho_M = \rho_{M,0} \left(\frac{a_0}{a}\right)^3$
- radiation-dominated universe: $w = \frac{1}{3} \Longrightarrow \rho_R = \rho_{R,0} \left(\frac{a_0}{a}\right)^4$
- Λ-dominated universe: $w = -1 \Longrightarrow \rho_\Lambda = \rho_{\Lambda,0} \left(\frac{a_0}{a}\right)^0 = \rho_{\Lambda,0}$.

1.1.5 Present-day measured cosmological parameters

Results of the Planck experiment (Planck Collaboration et al., 2016), focused on the measurement of CMB properties, indicate that the actual value of the Hubble parameter is $H_0 = 67.8 \pm 0.9$ km s^{-1}Mpc^{-1}. This means that the present-day value of the critical density of the universe is

$$\rho_{c,0} = \frac{3H_0^2}{8\pi G} \approx 2 \cdot 10^{-29} \text{g cm}^{-3} h^2 \tag{1.26}$$

where h is given by $H_0 = 100h$ km s^{-1}Mpc^{-1}. The measured matter density parameter is $\Omega_m = 0.308 \pm 0.012$ while the curvature of the universe is strictly constrained to be $k < 0.005$, pointing out the flatness of the universe. These results are consistent with high-redshift supernovae observations (Riess et al., 1998) and with results of *COBE* and *BOOMERANG* experiments (Jaffe et al., 2001), indicating that $\Omega_\Lambda \sim 0.7$ and $q \sim -0.55$. In this work we adopt the values $\Omega_\Lambda = 0.7$, $\Omega_m = 0.3$ and $h = 0.7$.

1.1.6 Friedmann model for a flat universe

As shown in Sect. 1.1.4, the energy density of every component, having a different equation of state, has a different evolution with cosmic time. This fact makes possible to identify different epochs during the history of the universe, in which a different component was the dominant one. Boundaries of this epochs can be found imposing the equivalence of matter and radiation density and of matter and dark energy density, respectively:

- matter-radiation equivalence: $\rho_M = \rho_R$ when

$$\rho_{M,0}\left(\frac{a(t_0)}{a(t_{eq})}\right)^3 = \rho_{R,0}\left(\frac{a(t_0)}{a(t_{eq})}\right)^4 \tag{1.27}$$

$$\rho_{M,0}(1+z_{eq})^3 = \rho_{R,0}(1+z_{eq})^4 \tag{1.28}$$

$$(1+z_{eq}) = \frac{\rho_{M,0}}{\rho_{R,0}} \sim 3\cdot 10^4 \Longrightarrow z_{eq}^{MR} \sim 3\cdot 10^4; \tag{1.29}$$

- matter-Λ equivalence: $\rho_M = \rho_\Lambda$ when

$$\rho_{\Lambda,0} = \rho_{M,0}(1+z_{eq})^3 \tag{1.30}$$

$$(1+z_{eq}) = \left(\frac{\rho_{\Lambda,0}}{\rho_{M,0}}\right)^{1/3} \sim 1.7 \Longrightarrow z_{eq}^{M\Lambda} \sim 0.7. \tag{1.31}$$

This means that dark energy started to dominate our universe recently, at $z \lesssim 0.7$, while at redshifts $0.7 \lesssim z \lesssim 3\cdot 10^4$ the universe energy content was dominated by matter. Before this epoch, radiation was predominant.

Thus, as a first approximation, in this three epochs we can consider the cosmic fluid as made up of the dominant component only:

- at $z \gtrsim 3\cdot 10^4$, during the *radiation epoch*, $w_{eff} \sim 1/3$
- at $0.7 \lesssim z \lesssim 3\cdot 10^4$, during the *matter epoch*, $w_{eff} \sim 0$
- at $z \lesssim 0.7$, during the *dark energy epoch*, $w_{eff} \sim -1$.

Combining Eq. (1.17a) and (1.23) in the different epochs, one can show that an accelerated expansion of the universe is possible only in a Λ-dominated universe, while in the matter- and radiation-dominated epochs the expansion of the universe was decelerated ($\ddot{a} < 0$). This fact, together with the observational evidence of $\dot{a} > 0$, means that at $z \gtrsim 0.7$ the function $a(t)$ has negative concavity so, somewhere in the past, in correspondence of the *Big Bang*, the scale factor was null. Moreover, the age of the universe is necessarily finite and less than the *Hubble time* $H_0^{-1} = a/\dot{a}$. This is shown in fig. 1.1

In a single-component universe dominated by the element with state parameter w, Eq. (1.21) reads

$$H_0^2\left(1-\Omega_{w,0}\right) = -\frac{kc^2}{a_0^2} \tag{1.32}$$

while from the Friedmann equations and from Eq. (1.25) one obtains

$$H^2(t) = H_0^2\left(\frac{a_0}{a}\right)^2\left[1-\Omega_{w,0}+\Omega_{w,0}\left(\frac{a_0}{a}\right)^{1+3w}\right]. \tag{1.33}$$

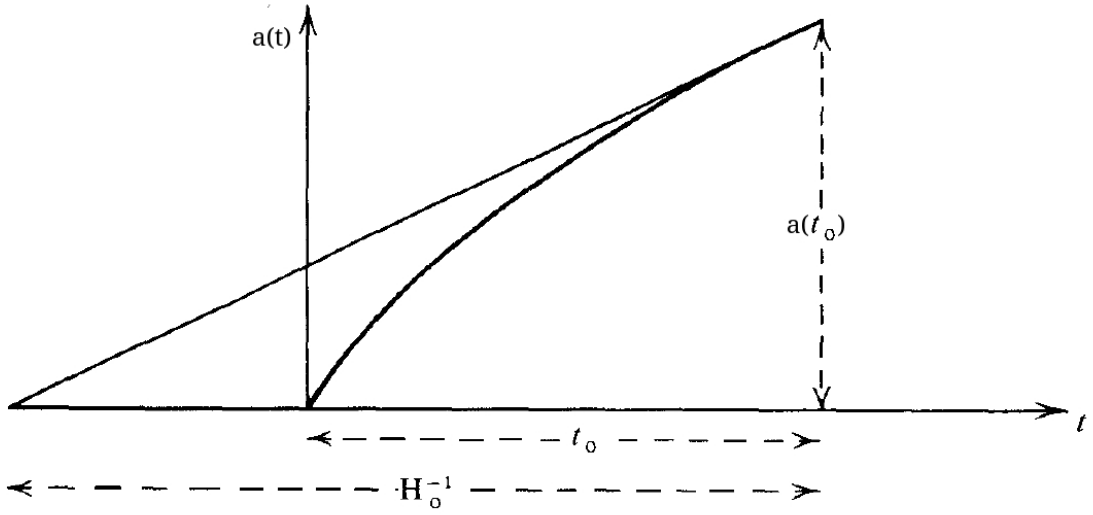

FIGURE 1.1: The concavity of a(t) ensures that there must be a singularity in the past, namely a point when a = 0. It also ensures that the age of the Universe, t_0 , is less than the Hubble time, $1/H_0$. Figure from Berry, 1989.

If such a universe is also flat ($k = 0 \leftrightarrow \rho_{w,0} = \rho_c \leftrightarrow \Omega_{w,0} = 1$), it is possible to find explicit solutions for $a(t), H(t), q(t), \rho_w(t)$, namely:

$$t_0^{-1} = H_0 \frac{3(1+w)}{s} \tag{1.34a}$$

$$a(t) = a_0 \left(\frac{t}{t_0}\right)^{\frac{2}{3(1+w)}} \tag{1.34b}$$

$$H(t) = \frac{\dot{a}}{a} = \frac{2}{3(1+w)} t^{-1} \tag{1.34c}$$

$$q(t) = -\frac{\ddot{a}a}{\dot{a}^2} = \frac{3(1+w)}{2} - 1 = \text{const.} = q_0 \tag{1.34d}$$

$$\rho_w(t) = \frac{1}{6\pi G(1+w)^2 t^2} \tag{1.34e}$$

From these relations we can conclude that, in this model, the universe undergoes an indefinite expansion, whose speed depends on w. Finally, from Eqs. (1.25), (1.33) and from the definitions of the critical density and Ω_w one obtains that

$$\Omega_w(z) = \frac{\Omega_{w,0}(1+z)^{1+3w}}{1 - \Omega_{w,0} + \Omega w, 0(1+z)^{1+3w}} \tag{1.35}$$

that is to say that if $\Omega_{w,0}$ is larger, equal or smaller than 1, then $\Omega_w(z)$ is always larger, equal or smaller than 1, even if approaching the Big Bang ($z \to \infty$), the density parameter tends to unity ($\Omega_w(z) \to 1$). The evolution of the universe cannot change its geometry.

1.2 Evolution of perturbations

1.2.1 Linear theory

Today's universe can be described as homogeneous and isotropic only on large scales. In order to describe structures observed on smaller scales, from galaxy clusters to galaxies, it is necessary to introduce inhomogeneities in our theory. *Structure formation theories* describe the evolution of primordial density fluctuation during the history of the universe.

The generation of primordial perturbations is described by the *Inflation theory*, whose predictions agree with present observations, accounting for the homogeneity, isotropy and flatness of the observable universe and for the absence of magnetic monopoles. According to this scenario, primordial density and temperature fluctuations originate from quantum effects in the early universe, slightly after the Big Bang. The growth of these small inhomogeneities of the cosmic fluid into the present observable structure of the universe can be calculated with the laws of gravity in an expanding universe.

The quantity

$$R_H(t) = a(t) \int_0^{a(t)} \frac{da'}{\dot{a}' a'(t')} \tag{1.36}$$

is called *radius of the cosmological horizon* and defines the radius of the portion of the universe that is in causal connection with the observer, namely the boundary of the observable region of the universe. This quantity is important in the study of the evolution of perturbations, since it defines a length scale under which the gravitational collapse of dark and ordinary matter can be prevented by other physical processes opposing to gravity (basically the cosmic fluid pressure). Moreover, in this regime gravitational collapse can be well described with a Newtonian theory, the so-called Jeans theory, exposed below.

In early phases of perturbations growth, when the density contrast between the mean "background" density of the universe ρ_b and the density of the perturbation ρ is small, that is when

$$\delta = \frac{\delta\rho}{\rho} = \frac{\rho - \rho_b}{\rho_b} \ll 1, \tag{1.37}$$

the gravitational collapse of inhomogeneities can be described by a linear, first-order approximation. If we do not consider the expansion of the universe, on length scales smaller than R_H the equations that describe the growth of perturbations are the continuity equation, the Euler equation, the Poisson equation and the entropy conservation:

$$\begin{cases} \frac{\partial\rho}{\partial t} + \vec{\nabla}(\rho\vec{v}) = 0 \\ \frac{\partial\vec{v}}{\partial t} + \vec{v}\vec{\nabla}\vec{v} = -\frac{1}{\rho}\vec{\nabla}P - \vec{\nabla}\phi \\ \Delta\phi = 4\pi G\rho \\ \frac{dS}{dt} = 0 \end{cases} \tag{1.38}$$

This system can be solved with constant density, pressure and gravitational potential ρ_b, P_b, ϕ_b and null velocity. Adding to this solution small perturbations $\delta\rho, \delta P, \delta\phi, \delta v$ and leaving only first-order terms in equations, one obtains

$$\begin{cases} \frac{\partial\delta\rho}{\partial t} + \rho_b\vec{\nabla}\delta\vec{v} = 0 \\ \frac{\partial\delta\vec{v}}{\partial t} = -\frac{v_s^2}{\rho_b}\vec{\nabla}\delta\rho - \vec{\nabla}\delta\phi \\ \Delta\delta\phi = 4\pi G\delta\rho\rho_b \end{cases} \tag{1.39}$$

where v_s^2 is the sound speed in adiabatic conditions, when $\delta P = v_s^2 \delta\rho$. Writing perturbations as plane waves $f(\vec{r},t) = f_k exp(i\vec{k}\vec{r} + i\omega t)$, we obtain the dispersion relation

$$\omega^2 = v_s^2 k^2 - 4\pi G\rho_b, \tag{1.40}$$

which has two real solutions for $\omega^2 > 0$, leading to the propagation of stable plane waves, and two imaginary solutions for $\omega^2 < 0$, one of which leading to an indefinite growth of perturbations. The boundary between these two regimes is given by $\omega^2 = 0$, when the perturbation is static. Recalling that $k = 2\pi\lambda$, this happens when the perturbations has a length scale equal to the *Jeans length*

$$\lambda_J = v_s\sqrt{\frac{\pi}{G\rho_b}} \tag{1.41}$$

which corresponds to a *Jeans mass*

$$M_J = \frac{4}{3}\pi\rho_b\lambda_J^3. \tag{1.42}$$

So, if the size λ of the perturbation is such that $\lambda > \lambda_J$ (or, equivalently, its mass M is greater than M_J), this perturbation can undergo gravitational collapse; otherwise it can only propagate in the universe as a stable wave.

In an expanding universe, growth of perturbations is more difficult. In this case the perturbation can be described as a closed universe contained in a flat background universe. Imposing the equivalence of their two Hubble parameters and studying the evolution with Friedmann equations, one obtains

$$\delta \propto (\rho_b a^2)^{-1} \tag{1.43}$$

so, before and after the time t_{eq} corresponding to the matter-radiation equivalence (1.29) the time dependence of the density contrast is

$$t < t_{eq} : \delta \propto a^2 \propto t \tag{1.44a}$$

$$t > t_{eq} : \delta \propto a \propto t^{2/3}. \tag{1.44b}$$

If $\lambda > R_H$, where the only relevant force is gravity, this solution refers to all components of the cosmic fluid; if $\lambda < R_H$ (and $\lambda > \lambda_J$), this solution holds only for the main component of the universe at a given time and, potentially, also for components physically coupled with the main one, with the others possibly influenced by *microphysical* processes. Rewriting Eq. (1.38) in terms of a velocity $\vec{u}$, which is the sum of the peculiar velocity of the perturbation and the expansion velocity given by the Hubble law, and using $\delta(\vec{r},t) = \delta_k(t)exp(i\vec{k}\vec{x})$, it is possible to obtain, for $t > t_{eq}$ (namely in a matter-dominated universe), the following equation for δ_k:

$$\ddot{\delta_k} + 2\dot{\delta_k}\frac{\dot{a}}{a} + \delta_k\left[k^2 v_s^2 - 4\pi G\rho_b\right] = 0 \tag{1.45}$$

which is solvable with the ansatz $\delta_k \propto t^\alpha$. When $\lambda \gg \lambda_J = \frac{v_s}{5}\sqrt{\frac{24\pi}{G\rho_b}}$, this leads to the two solutions

$$\delta_- \propto t^{-1} \propto a^{-3/2} \propto (1+z)^{3/2} \tag{1.46a}$$

$$\delta_+ \propto t^{2/3} \propto a \propto (1+z)^{-1}. \tag{1.46b}$$

For $t < t_{eq}$ (namely in a radiation-dominated universe) one finds

$$\ddot{\delta_k} + 2\dot{\delta_k}\frac{\dot{a}}{a} + \delta_k\left[k^2 v_s^2 - \frac{32}{3}\pi G\rho_b\right] = 0 \tag{1.47}$$

that, using $\delta_k \propto t^\alpha$ when $\lambda \gg \lambda_J = v_s\sqrt{\frac{3\pi}{8G\rho_b}}$, leads to

$$\delta_+ \propto t \propto a^2 \propto (1+z)^{-2}. \tag{1.48}$$

However, it can be shown that in such conditions $\lambda_J > R_H$.

Summarizing, δ_+ solutions describe the growing perturbations in a flat universe, before and after the equivalence between matter and radiation energy density. If the size of the fluctuation is greater than the cosmological horizon ($\lambda > R_H$), δ_+ describes the evolution of all components of the cosmic fluid, so

$$\lambda > R_H : \begin{cases} t < t_{eq} : & \delta \propto a^2 \propto t \text{ for all components} \\ t > t_{eq} : & \delta \propto a \propto t^{2/3} \text{ for all components} \end{cases} \tag{1.49}$$

while if $\lambda < R_H$, δ_+ describes only the evolution of perturbations of the main component of the universe:

$$\lambda < R_H \begin{cases} t < t_{eq} : & \text{no instability for radiation} \\ t > t_{eq} : \delta \propto a \propto t^{2/3} & \text{only for matter.} \end{cases} \tag{1.50}$$

Nevertheless, until the *decoupling* occurred at $z_{dec} \sim 300$, ordinary matter ("baryons") was coupled with radiation, due to frequent scattering. This means that the solution given by Eq. (1.50) holds at $t < t_{eq}$ for both radiation and baryons and at $t_{dec} > t > t_{eq}$ only for dark matter (DM), which isn't affected by radiation scattering, and holds also for ordinary matter only after, for $t > t_{dec}$. Before decoupling, as for radiation, baryons weren't able to collapse on sub-horizon scales.

The extent of dark matter perturbations before the equivalence was restricted by the *Meszaros effect* (see Peter Coles, 2002), which imposes that

$$\delta_{k,DM} = 1 + \frac{3}{2}\frac{a}{a_{eq}} \quad \Longrightarrow \quad \delta_{k,DM} \leq \frac{5}{2} \quad \text{before equivalence.} \tag{1.51}$$

After t_{eq} dark matter perturbations on sub-horizon scales grow as given by Eq. (1.50), so at decoupling, when baryons can undergo gravitational collapse, in the universe were already present dark matter potential wells. This leads to the *baryon catch-up* effect, implying that baryonic perturbations follow the dark matter ones:

$$\delta_{k,B} = \delta_{k,DM}\left(1 - \frac{a_{dec}}{a}\right) \text{ for } t > t_{dec}. \tag{1.52}$$

In a universe without dark matter this process wouldn't be possible, causing $\delta_{k,B}$ to be much smaller than observed today.

However, as seen, perturbations which do not have enough mass to collapse are propagating as density waves, under the influence of the global gravitational field. This fact causes a leveling of existing perturbations at the scale reached by dark matter perturbations traveling at speed v_s at time t, called *free streaming* scale:

$$\lambda_{FS}(t) = a(t)\int_0^t \frac{v_s dt'}{a(t')}. \tag{1.53}$$

The free streaming mass $M_{FS} \propto \lambda_{FS}^3$ grows whit time, and coincides with the Jeans mass before t_{eq}; after t_{eq}, M_{FS} remains constant and equal to $M_J(t_{eq})$. This means that at the equivalence only perturbations with mass larger than the free streaming mass are survived. The Jeans length and mass change with the evolution of the universe, because the dominant component of the cosmic fluid and the particles' velocity v_s changes. The maximum value reached by the Jeans mass during the history of the universe is the minimum mass that ensures a perturbation to continuously grow. The maximum Jeans mass is reached at t_{eq}, but its value depends on the properties of dark matter. For example, we can distinguish between Cold Dark Matter (CDM) and Hot Dark Matter (HDM) models. In CDM scenarios, the velocity of DM particles at the epoch of decoupling between radiation and matter is non-relativistic; on the contrary, in HDM scenario DM particles are lighter and their velocities at decoupling are still relativistic. Intermediate scenarios correspond to Warm Dark Matter models. The mass and velocity of DM particles have a great impact on structure formation: CDM theories predict $M_J(t_{eq}) = M_{FS}(t_{eq}) \sim 10^6 M_\odot$, smaller than the mass of lightest galaxies, while HDM theories predict $M_t(a_{eq}) = M_{FS}(t_{eq}) \sim 10^{16} M_\odot$, bigger than the mass of heaviest galaxy clusters. These different values imply that in an HDM universe the biggest structures are the oldest ones, the opposite in a CDM universe. Current observations support the CDM scenario, in which galaxies are older than galaxy clusters, the latter often observed out of equilibrium.

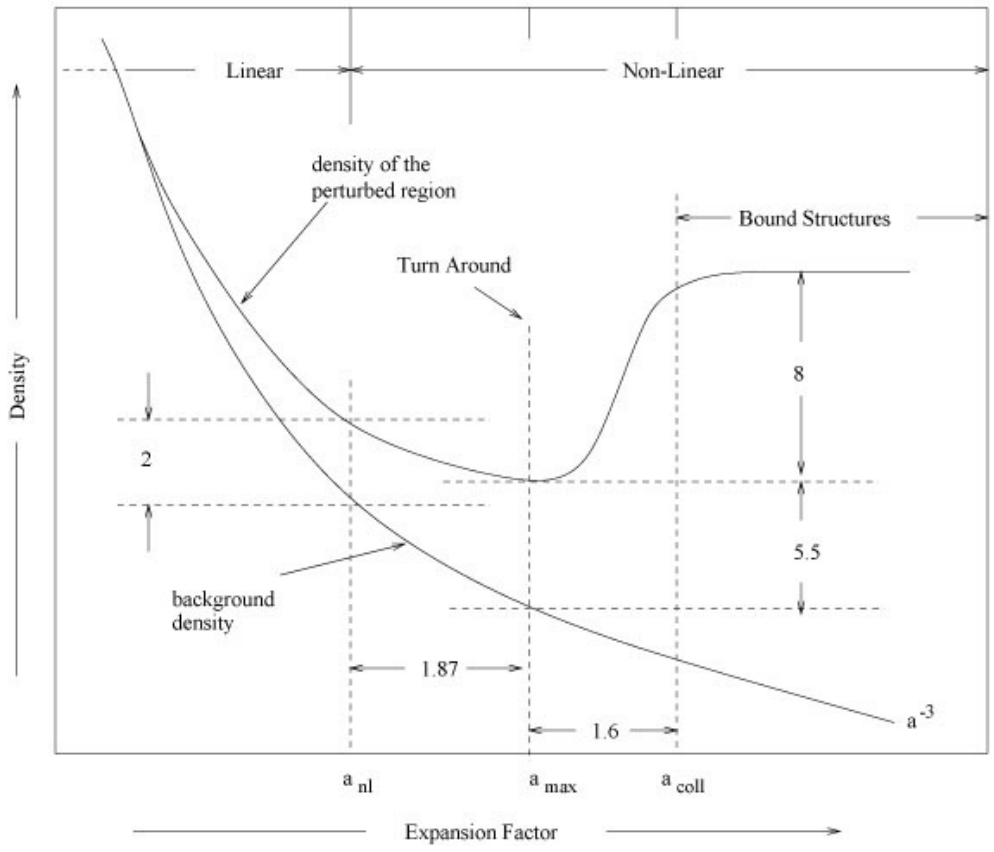

FIGURE 1.2: Density evolution of a spherical overdense region in the nonlinear regime. Figure from Padmanabhan, 2002.

1.2.2 Nonlinear theory

The assumptions used in the linear theory break down when $\delta \sim 1$. Analytical solutions for the nonlinear collapse can be found only in the simple case of a spherical perturbation, which is too simple to describe realistic structures but give us some interesting information about the collapse process. As can be seen in Fig. 1.2, initially the perturbation expands but slower than the universe, since the turn-around point is reached at time t_{max}, when $\delta(t_{max}) \sim 4.6$. Here the contraction starts, and a virialized structure is formed at t_{coll}, when $\delta(t_{coll}) \sim 400$.

For an accurate description of structure formation in this regime numerical simulations are needed. Nowadays it is possible to simulate the evolution of dark matter fluctuation during the history of the universe in large volumes (hundreds of Mpc on a side), and to identify structures whose properties are compatible with those of observed galaxies and galaxy clusters. Fig 1.3 illustrates the results of such a simulations, in which the formation of the so-called *cosmic web*, a filamentary structure connecting dense clumps of matter corresponding to cluster of galaxies, is evident.

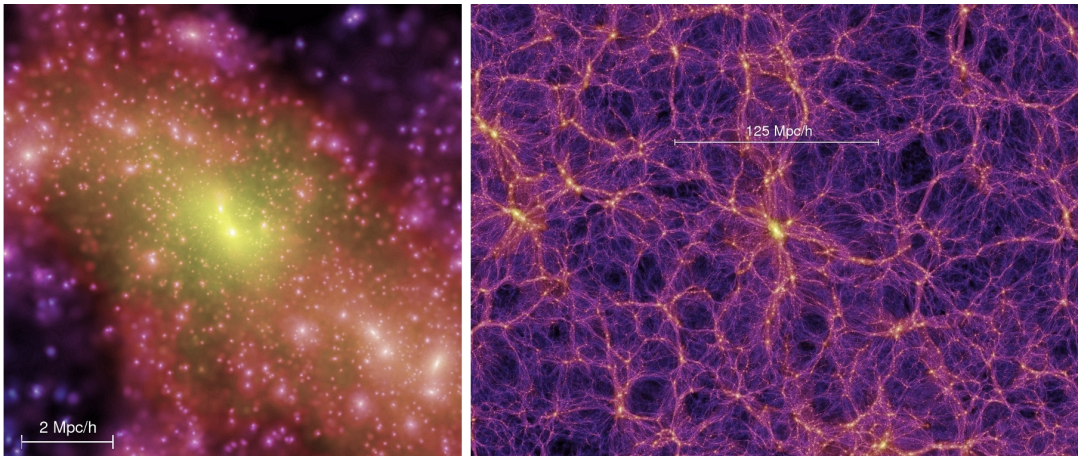

FIGURE 1.3: A snapshot from the Millennium cosmological simulation, showing the dark matter distribution at z=0 in a galaxy cluster (left) and on a larger scale (right). Figure from the Millennium Simulation website.

1.3 Problems of the ΛCDM model

The standard ΛCDM cosmological model is not exempt from problems. On galactic scale, the two main problems are the so-called *missing satellite problem* and the *cusp-core problem*.

The missing satellite problem consists in the fact that simulated galaxy-sized halos retain a large amount of substructure, predicting hundreds or thousands of subhalos. In contrast, observations in the local group show that our galaxy only have few tens of satellites. A plausible solution for this problem can be found in baryonic physics, without invoking a modification of the standard cosmological model: many halos could be dark because of the absence of star formation inside them. Effectively, the velocity threshold at which subhalo and dwarf satellite counts diverge is close to ~ 30 km/s, the value at which heating of intergalactic gas by the ultraviolet photoionizing background should suppress gas accretion onto halos, which could plausibly cause these halos to remain dark. An additional contribute to the suppression of star formation in these small haloes can be found in supernovae and stellar winds (Weinberg et al., 2015). However, comparing the most massive satellites found in simulations (the ones which one would expect to be the most luminous) with the Milky Way's observed satellites, it is found that the mass in the central regions of these subhalos exceeds the mass inferred from stellar dynamics of observed dwarfs by a factor ~ 5. Since it seems unlikely that these massive subhalos are dark and that the observed dwarfs reside in less massive hosts, this "too big to fail" problem is still unresolved with baryonic physics. This evidence suggests that simulations of ΛCDM structure formation predict too much mass in the central regions of halos and subhalos: from this point of view, the missing satellites problem looks similar to the cusp-core problem, discussed in the next paragraph.

The cusp-core problem arises fitting observed galactic rotation curves with theoretical models of the distribution of dark matter, stars and gas. NFW dark matter halos overpreditcs the rotation speed in the inner few kpc by a factor two or more with respect to isothermal models with a constant density core. Despite uncertainties in modeling and observations, it seems clear that resolving the cusp-core problem requires a modification of the halo profiles of typical spiral galaxies predicted by N-body simulations. High-resolution hydrodynamic simulations of galaxy-sized halos with star formation and feedback show that this effects, injecting energy into dark matter particles orbits, can cause the dark matter profile to drop at the centre, forming cores with nearly constant density. However, this solution needs to further observational confirmations. If not found, this problem can become another challenge to the standard ΛCDM model.

Instead of invoking the complex aforementioned baryonic solutions to the missing satellites and to the cusp-core problem, one can try to match simulations and observations modifying the hypothesis which simulations are based on: in particular, that dark matter is "cold". In fact, if dark matter is "warm", its free-streaming velocities in the early universe were large enough to erase primordial perturbations on sub-galactic scales. Thus, in such a situation, the subhalo mass function drops at low masses. The results of a simulated galaxy-sized halo in some WDM universes are depicted in fig. 1.4, in which is evident the loss of substructure at low masses in warmer scenarios.

However, this affects Lyman-α forest observations and seems to be in contrast with observations of strong lensing systems, that show evidence for a significant subhalo fraction as well as the existence of small ($\sim 10^8 M_\odot$) substructures (see Sect.

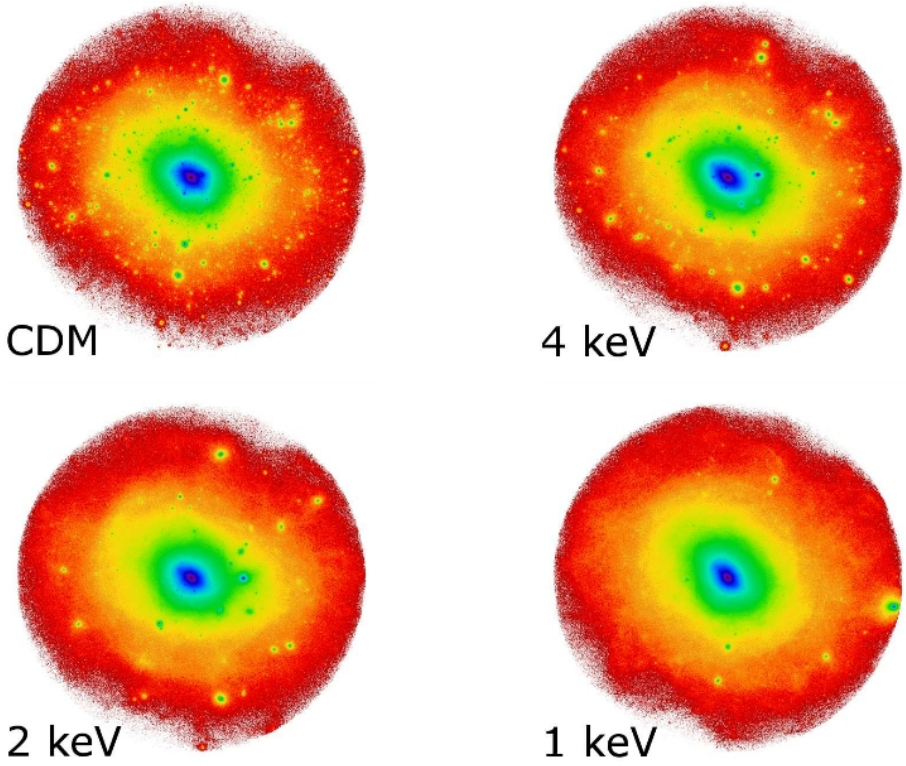

FIGURE 1.4: Portraits of a Milky Way-like halo at $z = 0$ in high resolution simulations with different dark matter particles properties. Structure within 500 kpc of the center is shown. From Polisensky and Ricotti, 2011.

3.2.2). Another possibility consists in a high dark matter self interaction (Self Interacting Dark Matter, SIDM), but current theories can resolves only the cusp-core problem leaving too much satellites around Milky Way-like galaxies. Summarizing, today doesn't exists a definitive solution to this problems, so further work is needed to find possible bugs in the current standard cosmological model. Probing substructures mass function down to small masses and investigating dark matter distribution in subhalos are promising ways to test the ΛCDM model.

Some tension between theory and observations exists also on larger scale. Grillo et al., 2015 compare the results of their strong lensing analysis of the cluster MACS0416 with simulated clusters of comparable mass extracted from high resolution cosmological simulations. They found that the inner regions of simulated clusters contains considerably less mass in substructures with respect to observations. The mismatch is particularly evident in the central 150 kpc and it corresponds to a lack of massive subhalos with circular velocities $v_c \gtrsim 100$ km/s (Fig. 1.5).

A similar result is reported in Munari et al., 2016: the number of massive ($v_c \gtrsim 200$ km/s) substructures in the inner 2.2 Mpc of the cluster Abell 2142 is significantly higher than simulations predictions (Fig. 1.6). This result is even more robust then the previous one, since the authors directly compare the outcomes of simulations and velocities measurements, without any intermediate mass calibration as for strong lensing analysis.

In Natarajan et al., 2017 the substructure population derived from the lensing

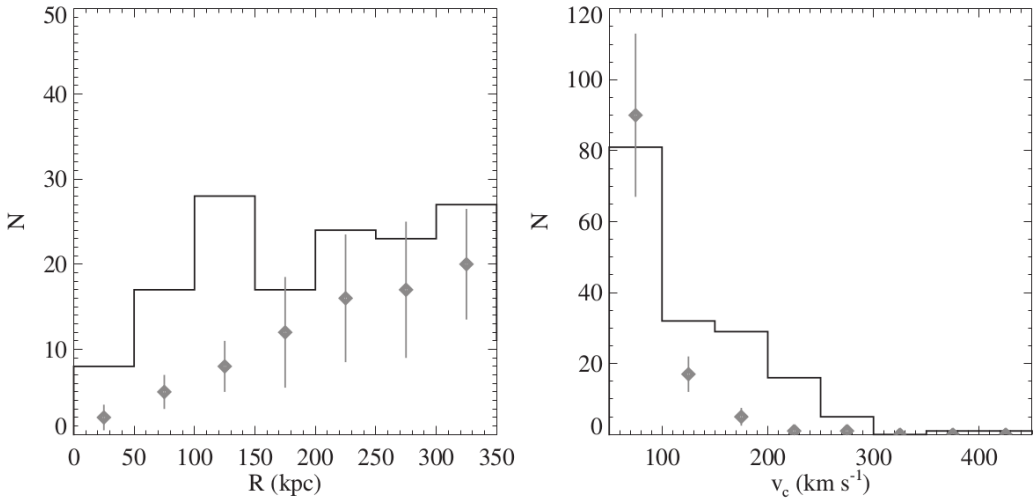

FIGURE 1.5: Number of subhalos as a function of the projected distance from the galaxy cluster center (left panel) and, within a two-dimensional aperture of 420 kpc, of their circular velocity value (right panel). The black histograms represent the values derived by Grillo et al., 2015 in the analysis of MACS0416 and the gray diamonds and bars show, correspondingly, the median values and the 1σ uncertainties obtained from cosmological simulations. Image from Grillo et al., 2015.

analysis of three clusters (MACSJ1149, MACSJ0416 and Abell 2744) is compared to those found in simulated clusters of similar mass. They report an excellent agreement between the observed and the simulated subhalo mass function over four decades in mass ($10^9 - 10^{13} M_\odot$). On the other hand, they find discrepancies in the subhalos radial distribution: in all three clusters, galaxies are significantly more centrally distributed with respect to simulations (Fig. 1.7). The reasons for this mismatch cloud be in sub-grid physics models implemented in simulations, for example over-efficient dynamical friction, tidal stripping and AGN feedback. However, as explained by the authors, this discrepancy can be also due to the fact that current cosmological simulations do not fully capture the dynamical complexity of disturbed, merging and rapidly evolving systems as the three observed clusters appears to be.

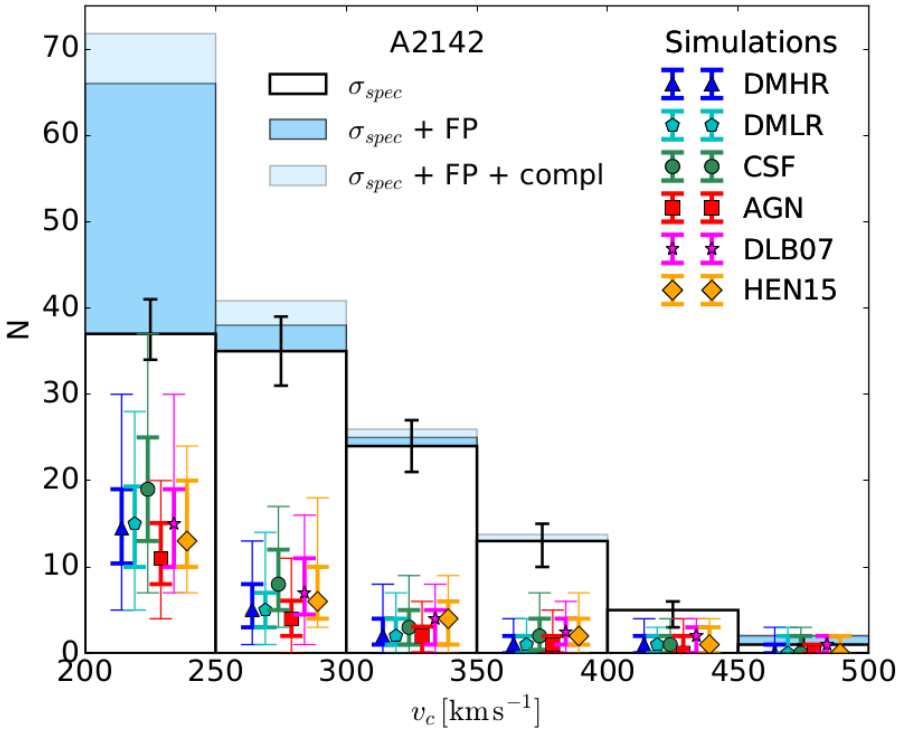

FIGURE 1.6: Distribution of the values of circular velocity of member galaxies of Abell 2142 within 2.2 Mpc in projection from the cluster center. The white histogram refers to the sample of members with measured velocity dispersion. Error bars represents the 16th and 84th percentiles in each bin. The blue histogram shows the distribution of the values of circular velocity of the members that have either a spectroscopic measurement of velocity dispersion or a velocity dispersion estimate inferred from the Fundamental Plane. When this last histogram is corrected to account for the incompleteness of the sample, the pale blue histogram is obtained. The colored symbols with error bars are the median values of circular velocity of subhalos in different simulated clusters, as indicated in the legend. Thick and thin error bars indicate the 16th-84th percentiles and the minimum-maximum values, respectively. Image from Munari et al., 2016.

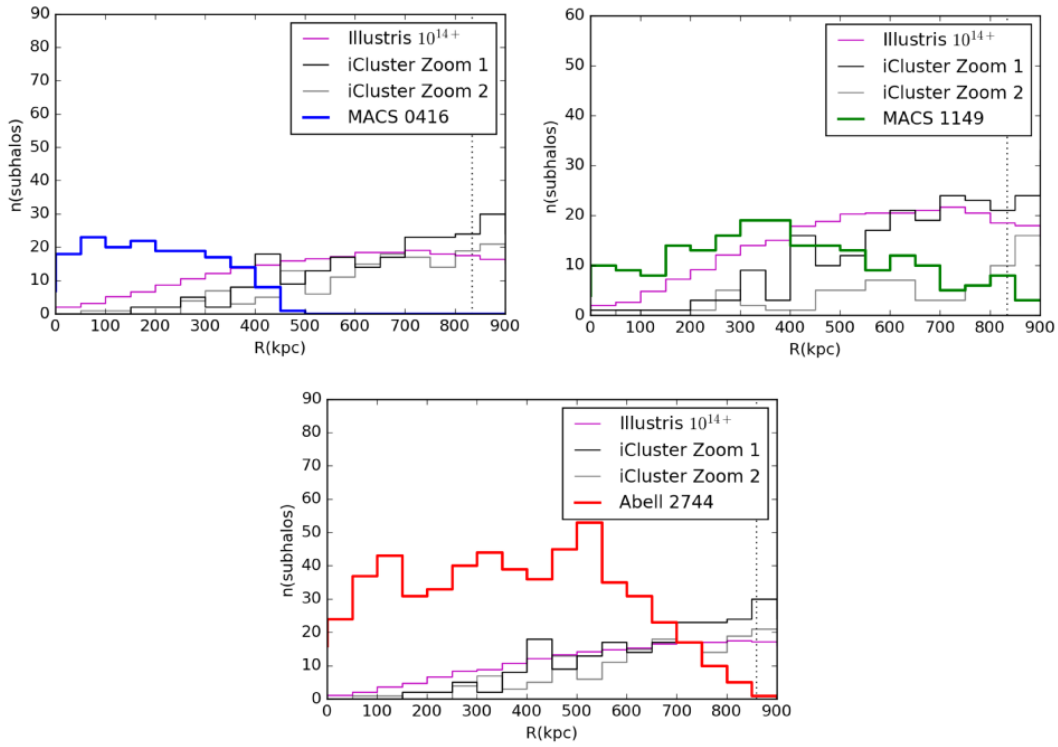

FIGURE 1.7: Each panel shows the comparison between the observed radial distribution of substructures and the distribution predicted by different sets of cosmological simulations. Simulated substructures are always less concentrated than observed ones. Images from Natarajan et al., 2017.

Chapter 2

Gravitational Lensing

2.1 Gravitational Lensing Theory

Light rays propagate according to Einstein's Theory of General Relativity. In this framework photons travel on null geodesics, whose geometrical properties are affected by the matter-energy content of space-time.

As seen in Chapter 1, on scales much larger than a few hundreds Mpc the universe can be described with the homogeneous and isotropic FRW metric (1.2). On smaller scales, the universe becomes "clumpy" due to the presence of galaxies and galaxy clusters, so the space-time metric and the light rays paths are locally influenced by the uneven distribution of matter. However, in many astrophysical situations the local gravitational field $\phi = -\frac{GM}{R}$ is small ($|\phi| \ll c^2$) or, in other words, the distance R to the center of mass of the distribution of matter is much larger than his Schwarzschild radius $R_s = 2GM/c^2$. Moreover, in ordinary situations the relative velocity v between the observer, the deflecting mass (lens) and the light source is much less than c. In such situations the *weak field* approximation is valid, namely the local $g_{\mu\nu}$ can be written as a small perturbation on the flat Minkowskian metric:

$$ds^2 = g_{\mu\nu}dx^\mu dx^\nu = \left(1 + \frac{2\phi}{c^2}\right)c^2dt^2 - \left(1 - \frac{2\phi}{c^2}\right)(d\vec{x})^2. \tag{2.1}$$

Light propagates on null geodesics, for which $ds^2 = 0$, so the light speed in the gravitational field is

$$c' = \frac{d\vec{x}}{dt} = c\sqrt{\frac{1 + 2\phi/c^2}{1 - 2\phi/c^2}} \approx c\left(1 + \frac{2\phi}{c^2}\right) < c. \tag{2.2}$$

This fact permits to define and effective *refraction index* as

$$n = \frac{c}{c'} = \frac{1}{1 + 2\phi/c^2} \approx 1 - \frac{2\phi}{c^2} < 1. \tag{2.3}$$

Using a variational approach based on the Fermat Principle, it is possible to show (see Schneider, Ehlers, and Falco, 1992) that the deflection angle $\hat{\vec{\alpha}}$ of a light path passing near a mass M with impact parameter b at $z = 0$ is

$$\hat{\vec{\alpha}}(b) = \frac{2}{c^2}\int_{-\infty}^{+\infty} \vec{\nabla}_\perp \phi dz \tag{2.4}$$

if this deflection occur on spatial scales much smaller than the distances between source, lens and observer (*thin screen approximation*) and on temporal scales in which

the expansion of the universe can be neglected. These conditions are generally satisfied even if the lens is a galaxy cluster. If the lens is a point mass, the previous result reduces to

$$|\hat{\vec{\alpha}}|(b) = \frac{4GM}{c^2 b} = \frac{2R_s}{b} \tag{2.5}$$

that is twice the value predicted with a Newtonian approach. It's important to notice that the deflection angle by a point mass depends linearly on M. Under the previous hypothesis, all general relativistic equations can be linearized and the resulting simplified theory is called *Gravitational Lensing Theory*.

The typical configuration of a gravitational lensing system is shown in fig. 2.1. Within the thin screen approximation, the lens is a two-dimensional distribution of matter on the so-called lens plane, where the deflection occurs. In this view, the lens mass distribution is described by the surface mass density

$$\Sigma(\vec{\xi}) = \int_{-\infty}^{+\infty} \rho(\vec{\xi}, z) dz. \tag{2.6}$$

Thanks to the linearity of (2.5), the deflection angles of multiple point lenses M_i can be linearly superposed, so

$$\hat{\vec{\alpha}}(\vec{\xi}) = \frac{4G}{c^2} \int_{-\infty}^{+\infty} \frac{(\vec{\xi} - \vec{\xi}_i)\Sigma(\vec{\xi}')}{|\vec{\xi} - \vec{\xi}_i|^2} d^2\xi'. \tag{2.7}$$

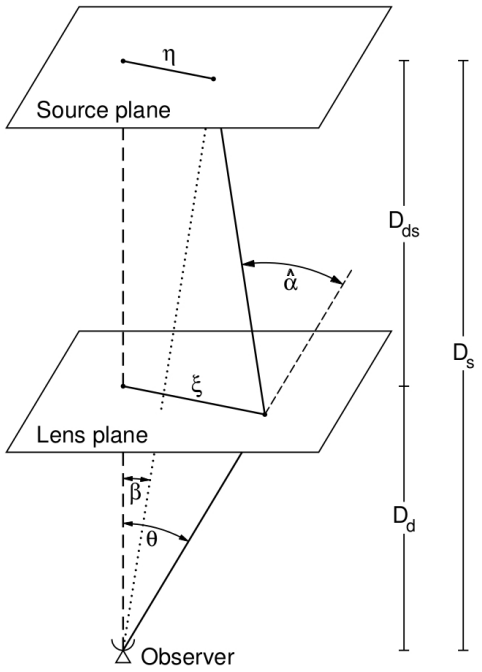

FIGURE 2.1: The typical configuration of a gravitational lensing system. Image from Bartelmann and Schneider, 1999.

2.1.1 The Lens Equation

If $\vec{\theta}, \vec{\beta}, \hat{\vec{\alpha}}$ are small, the true position of the source and its apparent position on the lens plane are related by a simple but fundamental equation, the *lens equation*, that

can be obtained by geometrical construction:

$$\vec{\theta} D_S = \vec{\beta} D_S + \hat{\vec{\alpha}} D_{LS} \tag{2.8}$$

where D_S, D_{LS} are the angular diameter distances between source and observer and source and lens, respectively. Introducing the *reduced deflection angle* $\vec{\alpha} \equiv \frac{D_{LS}}{D_S}\hat{\vec{\alpha}}$, previous equation becomes

$$\vec{\beta} = \vec{\theta} - \vec{\alpha}(\vec{\theta}). \tag{2.9}$$

It's common pratice to write the lens equation in dimensionless form, defining a length scale ξ_0 on the lens plane and a corresponding length scale $\eta_0 = \xi_0 D_S / D_L$ on the source plane. In this way, one can define the new vectors

$$\vec{x} \equiv \frac{\vec{\xi}}{\xi_0}; \quad \vec{y} \equiv \frac{\vec{\eta}}{\eta_0} \quad \Longrightarrow \quad \vec{\alpha}(\vec{x}) = \frac{D_L D_{LS}}{\xi_0 D_S}\hat{\vec{\alpha}}(\xi_0 \vec{x}) \tag{2.10}$$

where $\vec{\alpha}(\vec{x})$ is called the *scaled deflection angle*, to finally get:

$$\vec{y} = \vec{x} - \vec{\alpha}(\vec{x}). \tag{2.11}$$

2.1.2 Lensing potential and convergence

The lensing properties of a mass distribution are fully determined by its *effective lensing potential*, a quantity proportional to the projection of the Newtonian potential ϕ on the lens plane:

$$\hat{\Psi}(\vec{\theta}) = \frac{D_{LS}}{D_L D_S}\frac{2}{c^2}\int \phi(D_L\vec{\theta}, z) dz. \tag{2.12}$$

Its dimensionless counterpart is given by $\Psi = \hat{\Psi}\frac{D_L^2}{\xi_0^2}$. With a few calculations it's easy to show that

$$\vec{\nabla}_x \Psi(\vec{x}) = \vec{\alpha}(\vec{x}) \tag{2.13}$$

and that the Laplacian of Ψ gives twice the *convergence* κ:

$$\Delta_x \Psi(\vec{x}) = 2\kappa(\vec{x}) \tag{2.14}$$

that is defined as a dimensionless surface mass density:

$$\kappa(\vec{x}) \equiv \frac{\Sigma(\vec{x})}{\Sigma_{crit}} \quad \text{with} \quad \Sigma_{crit} = \frac{c^2}{4\pi G}\frac{D_S}{D_L D_{LS}}. \tag{2.15}$$

Σ_{crit} is called critical surface density and is a fundamental property of the lensing system, depending on the relative distances between source, lens and observer. Integrating (2.14) and using (2.13), one obtains:

$$\Psi(\vec{x}) = \frac{1}{\pi}\int_{R^2} \kappa(\vec{x}) \ln|\vec{x} - \vec{x}'| d^2x' \tag{2.16}$$

$$\vec{\alpha}(\vec{x}) = \frac{1}{\pi}\int_{R^2} \kappa(\vec{x})\frac{\vec{x} - \vec{x}'}{|\vec{x} - \vec{x}'|^2} d^2x'. \tag{2.17}$$

The dependence of the factor in front of the lensing potential (2.12) on the lens and source redshift is illustrated in Figs. 2.2 and 2.3. Fixing the source redshift and moving the lens from the observer to the source, the effective lensing potential decreases

to zero when $z_L = z_S$. This means that, for a fixed source distance, light is more effectively bent by nearer lenses. On the other hand, fixing the lens redshift and moving the source away, the effective lensing potential grows with source distance.

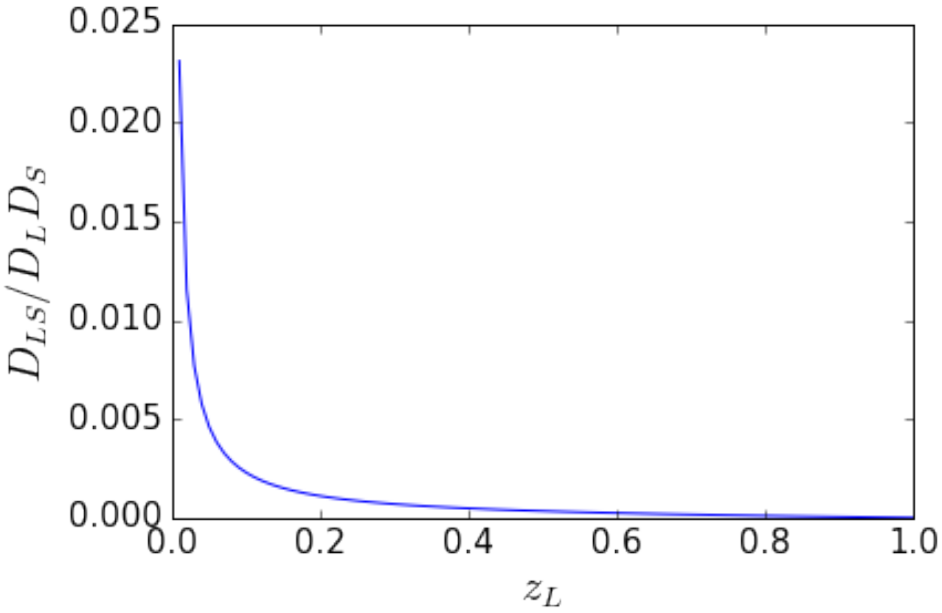

FIGURE 2.2: $D_{LS}/D_L D_S$ for different values of the lens redshift $z_L \in [0.0, 1.0]$. Source redshift is fixed at $z_S = 1.0$.

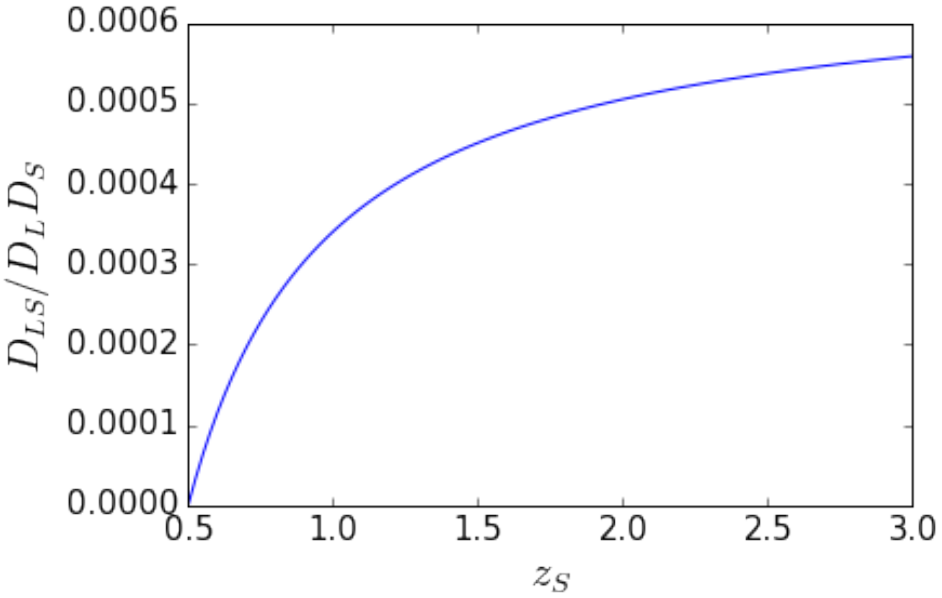

FIGURE 2.3: $D_{LS}/D_L D_S$ for different values of the source redshift $z_S \in [0.5, 3.0]$. Lens redshift is fixed at $z_L = 0.5$.

The other important distance combination is the *lensing distance* $D_{LS}D_L/D_S$, present in the definition of the convergence. His behaviour is shown in Figs. 2.4

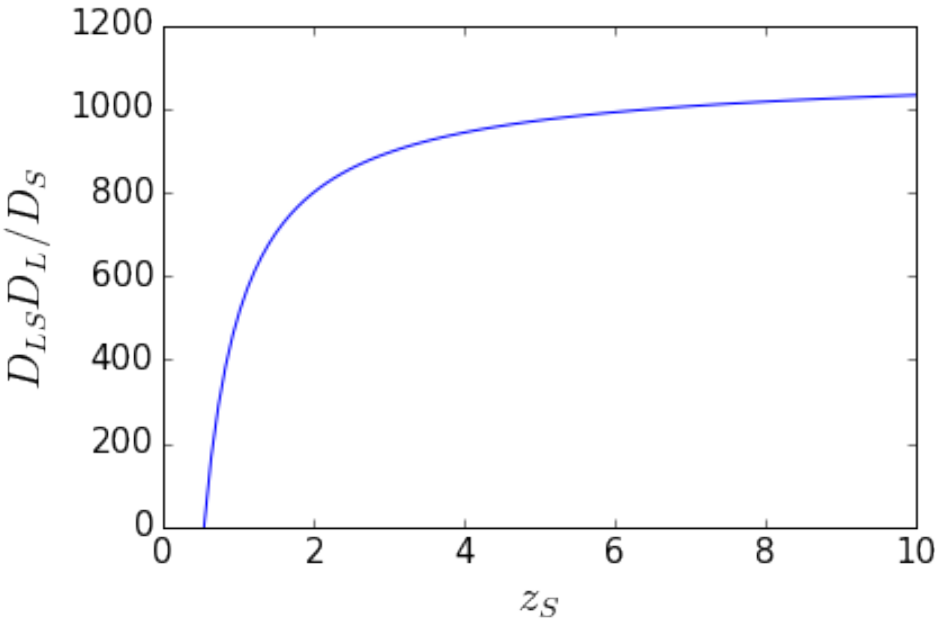

FIGURE 2.4: Lensing distance as a function of the source redshift z_S. Lens redshift is fixed at $z_L = 0.5$, while the source is moved in the range $z_S \in [0.5, 10.0]$.

and 2.5. Fixing the lens redshift and moving the source away, the convergence increases at once very rapidly and then more slowly. Conversely, fixing the source and moving the lens between the observer and the source one notice that convergence reaches a peak for an optimal z_L that increases with z_S.

2.1.3 Lens Mapping

The adimensional lens equation (2.9) defines a transformation between points on source and lens planes, trough $\vec{\alpha}(\vec{x})$. If we assume that the scaled deflection angle is fairly constant on the angular scale $d\vec{\theta}$, we can locally linearize the lens equation. In other words, if the angular size of the source is much smaller than the scale on which physical properties of the lens change, we can describe the image distortions trough the Jacobian matrix

$$A \equiv \frac{\partial \vec{y}}{\partial \vec{x}} = \left(\delta_{ij} - \frac{\partial \alpha_i(\vec{x})}{\partial x_j}\right) = \left(\delta_{ij} - \frac{\partial^2 \Psi(\vec{x})}{\partial x_i \partial x_j}\right) = (\delta_{ij} - \Psi_{ij})\,. \tag{2.18}$$

A can be splitted in two parts, namely

$$A = \underbrace{\left(A - \frac{1}{2}\mathrm{Tr}A \cdot I\right)}_{\text{anisotropic}} + \underbrace{\left(\frac{1}{2}\mathrm{Tr}A \cdot I\right)}_{\text{isotropic}} \tag{2.19}$$

$$= \begin{pmatrix} -\frac{1}{2}(\Psi_{11} - \Psi_{22}) & -\Psi_{12} \\ -\Psi_{12} & \frac{1}{2}(\Psi_{11} - \Psi_{22}) \end{pmatrix} + (1-k)\delta_{ij} \tag{2.20}$$

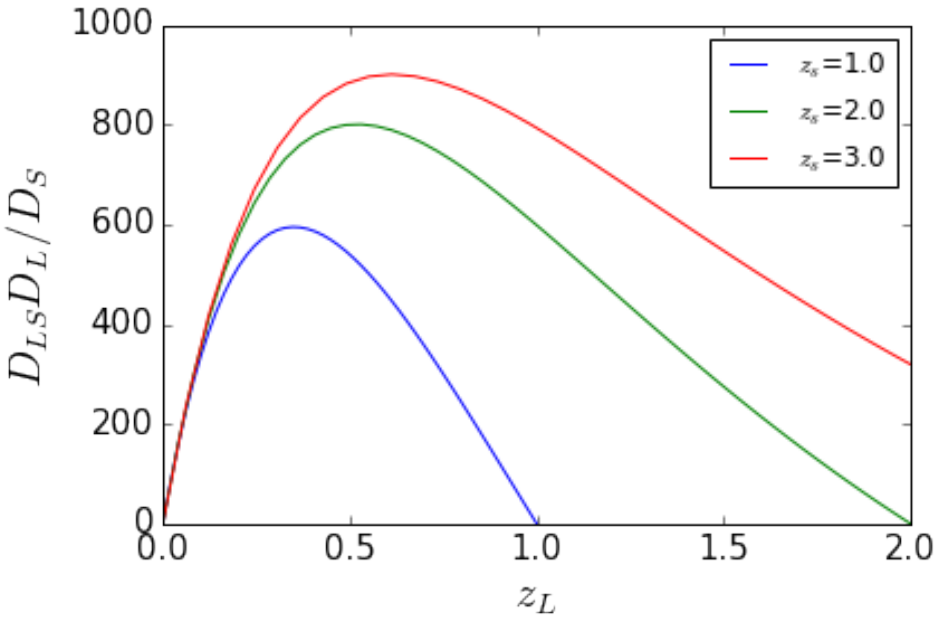

FIGURE 2.5: Lensing distance as a function of the lens redshift z_L and source redshift z_S. Source redshift is fixed at $z_S = 1.0, 2.0, 3.0$ in the blue, green and red case respectively, while the source is moved away from the lens.

and the pseudo-vector *shear* $\vec{\gamma} = (\gamma_1, \gamma_2)$ can be defined on the lens plane as

$$\gamma_1(\vec{x}) = \frac{1}{2}(\Psi_{11} - \Psi_{22}) \tag{2.21}$$

$$\gamma_2(\vec{x}) = \Psi_{12} = \Psi_{21}. \tag{2.22}$$

The anisotropic part of A is called the *shear matrix*, and his eigenvalues are $\pm\sqrt{\gamma_1^2 + \gamma_2^2} = \pm\gamma$; this means that is possible to find an angle ϕ such that

$$A = (1-k)\delta_{ij} - \gamma \begin{pmatrix} \cos 2\phi & \sin 2\phi \\ \sin 2\phi & -\cos 2\phi \end{pmatrix}. \tag{2.23}$$

The previous equations clarify the meaning of convergence and shear: the former induces an isotropic transformation, rescaling sources' images by a factor equal in all directions, the latter stretches images along a particular direction identified by eigenvectors of A. A circular source of radius r on the source plane is mapped onto an elliptical image on the lens plane, with semi-major and -minor axes given by

$$a = \frac{r}{\lambda_t} \quad , \quad b = \frac{r}{\lambda_r} \tag{2.24}$$

with

$$\lambda_t = 1 - k - \gamma \tag{2.25a}$$

$$\lambda_r = 1 - k + \gamma \tag{2.25b}$$

called respectively *tangential* and *radial* eigenvalue of A. This effect is shown in fig. 2.6.

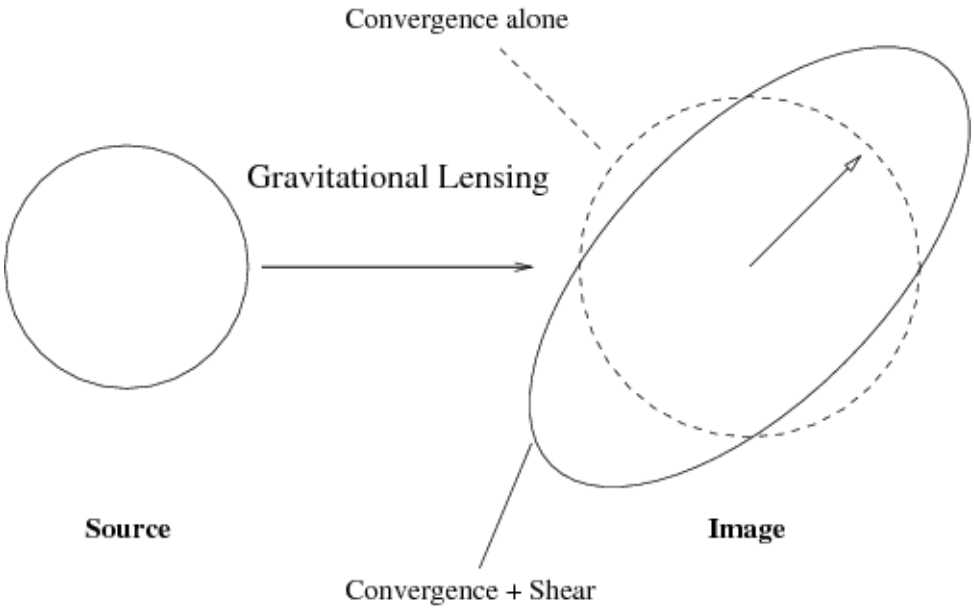

FIGURE 2.6: The effect of convergence and shear on a circular source.
Source: Umetsu, 2010

Another important effect of lens mapping is magnification. Since gravitational light deflection conserves the number of photons and their frequency, Liouville's theorem ensures that radiation density in phase-space is conserved, implying the conservation of surface brightness I_ν at the frequency ν. In contrast, gravitational lensing changes photon flux, changing the solid angle subtended by the source from $d\beta^2$ to $d\theta^2$. Defining the *magnification* μ as

$$\mu = \frac{d\theta^2}{d\beta^2} = (\mathrm{det}A)^{-1} = (\lambda_t \lambda_r)^{-1} \tag{2.26}$$

the observed flux F_ν at the frequency ν is amplified by a factor $|\mu|$ with respect to the flux of the source in absence of lensing:

$$F_\nu = \int_{\text{lens plane}} I_\nu(\vec{\theta}) d^2\theta = \int_{\text{source plane}} I^S_\nu(\vec{\beta}(\vec{\theta}))|\mu| d^2\beta. \tag{2.27}$$

Magnification is ideally infinite where λ_t or λ_r are equal to zero: this points on the lens plane constitute the tangential and radial *critical lines*. Near these lines images are stretched along the direction of the tangential and radial eigenvectors of the Jacobian matrix. Anyway, on critical lines the amplification is actually always finite: the theory exposed so far is only a first-order approximation of what really happens, but is enough for our purposes. Galaxy clusters can act as *cosmic telescopes*, reaching values of μ of ≈ 100 or more and allowing to investigate distant background galaxies with unprecedented resolution. Highly magnified sources are those situated near *caustics*, the locus of points on the source plane that correspond, through the lens equation (2.8), to critical lines (Fig. 2.7).

When a lens is enough *strong* to allow the formation of critical lines, it become possible to observe spectacular configurations of multiple images of the same source. Since light rays forming different images follows different paths, there is a time delay between them. This is caused both by the geometrical difference between paths and

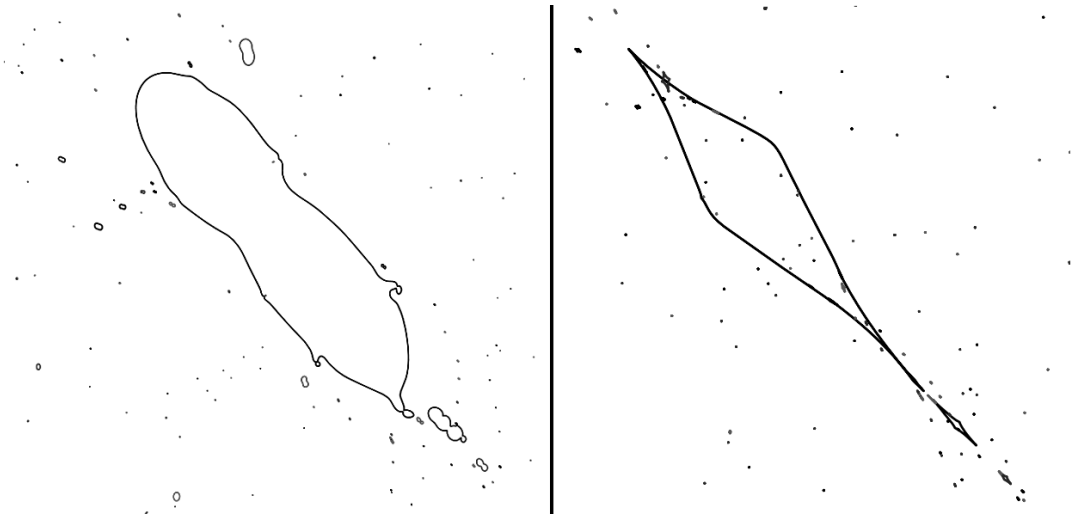

FIGURE 2.7: Example of critical lines of a simulated galaxy cluster (left) and corresponding caustics (right). Critical lines are mapped onto caustics through the lens equation (2.8).

by the different gravitational field affecting photons on different trajectories. It can be shown (Schneider, Ehlers, and Falco, 1992) that the total delay is such that time delay surfaces are described by the equation

$$t(\vec{x}) = \frac{(1+z_L)}{c}\frac{D_S\xi_0^2}{D_L D_{LS}}\left[\frac{1}{2}(\vec{x}-\vec{y})^2 - \Psi(\vec{x})\right] = 0 \tag{2.28}$$

where z_L is the redshift of the lens. Taking the gradient of this surface, one has

$$\nabla t(\vec{x}) \propto \vec{x} - \vec{y} - \nabla\Psi(\vec{x}) \tag{2.29}$$

$$\propto \vec{x} - \vec{y} - \vec{\alpha}(\vec{x}) \tag{2.30}$$

that is null where the lens equation (2.9) is satisfied, that is where images form. Therefore, images are located at the stationary points of the time delay surface (2.28).

The curvature of the time delay surface is described by the Hessian matrix

$$T_{ij} = \frac{\partial^2 t(\vec{x})}{\partial x_i \partial x_j} \propto (\delta_{ij} - \Psi_{ij}) = A_{ij}. \tag{2.31}$$

Different types of stationary points on this surface give rise to different types of image:

- *Type I images* occur at the minimums of time delay surface, where eigenvalues of T and A are both positive, so $\det A > 0$ and $\mathrm{tr}A > 0$. In this case $\mu > 0$.
- *Type II images* arise at the saddle points of the time delay surface, where λ_t and λ_r have opposite signs. Here μ is negative, that means that the image has an opposite parity with respect to the source.
- *Type III images* befall on the maximums of time delay surface where $\det A > 0$ and $\mathrm{tr}A < 0$, so they have positive magnification.

An example of time delay surface with the formation of a type I and a type II image is given in Fig. 2.8. In general, magnification is higher along the direction on which

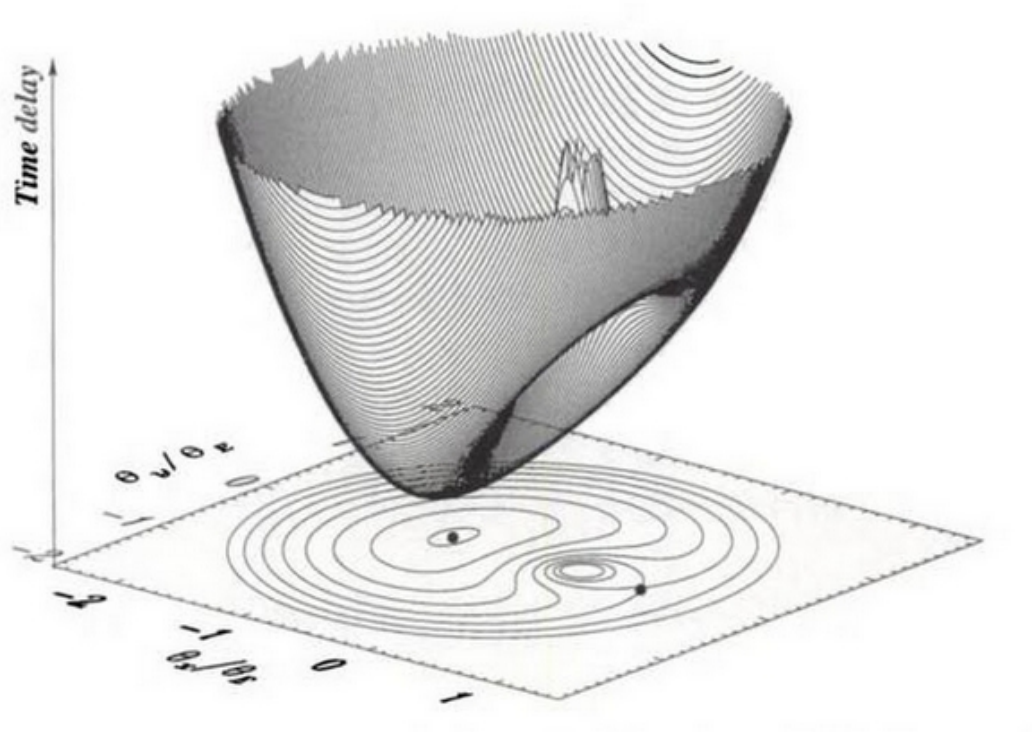

FIGURE 2.8: Time delay surface for a point-like lens not perfectly aligned with the source. Contour levels are shown in the bottom plane and the dots indicate the location of the two images. Source: Mollerach and Roulet, 2002.

curvature is smaller and vice versa. When a source and a circularly-symmetric lens are perfectly aligned $t(\vec{x})$ has a maximum at the lens center, while minima are located on a ring centered on the maximum. The source is therefore mapped in the so-called *Einstein Ring*, forming a type I image, and to a type III image at the center, that is usually highly demagnified due to the large curvature of $t(\vec{x})$ at this point (caused by a steep mass profile). Multiple images are usually in odd number except for singular lenses, where the infinite curvature of the time delay surface on the central singularity causes the suppression of the central image. An example is given in section 2.2.3. They appear or disappear near critical lines, namely when the source cross caustics.

2.2 Lens Models

In gravitational lensing studies analytical lens models are often used for many applications: from interpreting observations to predicting the rate of lensing events. We introduce here some of them which will be particularly useful in next chapters.

2.2.1 Generalities on axially symmetric models

In describing axially symmetric lenses, it is possible to reduce most of equations to one-dimensional form. Indeed, the deflection always occurs in the direction to the

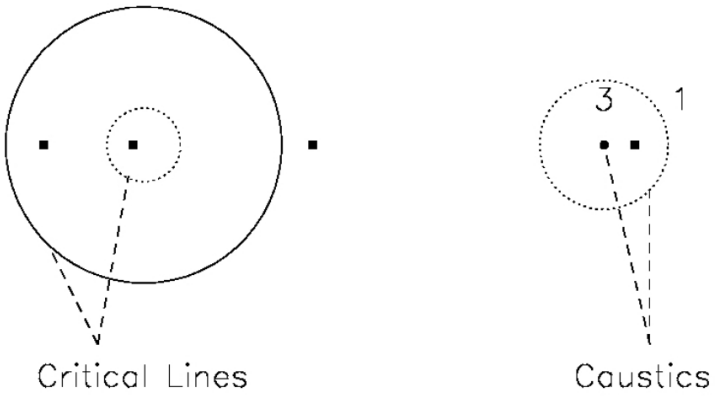

FIGURE 2.9: Lensing of a point source by a non-singular, circularly-symmetric lens. Left: image positions (black squares) and radial and tangential critical lines (respectively, dotted and solid curves); right: source position and corresponding caustics. Numbers indicate image multiplicity. From *Introduction to Gravitational Lensing - Lecture scripts*.

lens center. The deflection angle in this case is

$$\alpha(x) = \frac{m(x)}{x} \quad \text{with} \quad m(x) = 2\int_0^x x'\kappa(x')dx', \tag{2.32}$$

so the lens equations becomes

$$y = x - \frac{m(x)}{x}. \tag{2.33}$$

Carrying out some calculations it is possible to show that

$$\kappa(x) = \frac{1}{2x}\frac{dm}{dx} \tag{2.34}$$

$$\gamma(x) = \frac{m(x)}{x^2} - \kappa(x) = \bar{\kappa}(x) - \kappa(x) \tag{2.35}$$

where $\bar{\kappa}(x)$ is the mean value of κ inside the radius x. Tangential and radial critical lines are found solving, respectively,

$$1 - \bar{\kappa}(x) = 0 \quad \text{and} \quad 1 - 2\kappa(x) + \bar{\kappa}(x) = 0. \tag{2.36}$$

They are two concentric circumferences, mapped through the lens equation into a point (tangential caustic) and into a circular radial caustic, as shown in fig 2.9. If the source lies within the radial caustic, it produces three images (only two if the potential is singular), only one otherwise. If source, lens and observer are perfectly aligned, one has the formation of an Einstein ring.

2.2.2 Generalities on elliptical models

Broadly speaking, elliptical generalizations of axially symmetric profiles can be obtained substituting the x variable in circular profiles with $\sqrt{x_1^2 + f x_2^2}$, where f is the ratio between the minor and the major axes of the ellipse. This substitution can be

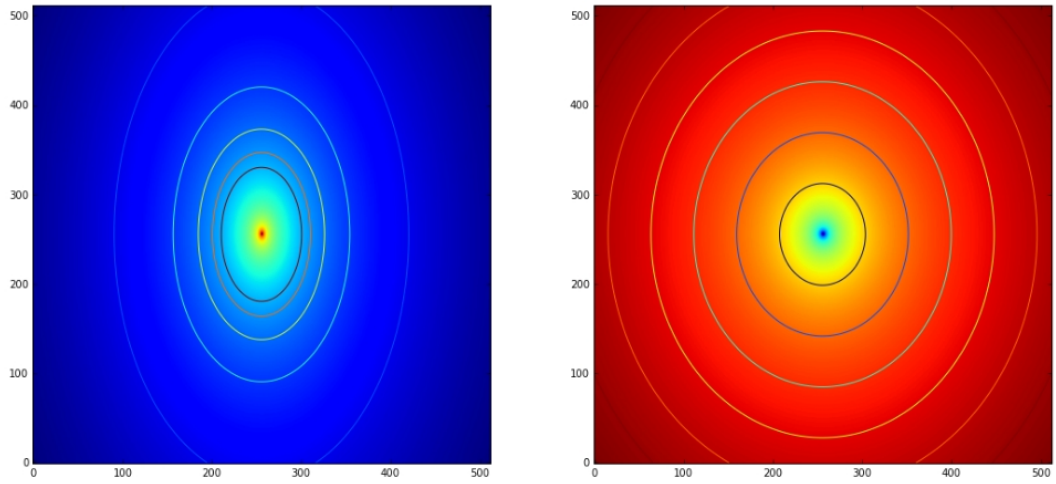

FIGURE 2.10: Convergence (left) and potential (right) of a SIE model whit $f = 0.6$. Colored curves represent iso-contours. The potential is rounder that the convergence.

carried out in the surface density or in the potential. In the first case the expressions for lensing quantities often become very complex, but they describe exactly light deflection by an elliptical mass distribution. An example is given in Fig. 2.10, where are shown convergence and potential for a Singular Isothermal Ellipsoid (SIE) model (see section 2.2.4). In the second case, one can derive easily all lensing quantities deriving the potential, but they can be unphysical for high ellipticities, when convergence iso-contours assume a peanut-like shape and the convergence become negative at large distances. Anyway, it is possible to give a general description of critical lines and caustics phenomenology in elliptical models.

Singular elliptical models produces elliptical or nearly-elliptical tangential critical lines, without radial critical lines. The tangential caustic is extended and typically shows four cusps. Image multiplicity changes when sources cross the tangential caustic and the *cut*, an ellipse on the source plane that is not a true caustics because it does not corresponds to a critical line. Depending on f, tangential caustic and cut can have different relative dimensions, as shown shown in Figs. 2.11 and 2.12. When source, lens and observer are perfectly aligned on can observe the Einstein cross, a symmetrical four-images configuration (Fig. 2.13).

If the lens is not singular but has a core radius x_c, depending on x_c and f can exist a radial caustic, and the central image isn't suppressed anymore, leading to the possibility to have three- and five-images configurations (Fig. 2.14).

2.2.3 Singular Isothermal Sphere

The Singular Isothermal Sphere (SIS) profile represents a lens whose constituent matter behaves like an ideal gas in thermal and hydrostatic equilibrium, confined by a spherically symmetrical gravitational potential. The density profile is given by

$$\rho(r) = \frac{\sigma_v^2}{2\pi G r^2} \tag{2.37}$$

where σ_v is the velocity dispersion of the particles which make up the lens and r is the radial distance. Projecting the three dimensional density on the lens plane we

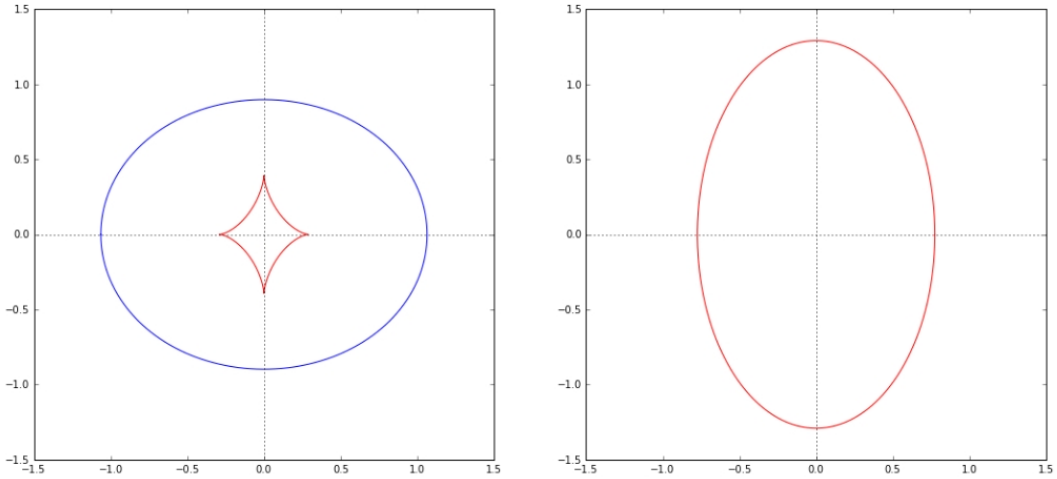

FIGURE 2.11: A SIE model whit $f < f_0 = 0.3942$. Left: the tangential caustic (red) is contained into the cut (blue). Right: tangential critical line. This model hasn't a radial critical line corresponding to the cut. Axis units are relative to the Einstein radius of the corresponding SIS model.

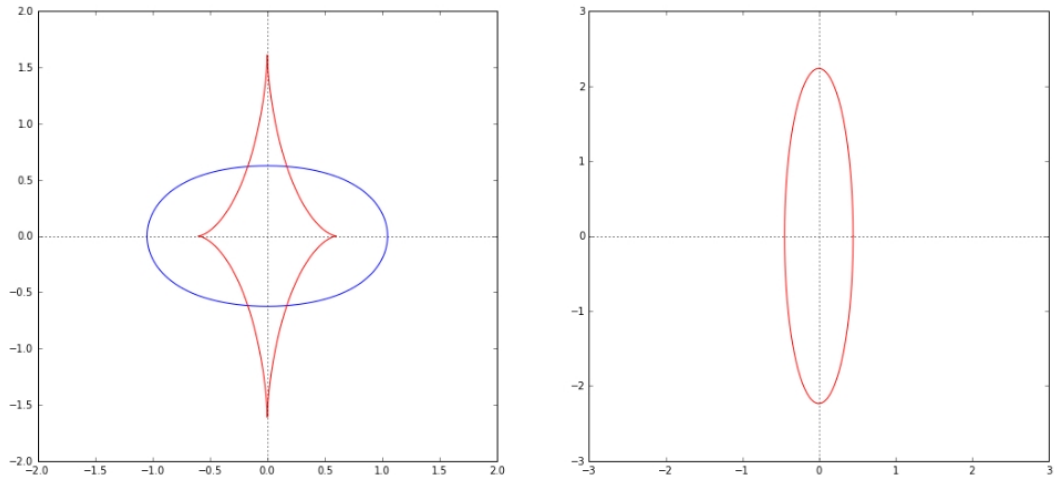

FIGURE 2.12: A SIE model whit $f > f_0 = 0.3942$. Left: the tangential caustic (red) isn't fully contained into the cut (blue). Right: tangential critical line. This model hasn't a radial critical line corresponding to the cut. Axis units are relative to the Einstein radius of the corresponding SIS model.

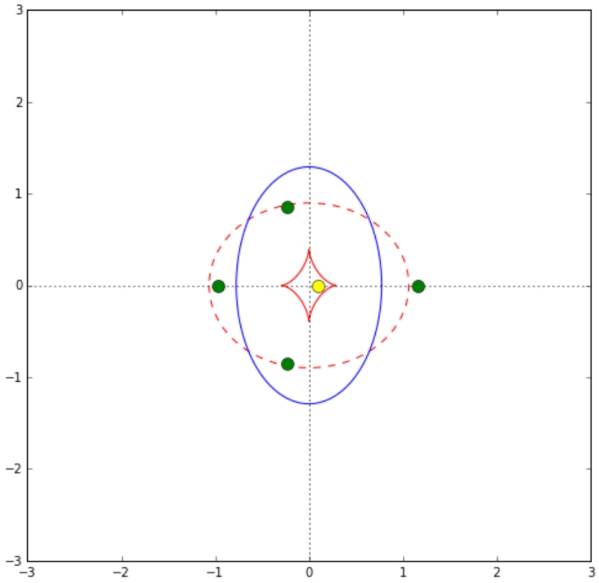

FIGURE 2.13: The Einstein Cross configuration: a source (yellow dot) nearly perfectly aligned with an elliptical lens form four images (green dots). If the source was exactly on the optical axis, the four images would form a symmetrical cross.

obtain the surface mass density

$$\Sigma(\xi) = \frac{\sigma_v^2}{2G\xi} \tag{2.38}$$

where $\vec{\xi}$ it's the projection of $\vec{r}$ on the lens plane and z is the distance along the line of sight: they satisfy the equation $r^2 = \xi^2 + z^2$. Even though this profile is singular at $\xi = 0$, it is widely used in lensing analysis and it was found to be a good description of the total matter distribution (stellar plus dark) in elliptical galaxies (Koopmans et al., 2009; Barnabè et al., 2011; Cappellari et al., 2015). This fact is commonly named *bluge-halo conspiracy*. Choosing $\xi_0 = 4\pi \left(\frac{\sigma_v}{c}\right)^2 \frac{D_L D_{LS}}{D_S}$ as lenght scale, we obtain

$$\Sigma(x) = \frac{\Sigma_{crit}}{2x} \quad \Longrightarrow \quad \kappa(x) = \frac{1}{2x} \tag{2.39}$$

and therefore

$$\Psi(x) = |x| \quad , \quad \alpha(x) = \frac{x}{|x|}. \tag{2.40}$$

The lens equations reads

$$y = x - \frac{x}{|x|} \tag{2.41}$$

that has 2 solutions if $y < 1$, only one otherwise. In the first case, the two images arise at $x = y + 1$ and $x = y - 1$, at the opposite sides of the lens. Their angular positions are

$$\theta_\pm = \beta \pm \theta_E \tag{2.42}$$

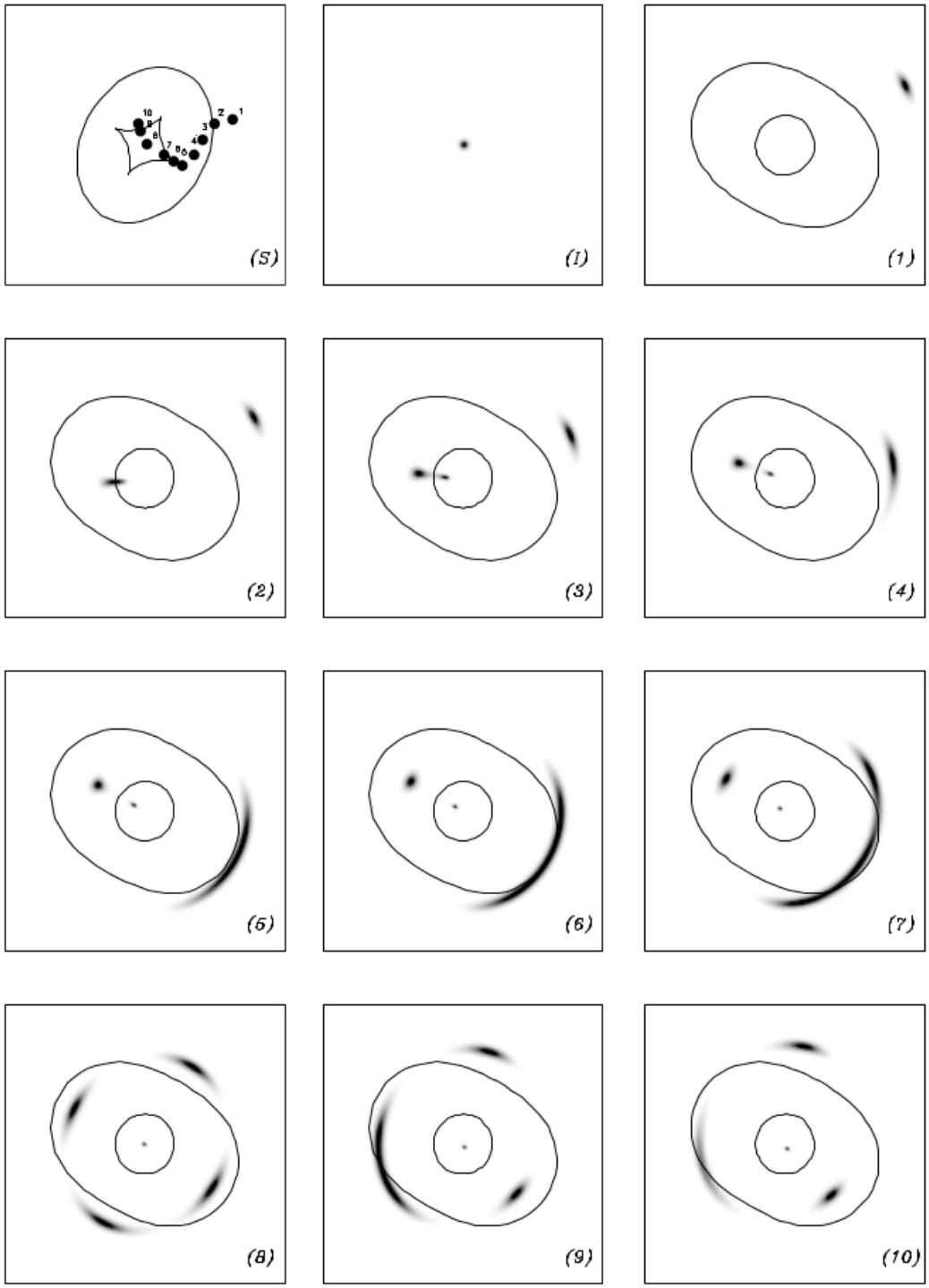

FIGURE 2.14: Multiple-image configurations produced by a nonsingular elliptical mass distribution. The panel (S) shows the caustic lines in the source plane and the positions numbered 1 to 10 denote the source position relative to the caustic lines. The panel (I) shows the image of the source without lensing. The panels (1) to (10) show the resulting lensed images for the various source positions. Panel (8) shows the Einstein cross configuration. Image from Kneib and Natarajan, 2011

where θ_E is the Einstein Radius of this lens model and correspond to

$$\theta_E = \sqrt{\frac{4GM(\theta_E)}{c^2}\frac{D_{LS}}{D_L D_S}}. \tag{2.43}$$

Therefore, when a SIS lens produces two images, they are separated by an angular distance of $2\theta_E$. On the other hand, when $y > 1$, Eq. (2.41) has only the solution $x = y + 1$ that tends to y when the angular separation between source and lens is big.

Calculating the derivatives of Ψ, it is possible to obtain the shear as

$$\gamma_1 = -\frac{\cos 2\phi}{2x} \qquad \gamma_2 = -\frac{\sin 2\phi}{2x} \tag{2.44}$$

thus

$$\gamma(x) = \sqrt{\gamma_1^2 + \gamma_2^2} = \frac{1}{2x} = \kappa(x). \tag{2.45}$$

Consequently, the radial eigenvalue is everywhere equal to unity (and there is not a radial critical line) and the tangential eigenvalue is equal to zero on the Einstein ring, where the (tangential) magnification is maximum. The magnification profile is

$$\mu = \frac{|x|}{|x| - 1} \tag{2.46}$$

from which we see that for $y \to \infty$, $\mu \to 1$ and if $y < 1$, the magnifications of the two images are

$$\mu_+ = 1 + \frac{1}{y} \quad , \quad \mu_- = 1 - \frac{1}{y} \tag{2.47}$$

that is to say that for $y \to 1$, the image on the same side of the source with respect to the lens tends to the intrinsic source position, while the opposite image is demagnified as it approaches the lens center.

With the lens equation it is easy to show that the tangential critical line (the Einstein ring) corresponds to the single caustic point $y = 0$ on the source plane. Image multiplicity changes when the source crosses the cut at $y = 1$.

2.2.4 Singular Isothermal Ellipsoid (SIE)

Choosing the same length scale ξ_0 as for the SIS case and defining the ellipticity $e = 1 - \frac{a}{b} = 1 - f$, one can introduce ellipticity in the Singular Isothermal model rewriting the potential (2.40) as

$$\Psi(x) = |x| \quad \Longrightarrow \quad \Psi(x, y) = \sqrt{(1-e)x^2 + (1+e)y^2}. \tag{2.48}$$

Deriving this elliptical potential, one obtains

$$\kappa(x, y) = \gamma(x, y) = \frac{1 - e^2}{2R^3}(x^2 + y^2) \tag{2.49}$$

where $R^2 = (1-e)x^2 + (1+e)y^2$. The potential is always rounder than the mass distribution, with $e_{pot} \sim e_{mass}/3$ (see Fig. 2.10). The tangential critical line becomes elliptical, and is mapped in an extended tangential caustic with four cusps (Figs. 2.11 and 2.12).

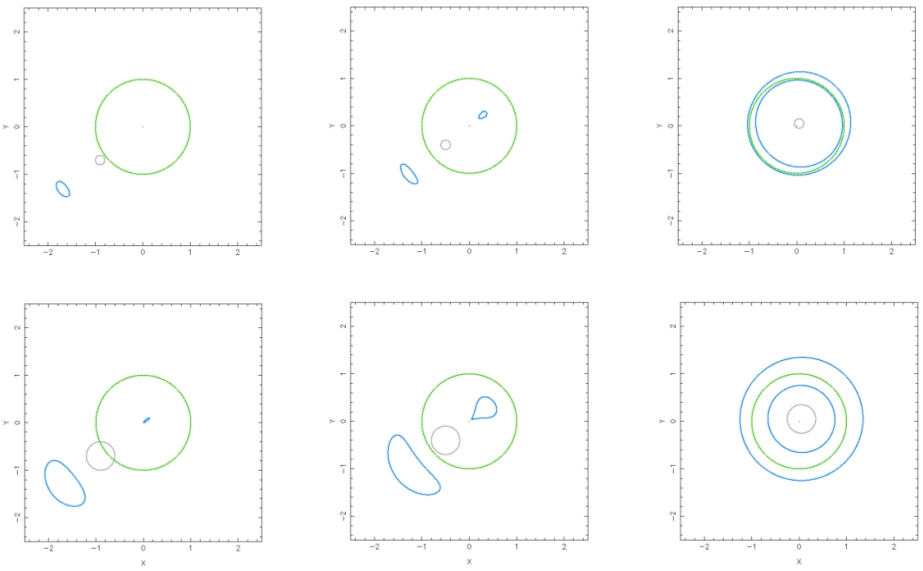

FIGURE 2.15: Multiple images of the SIS model, with a circular source of two different radii: a small source of radius 0.05 in the first row and a large source of radius 0.3 in the second row. Their positions are (-0.9:-0.7); (-0.5:-0.4); (+0.05:+0.05) in unit of Einstein radius, for each column. The circular source is in gray and the corresponding multiple images are in blue. The green lines are tangential critical curves and dotted circles are the cuts. Source: Lee and Kim, 2014

2.2.5 NFW profile

The Navarro-Frenk-White (NFW) profile is widely used to describe dark matter distributions. It was proposed by Navarro, Frenk, and White, 1995 as a "universal" function, capable to fit spherically averaged density profiles of dark matter halos found in numerical simulations over two decades in radius. It's given by

$$\rho(r) = \frac{\rho_s}{\left(\frac{r}{r_s}\right)\left(1+\frac{r}{r_s}\right)^2} \tag{2.50}$$

where r_s is the *scale radius* and ρ_s is the dark matter density at the scale radius. It is characterized by an isothermal slope at intermediate radii, but it is steeper near the center and shallower at large distances. The total mass of a halo is usually written as

$$M_{vir} = \frac{4\pi}{3} r_{vir}^3 \frac{\Delta_{vir}}{\Omega_m(z)} \Omega_0 \rho_c \tag{2.51}$$

where ρ_c represents the critical density of the Universe,$\Omega_0 = \Omega_m(t_0)$ is the today's value of the matter density parameter, Δ_{vir} is the virial overdensity enclosed by r_{vir}, the virial radius of the halo, corresponding to the distance within which particles are gravitationally bound to the halo traveling on equilibrium orbits. With this definition, Δ_{vir} is a function of cosmology and redshift; in this work we adopt the value $\Delta_{vir} = 200$, originally proposed by Navarro, Frenk, and White, 1995 and widely used in literature. An important parameter in the description of an NFW profile is the virial concentration, defined as the ratio between the radius enclosing the virial overdensity and the scale radius: $c_{vir} = r_{vir}/r_s$. The dark matter density at the scale

radius can be written in terms of the halo mass and concentration as

$$\rho_s = \frac{M_{vir}}{4\pi r_s^3}\left[\ln(1+c_{vir}) - \frac{c_{vir}}{1+c_{vir}}\right]^{-1} \tag{2.52}$$

so the profile can be rewritten in terms of M_{vir} and c_{vir}:

$$\rho(r|M_{vir}) = \frac{c_{vir}^2 r_{vir}^3}{3r(r_{vir}+c_{vir}r)^2}\frac{\Delta_{vir}}{\Omega_m(z)}\Omega_0\rho_c\left[\ln\left(1+c_{vir}-\frac{c_{vir}}{1+c_{vir}}\right)\right]^{-1}. \tag{2.53}$$

Summarizing, the NFW profile is completely defined by two parameters, ρ_s and r_s or c_{vir} and M_{vir}. The projected mass density is given in Bartelmann, 1996 as

$$\Sigma(x) = \frac{2\rho_s r_s}{x^2-1}f(x) \tag{2.54}$$

where $x = \xi/r_s$ and f is given by

$$f(x) = \begin{cases} 1 - \frac{2}{\sqrt{x^2-1}}\arctan\sqrt{\frac{x-1}{x+1}} & x > 1 \\ 1 - \frac{2}{\sqrt{1-x^2}}\operatorname{arctanh}\sqrt{-\frac{x-1}{x+1}} & x < 1 \\ 0 & x = 1. \end{cases} \tag{2.55}$$

Defining $\kappa_s \equiv \rho_s r_s \Sigma_{crit}^{-1}$, one has

$$\kappa(x) = 2\kappa_s\frac{f(x)}{x^2-1}. \tag{2.56}$$

The shear can be written down following Eq. (2.35). Finally, lensing potential and deflection angle are given by

$$\Psi(x) = 4\kappa_s g(x) \quad , \quad \alpha(x) = \frac{4\kappa_s}{x}h(x) \tag{2.57}$$

with

$$g(x) = \frac{1}{2}\ln^2\frac{x}{2} + \begin{cases} 2\arctan^2\sqrt{\frac{x-1}{x+1}} & x > 1 \\ -2\operatorname{arctanh}^2\sqrt{-\frac{x-1}{x+1}} & x < 1 \\ 0 & x = 1 \end{cases} \tag{2.58}$$

$$h(x) = \ln\frac{x}{2} + \begin{cases} \frac{2}{\sqrt{x^2-1}}\arctan\sqrt{\frac{x-1}{x+1}} & x > 1 \\ \frac{2}{\sqrt{1-x^2}}\operatorname{arctanh}\sqrt{-\frac{x-1}{x+1}} & x < 1 \\ 1 & x = 1 \end{cases} \tag{2.59}$$

A comparison between some lensing properties of SIS and NFW profiles is shown in fig. 2.16.

2.2.6 gNFW profile

The slope of the Navarro-Frenk-White profile can be made steeper or shallower introducing an additional parameter β, namely writing a generalized NFW profile

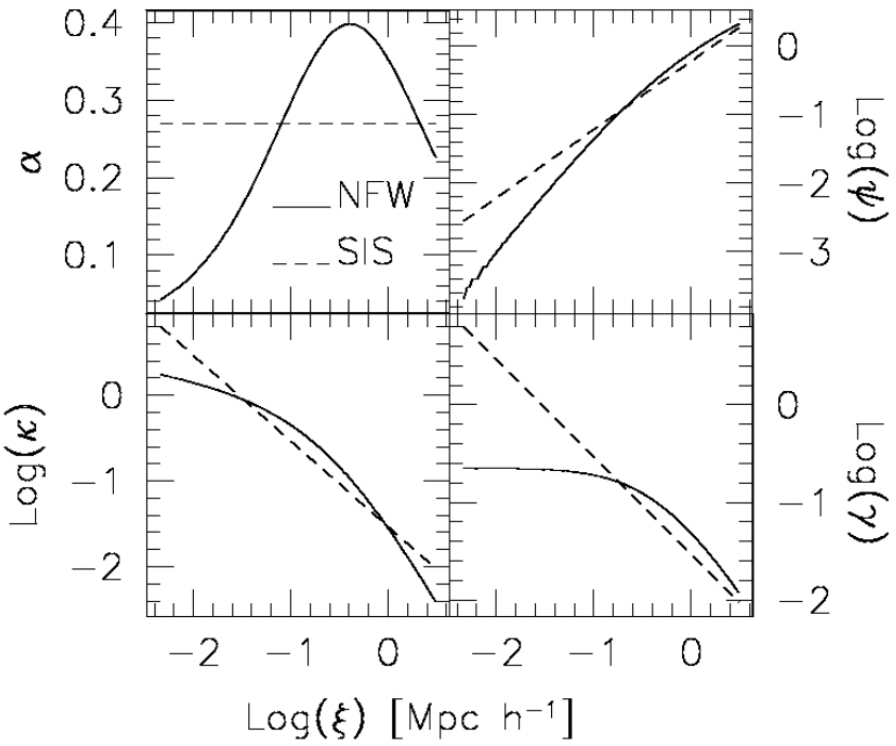

FIGURE 2.16: Some properties of NFW and SIS lenses as functions of the distance from the lens center. Top left panel: reduced deflection angle; top right panel: lensing potential; bottom left panel: convergence; bottom right panel: shear. Image from *Introduction to Gravitational Lensing - Lecture scripts*.

(gNFW) as

$$\rho(r) = \frac{\rho_s}{\left(\frac{r}{r_s}\right)^{\beta}\left(1+\frac{r}{r_s}\right)^{3-\beta}}. \tag{2.60}$$

For this profile is defined a new concentration parameter $c_{-2} = c_{vir}/(2-\beta)$. In analogy with the NFW case, it can be shown that this profile can be written in terms of the three parameters c_{-2}, M_{vir}, β.

Using dimensional notation, the surface mass distribution can be written as (Wyithe, Turner, and Spergel, 2001):

$$\Sigma(\xi) = 2\rho_s r_s x^{1-\beta}\int_0^{\frac{\pi}{2}} \sin\theta(\sin\theta + x)^{\beta-3}d\theta \tag{2.61}$$

and the other lensing quantities can be derived applying the equations given in section 2.2.1. Several properties of this lens model such as, for example, the deflection angles can only be derived numerically.

2.2.7 PIEMD profile

The Pseudo Isothermal Elliptical Mass Distribution (PIEMD) profile is widely used in lens modeling. The main advantage of using this profile is that its lensing properties can be expressed analytically. In this work we refer to the profile described in Elíasdóttir et al., 2007. The $3D$ density distribution is given by

$$\rho(r) = \frac{\rho_0}{(1+r^2/a^2)(1+r^2/s^2)} \tag{2.62}$$

where ρ_0 is the central density, a is the core radius and $s > a$ is the truncation radius. Inside the core radius the density scales as $\rho(r) \propto \rho_0/(1+r^2/a^2)$, while for $r \gg s$ the density is not zero but falls off as $r \propto r^{-4}$. In the intermediate region ($a \lesssim r \lesssim s$) the profile is isothermal. The projected density at the projected radius ξ on the lens plane is given by

$$\Sigma(\xi) = 2\int_{\xi}^{\infty}\frac{\rho(r)rdr}{\sqrt{r^2-\xi^2}} = \Sigma_0\frac{as}{s-a}\left(\frac{1}{\sqrt{a^2+\xi^2}} - \frac{1}{\sqrt{s^2+\xi^2}}\right) \tag{2.63}$$

where

$$\Sigma_0 = \pi\rho_0\frac{as}{s+a}. \tag{2.64}$$

One can obtain the convergence applying the definition (2.15), while the shear is given by

$$\gamma(\xi) = \frac{\Sigma_0}{\Sigma_{crit}}\frac{as}{s-a}\left[2\left(\frac{1}{a+\sqrt{a^2+\xi^2}} - \frac{1}{s+\sqrt{s^2+\xi^2}}\right) + \left(\frac{1}{\sqrt{a^2+\xi^2}} - \frac{1}{\sqrt{s^2+\xi^2}}\right)\right]. \tag{2.65}$$

The mass inside ξ is

$$M_{2D}(<\xi) = 2\pi\int_0^{\xi}\Sigma(\xi')\xi' d\xi' = 2\pi\Sigma_0\frac{as}{s-a}\left(\sqrt{a^2+\xi^2} - a - \sqrt{s^2+\xi^2}s\right) \tag{2.66}$$

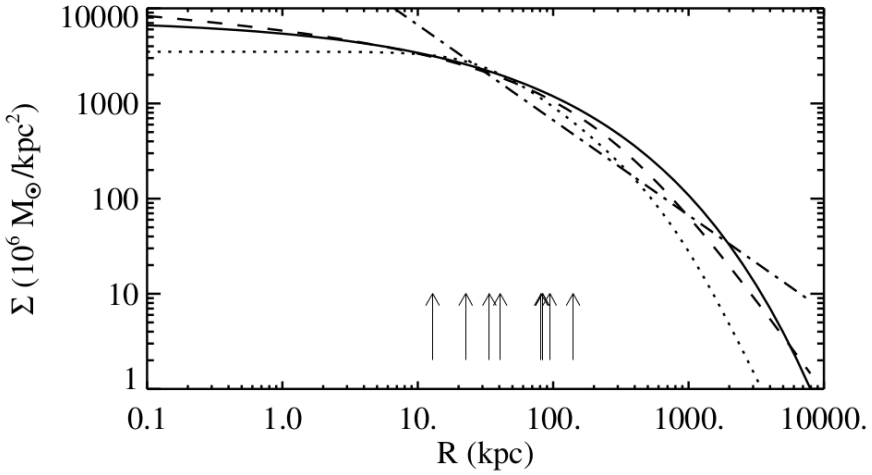

FIGURE 2.17: Comparison between PIEMD (dotted line), NFW (dashed line) and SIS (dot-dashed line) profiles. The surface densities are obtained fitting the same set of multiple images (marked with arrows) with the different profiles, as explained in Jullo et al., 2007. The SIS profile has a constant slope and hardly follows the other profiles.

from which one can obtain the lensing potential by integration:

$$\Psi(\xi) = 2G \int_{\xi}^{\xi_L} \frac{M_{2D}(\xi')}{\xi'} d\xi' \tag{2.67a}$$

$$= 4\pi G \Sigma_0 \frac{as}{s-a} (\sqrt{s^2+\xi^2} - \sqrt{a^2+\xi^2} + a \ln\left(a + \sqrt{a^2+\xi^2}\right) - \tag{2.67b}$$

$$- s \ln\left(s + \sqrt{s^2+\xi^2}\right)) + \text{constant} \tag{2.67c}$$

where ξ_L is a limiting integration radius leading to the constant term. Thus, the deflection angle is given by

$$\alpha(\xi) = -\frac{2}{c^2} \frac{D_{LS}}{D_S} \frac{d\Psi}{d\xi} \tag{2.68a}$$

$$= \frac{8\pi G}{c^2} \frac{D_{LS}}{D_S} \Sigma_0 \frac{as}{s-a} \left(\frac{\xi/a}{1+\sqrt{1+(\xi/a)^2}} - \frac{\xi/s}{1+\sqrt{1+(\xi/s)^2}} \right). \tag{2.68b}$$

A comparison between PIEMD, NFW and SIS profiles is shown in Fig. 2.17.

2.2.8 External shear

In order to obtain more realistic models, it is often needed to place a lens into an external shear field created by surrounding matter, on a sheet of constant surface mass density or both. This situation is particularly common in dense environments, such as galaxy clusters. This will be discussed in more details in the next chapters.

In general, both situations can be described by an external potential Ψ satisfying

$$\gamma_1 = \frac{1}{2}(\Psi_{11} - \Psi_{22}) = \text{const.} \tag{2.69}$$

$$\gamma_2 = \Psi_{12} = \text{const.} \tag{2.70}$$

$$\kappa = \frac{1}{2}(\Psi_{11} + \Psi_{22}) = \text{const.} \tag{2.71}$$

Since both the sum and the difference of Ψ_{11}, Ψ_{22} need to be constant, Ψ_{11} and Ψ_{22} themselves must be constant. Thus, the potential is of the form

$$\Psi = Cx_1^2 + C'x_2^2 + Dx_1x_2 + E, \tag{2.72}$$

implying that

$$\frac{1}{2}(\Psi_{11} - \Psi_{22}) = C - C' = \gamma_1 \tag{2.73}$$

$$\Psi_{12} = D = \gamma_2 \tag{2.74}$$

$$\frac{1}{2}(\Psi_{11} + \Psi_{22}) = C + C' = \kappa. \tag{2.75}$$

Imposing $\kappa = 0$ one has $C = -C'$, requiring $C = \frac{\gamma_1}{2}$, so the external shear potential Ψ_γ is given by:

$$\Psi_\gamma = \frac{\gamma_1}{2}(x_1^2 - x_2^2) + \gamma_2 x_1 x_2. \tag{2.76}$$

Similarly, imposing a null shear field one obtains the potential Ψ_κ of a sheet of a constant surface mass density:

$$\Psi_\kappa = \frac{\kappa}{2}(x_1^2 + x_2^2). \tag{2.77}$$

Adding an external perturbation to a lens model obviously modifies its lensing properties. The effect of a constant external shear field is to change the light bending introducing an additional deflection angle $\vec{\alpha_\gamma}$:

$$\vec{\nabla}\Psi_\gamma = \vec{\alpha_\gamma} = \begin{pmatrix} \gamma_1 & \gamma_2 \\ \gamma_2 & -\gamma_1 \end{pmatrix} \vec{x} \tag{2.78}$$

while a sheet of constant surface mass density gives the deflection angle $\vec{\alpha_\kappa}$:

$$\vec{\alpha_\kappa} = \vec{\nabla}\Psi_\kappa = \kappa\vec{x}. \tag{2.79}$$

In this case the lens equation is $\vec{y} = \vec{x}(1 - \kappa)$, so if this sheet is critical ($\kappa = 1$) it focuses light rays in the origin.

Chapter 3

Galaxy clusters as gravitational lenses

This chapter is dedicated to galaxy clusters. After a presentation of their general properties, we present the wide range of gravitational lensing phenomena that can be observed in galaxy clusters, from weak to strong lensing, with a particular attention to strong lensing of background sources by cluster members. In fact, all the rest of the work will focus on this kind of events.

3.1 Main properties of galaxy clusters

Galaxy clusters play a special role in the present universe, since they are the largest structures, and therefore the youngest to form in the universe. They originate from the greatest mass peaks in the primordial matter density field, gravitationally amplified through the structure formation process described in the previous chapter. In cosmological N-body simulations, they appear as dense concentrations of matter at the intersections of "cosmic web" filaments. Clusters are thought to form trough a hierarchical sequence of mergers and accretion of smaller systems, that may be survived until present time to form the actual substructure population. Dark matter is the dominant mass component ($80 - 85\%$) followed by Intracluster Medium (ICM, $10 - 15\%$) and stars in galaxies, making up only a few percent of the total cluster mass.

The main observational properties of clusters and groups of galaxies are summarized in Table 3.1 (Bahcall, 1999). The table lists the typical range and/or median value of each observed property, for rich and poor clusters. Rich clusters are defined by Abell, 1958 as those containing at least 30 galaxies within a magnitude range of m_3 to $m_3 + 2$ within a radius of $R \approx 1.5/h$ Mpc of the cluster center, where m_3 is the magnitude of the third brightest cluster member. In the next sections, properties of galaxy clusters relevant to our discussion are exposed with further details.

3.1.1 Galaxies

Galaxies in clusters are different with respect to those found in the field. In particular, as shown in Fig. 3.1 it is clear that clusters host mainly early-type galaxies (ETGs), while in the field it's more common to find spiral, irregular and star-forming galaxies (Dressler, 1980).

At the center of galaxy clusters it is possible to find the most massive galaxies in the universe, generally called Brightest Cluster Galaxies (BCG) or cD-type galaxies. They are thought to form via accretion of matter falling in the cluster potential well and thanks to merging between several galaxies (Ostriker and Hausman, 1977, Merritt, 1984).

Property	Rich clusters	Poor clusters (groups)
Richness	30-300 galaxies	3-30 galaxies
Radius	(1-2) h^{-1} Mpc	(0.1-1) h^{-1} Mpc
Radial velocity dispersion	400-1400 km s^{-1}	100-500 km s^{-1}
Radial vel. disp. (median)	$\sim$ 750 km s^{-1}	$\sim$ 250 km s^{-1}
Mass ($r \leq 1.5\ h^{-1}$ Mpc)	$(10^{14} - 2 \cdot 10^{15}) h^{-1}\ M_\odot$	$(10^{12.5} - 10^{14}) h^{-1}\ M_\odot$
Luminosity (B band)	$(6 \cdot 10^{11} - 6 \cdot 10^{12}) h^{-2}\ L_\odot$	$(10^{10.5} - 10^{12})\ h^{-2}\ L_\odot$
Mass-to-light Ratio	$300 h M_\odot / L_\odot$	$200 h M_\odot / L_\odot$
Cluster number density	$(10^{-5} - 10^{-6}) h^3 Mpc^{-3}$	$(10^{-3} - 10^{-5}) h^3 Mpc^{-3}$
Correlation scale	(22$\pm$4)h^{-1} Mpc	(13$\pm$2)h^{-1} Mpc

TABLE 3.1: Typical properties of groups and clusters of galaxies. For more details, see Bahcall, 1999. Here, radius means the radius of the main concentration of galaxies (where, typically, the galaxy surface density drops to $\approx 1\%$ of the central core density).

Kinematics of galaxies can be used to infer the cluster total mass. The virial theorem states that, for an object that is bound by gravity, the kinetic energy K of the system and its gravitational potential energy U are related by $2K + U = 0$. Applying this result to a cluster with mass M and radius R, we can write the kinetic energy of cluster members in terms of their velocity dispersion σ_v as

$$K \approx \frac{1}{2} M \sigma_v^2 \tag{3.1}$$

and the total potential energy of the system as

$$U \approx -\frac{GM^2}{R}. \tag{3.2}$$

From the previous equations follows a simple relation between the mass of the entire system, its size and the velocity dispersion of galaxies, namely

$$M \approx \frac{R\sigma_v^2}{G} \approx \left(\frac{R}{1h^{-1}Mpc}\right)\left(\frac{\sigma_v}{10^3 km/s}\right) 10^{15} h^{-1}\,\mathrm{M}_\odot \tag{3.3}$$

(Rosati, Borgani, and Norman, 2002). Thus, the total mass of a galaxy cluster can be estimated measuring members velocities.

More refined methods make use of redshift measurement to deduce the infall velocity field around the cluster (see, for example, the caustic method by Diaferio and Geller, 1997, Rines and Diaferio, 2006).

3.1.2 Intracluster Medium

Observed ICM in nearby and distant clusters has a typical temperature that follows the relation :

$$k_B T \approx \mu m_p \sigma_v^2 \approx 6 \left(\frac{\sigma_v}{10^3 \mathrm{km\ s^{-1}}}\right)^2 \quad \mathrm{KeV} \tag{3.4}$$

where m_p is the proton mass and μ is the mean molecular weight, expected if gas and member galaxies shares the same dynamics (Rosati, Borgani, and Norman, 2002). Assuming spherical symmetry, the condition of hydrostatic equilibrium connecting

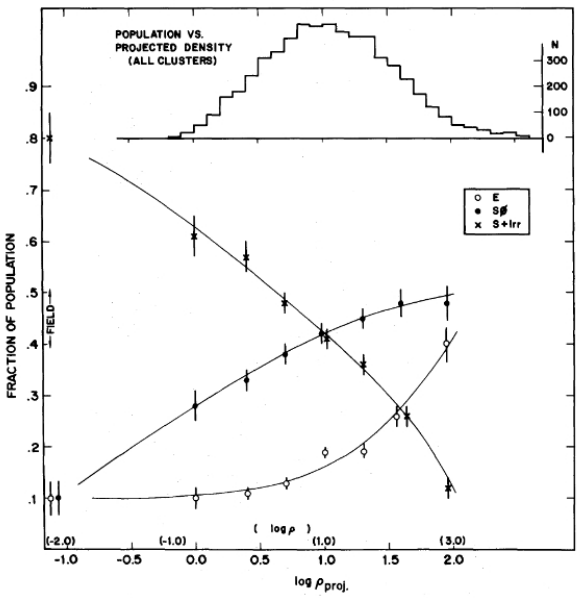

FIGURE 3.1: The fraction of elliptical (E), lenticular (S0), and spiral+irregular (S+I) galaxies as a function of the log of the projected density, in galaxies Mpc^{-2} , for a sample of cluster galaxies and for the field. The upper histogram shows the number distribution of the galaxies over the bins of projected density (Dressler, 1980).

the local gas pressure p to its density ρ_g is

$$\frac{dp}{dr} = -\frac{GM(<r)\rho_g(r)}{r^2}. \tag{3.5}$$

Inserting the equation of state for a perfect gas into the previous equation, one can write $M(<r)$ as

$$M(<r) = -\frac{k_B T r}{G\mu m_p}\left(\frac{d\ln\rho}{d\ln r} + \frac{d\ln T}{d\ln r}\right). \tag{3.6}$$

This expression is commonly used to estimate the gravitational mass of galaxy clusters and groups from the measurements of temperature and gas density profiles with X-ray observations. It clearly relies on the hypothesis of hydrostatic equilibrium and spherical symmetry. A common way to simplify the previous expression is to use the so-called β-model (Cavaliere and Fusco-Femiano, 1976), consisting in further assuming that the galaxy distribution is isothermal and thus that the gas density profile can be written as

$$\rho_g(r) = \rho_0\left[1 + \left(\frac{r}{r_{core}}\right)^2\right]^{-\frac{3}{2}\beta}, \tag{3.7}$$

while the observed surface brightness profile at projected radius b is of the form

$$I(b) = I_0\left[1 + \left(\frac{b}{r_{core}}\right)^2\right]^{\frac{1}{2}-3\beta}. \tag{3.8}$$

Here r_{core} is a suitable scale radius and β is defined as

$$\beta = \frac{\sigma_r^2}{kT/\mu m_p} \tag{3.9}$$

where σ_r is the galaxies line-of-sight velocity dispersion. This model is self-consistent and permits to rewrite Eq. 3.6 as

$$M(< r) = -\frac{k_B r^2}{G\mu m_p}\left[\frac{3\beta r T}{r^2 + r_{core}^2} - \frac{dT}{dr}\right] \tag{3.10}$$

and thus to obtain the total mass profile of a galaxy cluster from the observed gas temperature profile.

3.1.3 Dark matter density profiles

Dark matter is the main component of galaxy clusters. N-body cosmological simulations predict that radially-averaged dark matter halos profiles on all mass scales can be described by the Navarro-Frenk-White profile, which was extensively discussed in Sect. 2.2.5. Nevertheless, the same simulations show that there is a considerable scatter in measurements of profile shapes of different clusters, as demonstrated by Meneghetti et al., 2014 (Fig. 3.2). In fact Sand et al., 2004, studying a sample of six strong lensing clusters, found that the inner slope is consistent with $\beta \approx 0.52$ and inconsistent with $\beta \gtrsim 1$. Similarly, a lensing analysis of the cluster Abell 383 by Newman et al., 2011 shows that the inner slope of the density profile is < 1 at 95% confidence level. Analogous results are reported by Newman et al., 2009 for Abell 611, while findings of Newman et al., 2011 on a sample of seven massive clusters suggest a steep inner slope $\beta > 1$. In any case, it is clear that density profile of single clusters can depart from the NFW.

3.1.4 Concentration-mass relation

The halo concentration is a decreasing function of the host halo mass and depends on redshift, since on average halos at higher redshift are less concentrated. This result, found in numerical simulations, is explained in terms of halo formation history: massive halos which formed recently have suffered major mergers in recent times, so they are less concentrated. From the observational point of view, the c-M relation was studied with gravitational lensing (e.g. Meneghetti et al., 2014), X-ray observations (e.g. Ettori et al., 2010) or through the dynamical analysis of cluster members (e.g. Biviano et al., 2013). In this work we use the concentration-mass-redshift relation provided by Meneghetti et al., 2014, fitted by

$$c(M, z) = A\left(\frac{1.34}{1+z}\right)^B \left(\frac{M}{8 \times 10^{14} h^{-}1 M_\odot}\right)^C \tag{3.11}$$

The values of A, B, C found with the 3-dimensional fitting of observed galaxy clusters with NFW profiles are $A = 3.757 \pm 0.054, B = 0.288 \pm 0.077, C = -0.058 \pm 0.017$.

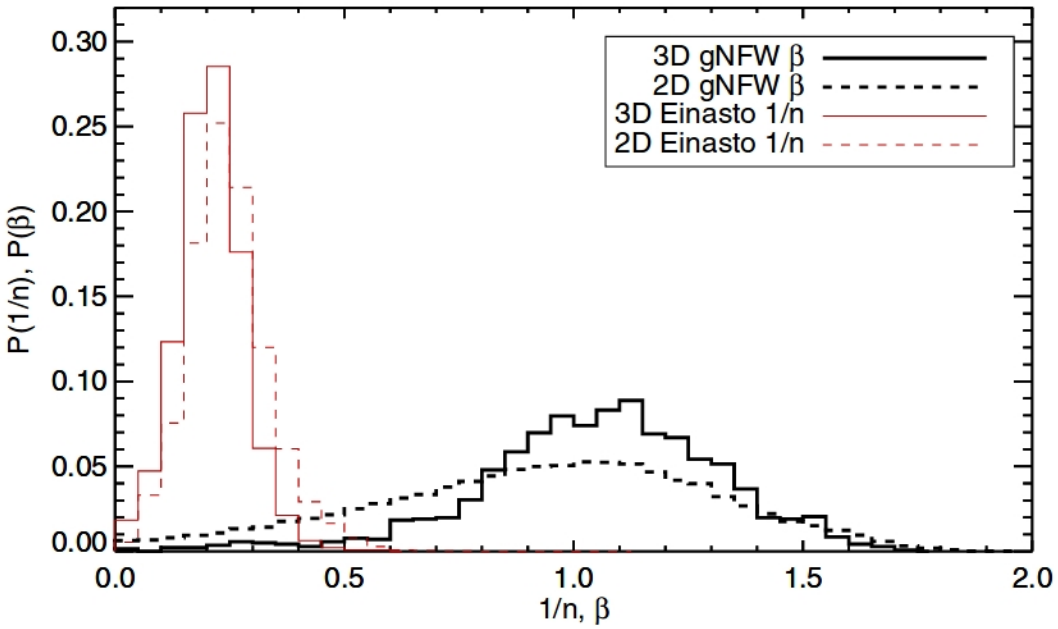

FIGURE 3.2: Distributions of the inner slopes obtained from the gNFW fits (β) and of the Einasto index $1/n$ derived from the analysis of the density (solid histograms) and of the surface-density profiles (dashed histograms) of halos in the MUSIC-2 cosmological simulation, as they result from fitting the halo density profiles with gNFW models (Meneghetti et al., 2014).

3.1.5 Subhalo mass function

As highlighted by Gao et al., 2004, the subhalo populations of different haloes found in the GIF2 cosmological N-body simulation[1] are not scaled copies of each other, but vary systematically with halo properties. On average, more massive haloes contain more subhaloes, and these subhaloes contain a larger fraction of the mass of the parent halo, due to their more recent formation. At given halo mass, subhaloes are more abundant in haloes which are less concentrated, namely formed more recently, because fewer substructures were destroyed by dynamical processes into the main halo. However, there is considerable scatter in the abundance of subhaloes in haloes of similar mass, concentration or formation time. This result probably reflects differences during the formation history of the halo.

As shown in Giocoli et al., 2010, the mass function of substructures found in the GIF2 simulations can be estimated taking into account the hierarchical formation history of halos: their best fit function is

$$\frac{1}{M_{vir}}\frac{dN(M_{vir}, c_{vir}, z_l)}{dm} = A(1+z_l)^{1/2}\frac{c^*}{c_{vir}}m^{\alpha}exp\left[-\tilde{\beta}\left(\frac{m}{M_{vir}}\right)^3\right] \tag{3.12}$$

where dN is the number of substructures with mass between m and $m+dm$, $A = 9.33 \cdot 10^{-4}$, $\tilde{\beta} = 12.2715$, $\alpha = -0.9$ and c^* is the mean concentration of a halo with mass M_{vir} at redshift z_l. As shown in Fig. 3.3 (left panel), it is a power-law function at low masses with an exponential cut-off at high masses.

[1] http://wwwmpa.mpa-garching.mpg.de/Virgo/

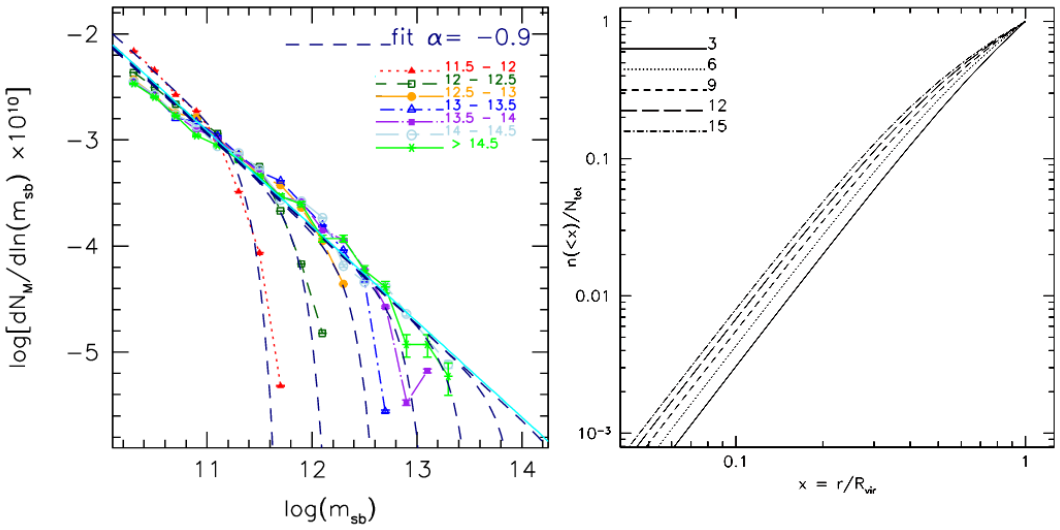

FIGURE 3.3: Left panel: Substructure mass function given by Eq. 3.12 per unit host halo mass (in units of $10^{10}/h\,\mathrm{M}_{\odot}$), at z=0. Host haloes are divided in seven different mass bins, shown in different colors. The solid line shows a power law distribution with slope $\alpha = -0.9$. The dashed lines show the fit to the data for each mass bin with the high mass exponential cut-off (adapted from Giocoli et al., 2010). Right panel: radial subhalo density distribution given by Eq. 3.13. The different curves show this distribution for different values of the host halo concentration c_{vir} (Giocoli et al., 2012).

3.1.6 Subhalo radial distribution

The radial distribution of subhaloes in GIF2 cosmological simulations it is found to be much less concentrated than that of the dark matter (Gao et al., 2004, Gao et al., 2012). Thus, substructures aren't good tracers of the total halo mass distribution. This radial profile do not depend on the mass of the subhaloes and has a weak dependence on the mass (or concentration) of the parent halo. Gao et al., 2004 find that the radial distribution of subhaloes appears "universal" and can be accurately fitted by the formula

$$\frac{n(<d)}{N_{tot}} = \frac{(1+ac_{vir})d^b}{(1+ac_{vir}d^2)} \tag{3.13}$$

where d is the distance from the host halo centre in units of the virial radius, N_{tot} is the total number of subhalos in the host, $a = 0.244$ and $b = 2.75$. This function is plotted in the right panel of Fig. 3.3 for different concentrations.

However, Eqs. (3.12) and (3.13) are based on results of dark matter-only simulations. The correspondence between simulated dark matter halos and galaxies it is not trivial, since baryons are expected to play an important role in galaxy formation and evolution. Processes like adiabatic contraction of baryons and AGN and supernovae feedback can affect the distribution of dark matter inside halos, resulting in a modification of density profiles. Moreover, condensation of baryons inside subhalos could increase their central density making them less affected by tidal disruption. This fact could cause an increase of subhalos abundance close to the halo center. Anyway, in lensing analysis it is common to assume that galaxies are good tracers of dark matter substructures (especially when the "simply-parametrized" or

the "light-trace-mass" approaches are used, see Sect. 3.2.1). In this work we adopt the same hypothesis.

3.2 Gravitational lensing in galaxy clusters

3.2.1 Strong lensing

Some examples of strong lensing effects due to galaxy clusters are visible in Fig. 3.8, relative to the cluster MACS0416. In this cluster there are 37 families of multiple images known to date, some of which results in highly distorted arcs (e.g. images 5b and 5c in the same figure). These strong lensing events allow the mass modeling of the clusters itself. Once it is established, thanks to spectrophotometric measurements, that many images belong to the same source, their positions and redshifts can be used for constraining gravitational lensing models of the cluster, through the process called *lens inversion*. If many sets of multiple images are available, it is possible to determine the position of critical curves, thus obtain an estimate of the projected mass they enclose within their area A_c. Thus, an effective Einstein radius can be defined as

$$\theta_E = \sqrt{\frac{A_c}{\pi}}. \tag{3.14}$$

For an axially symmetric lens, the average projected mass enclosed by the Einstein radius is the critical density, so we can write

$$M_{2D}(< \theta_E) = \pi (D_L \theta_E)^2 \Sigma_{crit}, \tag{3.15}$$

while for a generic mass distribution the enclosed projected mass profile it is given by

$$M_{2D}(< \theta) = \Sigma_{crit} D_L^2 \int_{|\vec{\theta'}|<\theta} \kappa(\vec{\theta'}) d^2\theta'. \tag{3.16}$$

Mass measurements based on the previous equations are more precise near θ_E, where different modeling assumption tend to agree within a few percent (Meneghetti et al., 2016).

Approaches used for the mass modeling are of many types. Three classes of strategies often used in strong lensing studies are the "simply-parametrized", the "free form" and the "light-trace-mass". Simply parametrized models try to reproduce the mass distribution with a set of physically motivated components, described each by a small number of parameters, representing the galaxies in the cluster and the overall cluster halo (see e.g. Kawamata et al., 2016). On the other hand, free form models are particularly flexible, since they are made out of components which are not associated with any specific physical object and used as building blocks (see, for example, Diego et al., 2016). Finally, light-trace-mass model are build assuming that light approximately traces mass, so mass components are obtained smoothing and rescaling the observed surface brightness of cluster members (Zitrin et al., 2015).

3.2.2 Galaxy-galaxy strong lensing

In dense environments like galaxy clusters it is not rare to observe galaxy-galaxy strong lensing (GGSL) events, namely cluster members acting as strong lenses on some background source. Here below, we illustrate only few examples of GGSL events.

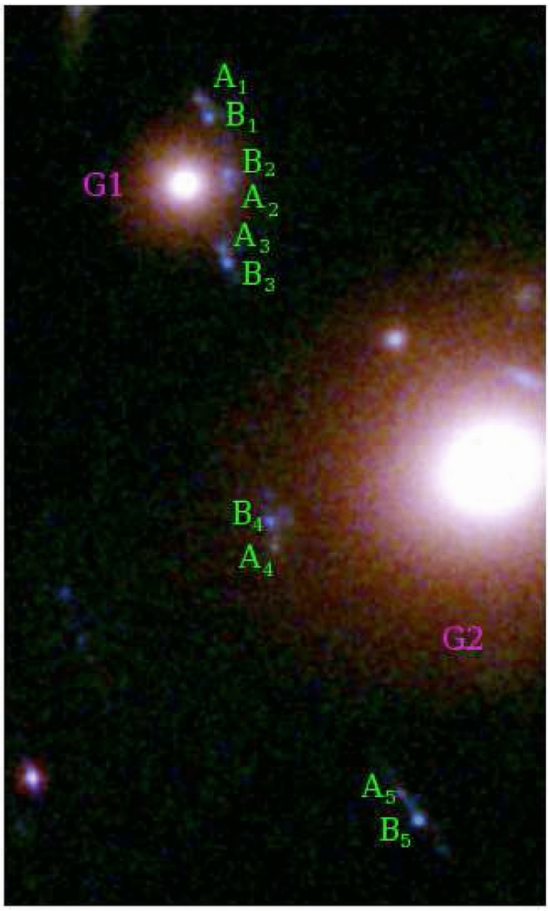

FIGURE 3.4: Color composite image of the galaxy-galaxy strong lensing event in the cluster MACSJ1206 reported by Grillo et al., 2014. Five multiple images of a source with a bimodal structure (at $z \approx 3.7$) are visible around two lens cluster galaxies (at $z = 0.44$), G1, near the top, and G2, in the middle.

MACSJ1206 hosts at least 2 GGSL events. The first system, described in Grillo et al., 2014 and visible in Fig. 3.4, consists of a total of ten multiple images belonging to two different sources at $z \approx 3.7$. In the second one, shown in Fig. 3.5, a source forms an Einstein ring around an elliptical galaxy of the cluster. Finally, Bradley et al., 2014 reports spectroscopic observations of a tangential arc, in which the source exhibits a clear emission line at 8146 Å, corresponding to $Ly\alpha$ at $z = 5.701$ (Fig. 3.6). However, the lens is not a cluster member in this case, but a foreground galaxy. Parry et al., 2016 report the discovery of a galaxy-galaxy strong lensing event in the cluster MACSJ1115. Here, two cluster members (G1 and G2 in Fig. 3.7) act as lenses causing the formation of a quadruple image system around G1. The modeling of these systems allows to constrain the dark matter fraction in G1 and G2, demonstrating how these kind of events can give us information on the influence that dark matter has on the structure and evolution of the inner regions of galaxies. Caminha et al., 2016 report a galaxy-galaxy lensing system in MACS0416, shown in Fig. 3.8 (top-right inset). In this case, three images of the same source at $z = 3.2215$ (spectrscopic redshift measured in MUSE spectra) are formed around two cluster galaxies. A special galaxy-galaxy strong lensing event is that discovered in MACSJ1149 by Kelly et al., 2015. During November 2014, thanks to Grism Lens-Amplified Survey from Space

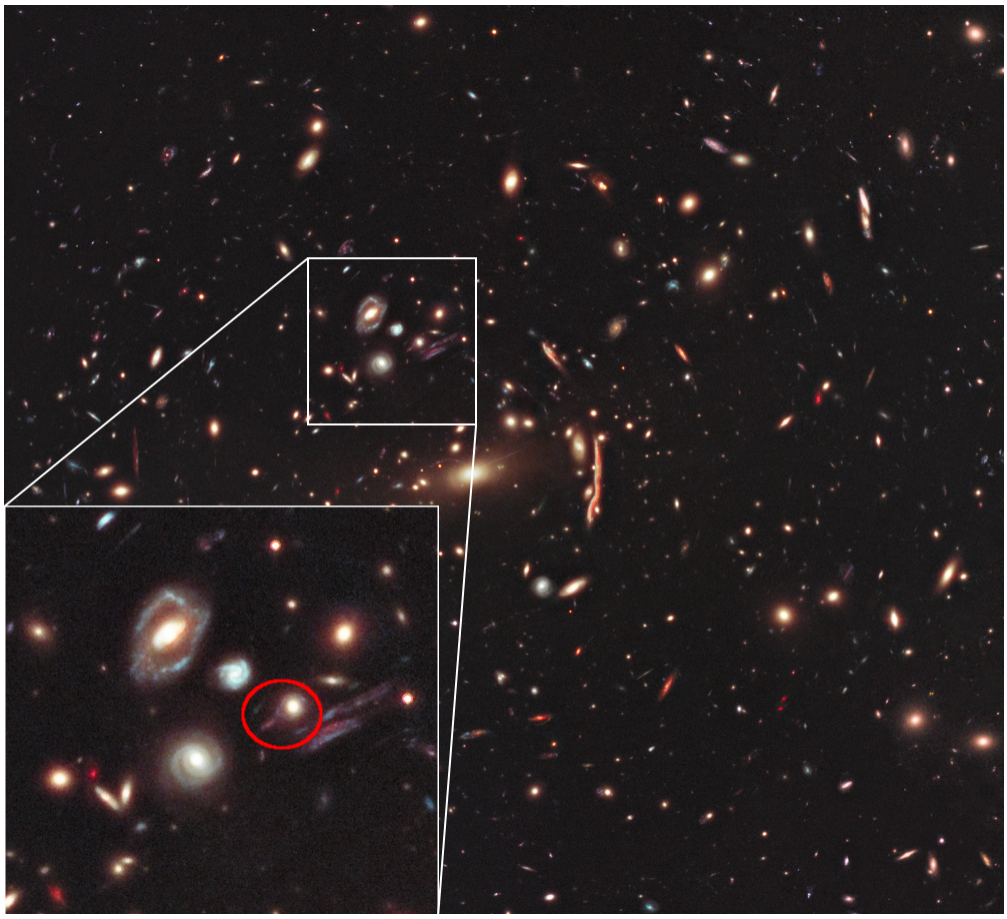

FIGURE 3.5: Complete Einstein ring around a cluster member in the cluster MACSJ1206.

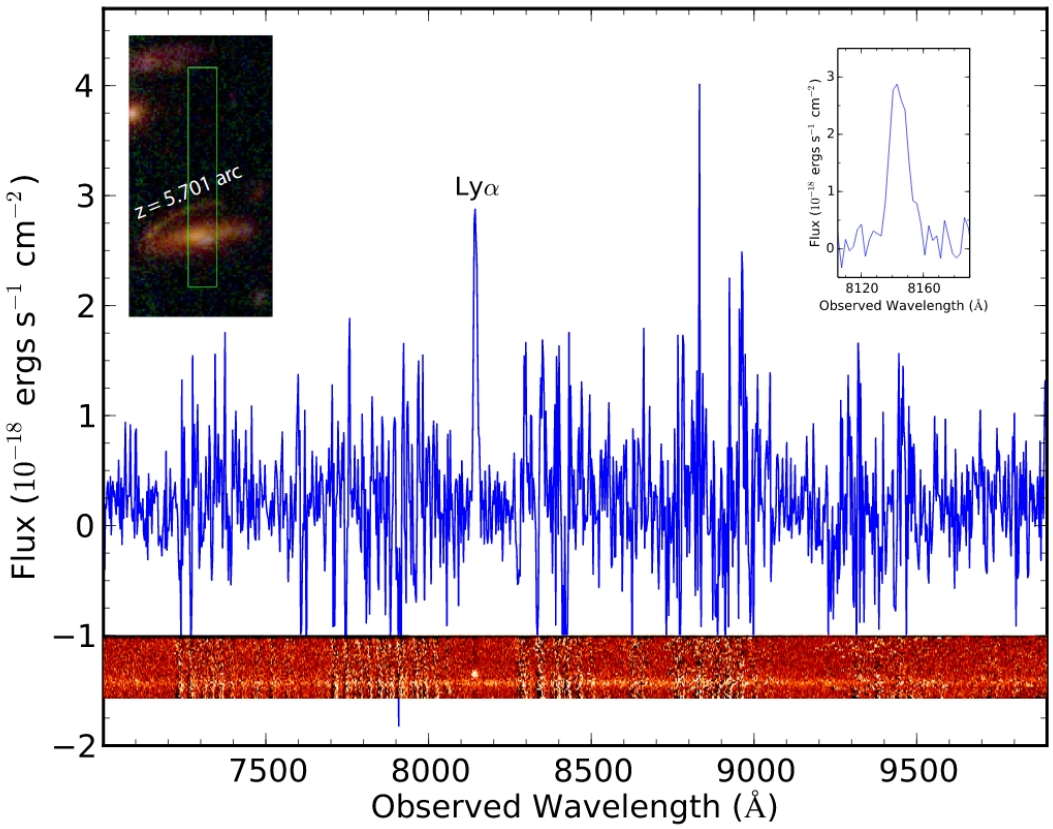

FIGURE 3.6: Observed 1D longslit spectrum of MACS1206-179 obtained with VLT/VIMOS as part of the CLASH VLT program (PI: P. Rosati). The spectrum exhibits a clear emission line at 8146 Åcorresponding to $Ly\alpha$ at z= 5.701 overlapped to the continuum spectrum of an early type galaxy. The upper-left inset shows the slit location. The upper-right insert shows a close up of the emission line, which shows an asymmetric profile suggestive of $Ly\alpha$. The 2D spectrum is shown along the bottom of the plot (from Bradley et al., 2014).

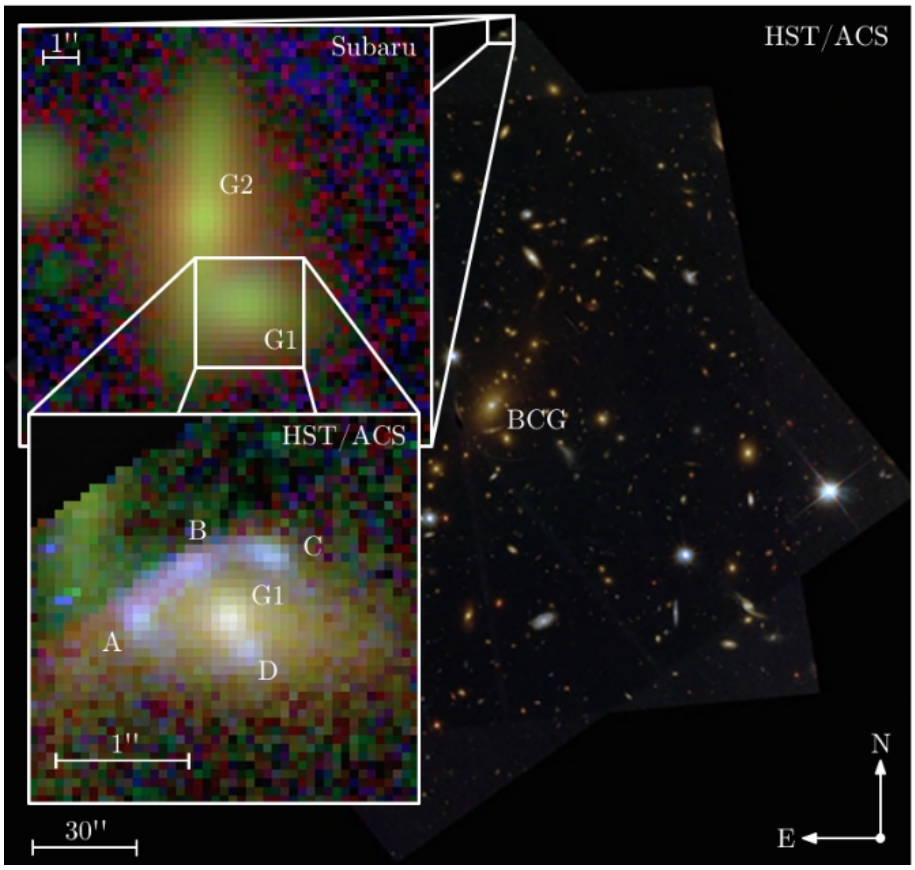

FIGURE 3.7: Colour-composite images of the strong lensing system in the cluster MACSJ1115 obtained with Subaru and HST/ACS. The high angular resolution of the HST/ACS data allows to resolve the multiple images (A, B, C and D) of the background source. The two main lenses, G1 and G2, are members of the galaxy cluster, with G1 located approximately 120″ away from the BCG (from Parry et al., 2016).

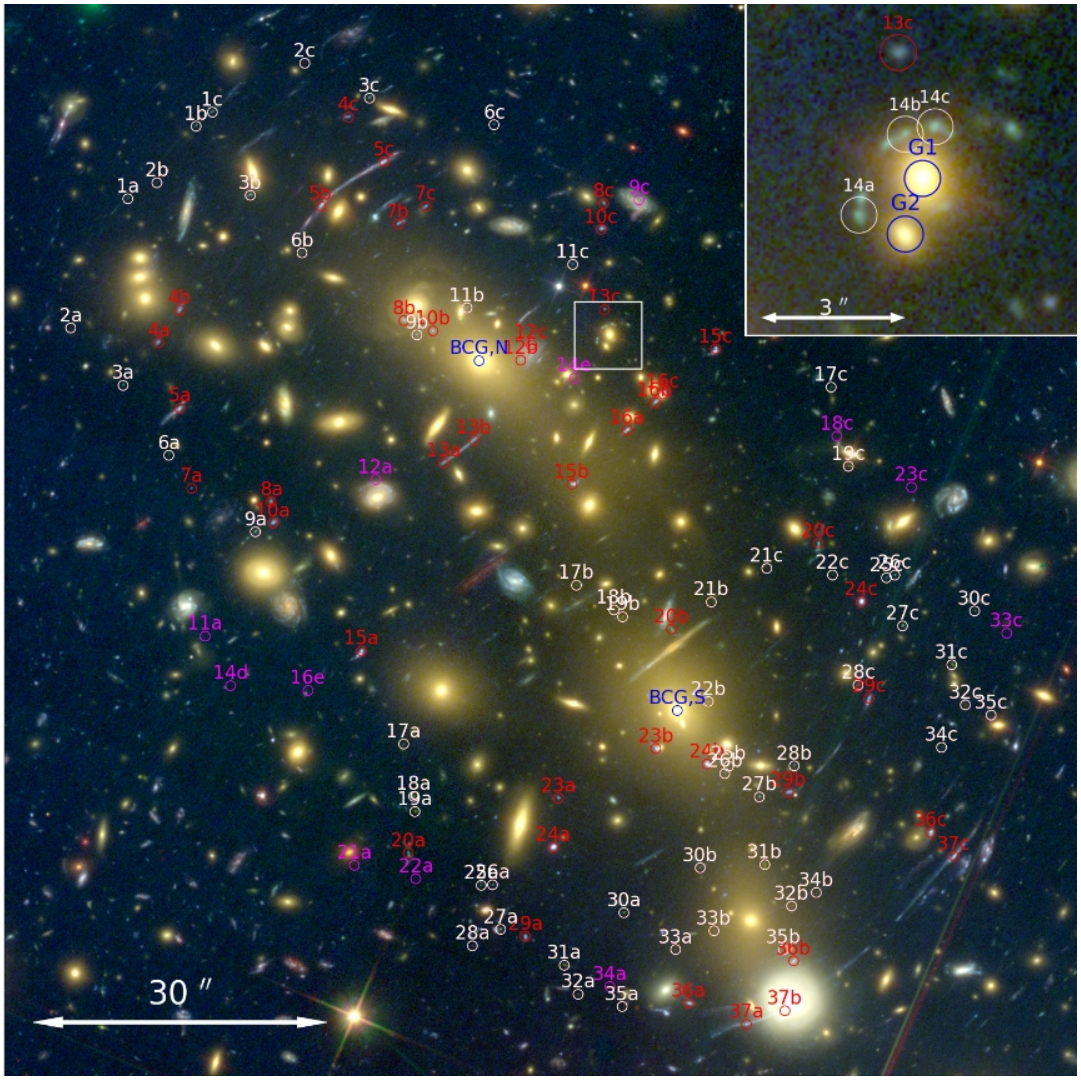

FIGURE 3.8: Color composite image of the cluster MACSJ0416 from Hubble Frontier Fields data. White and red circles mark the positions of multiple images with known spectroscopic redshifts. The inset is a blow-up of the region around family 14, around two galaxy cluster members, G1 and G2. The blue circles indicate the positions of the BCGs (BCG,N and BCG,S) (from Caminha et al., 2016).

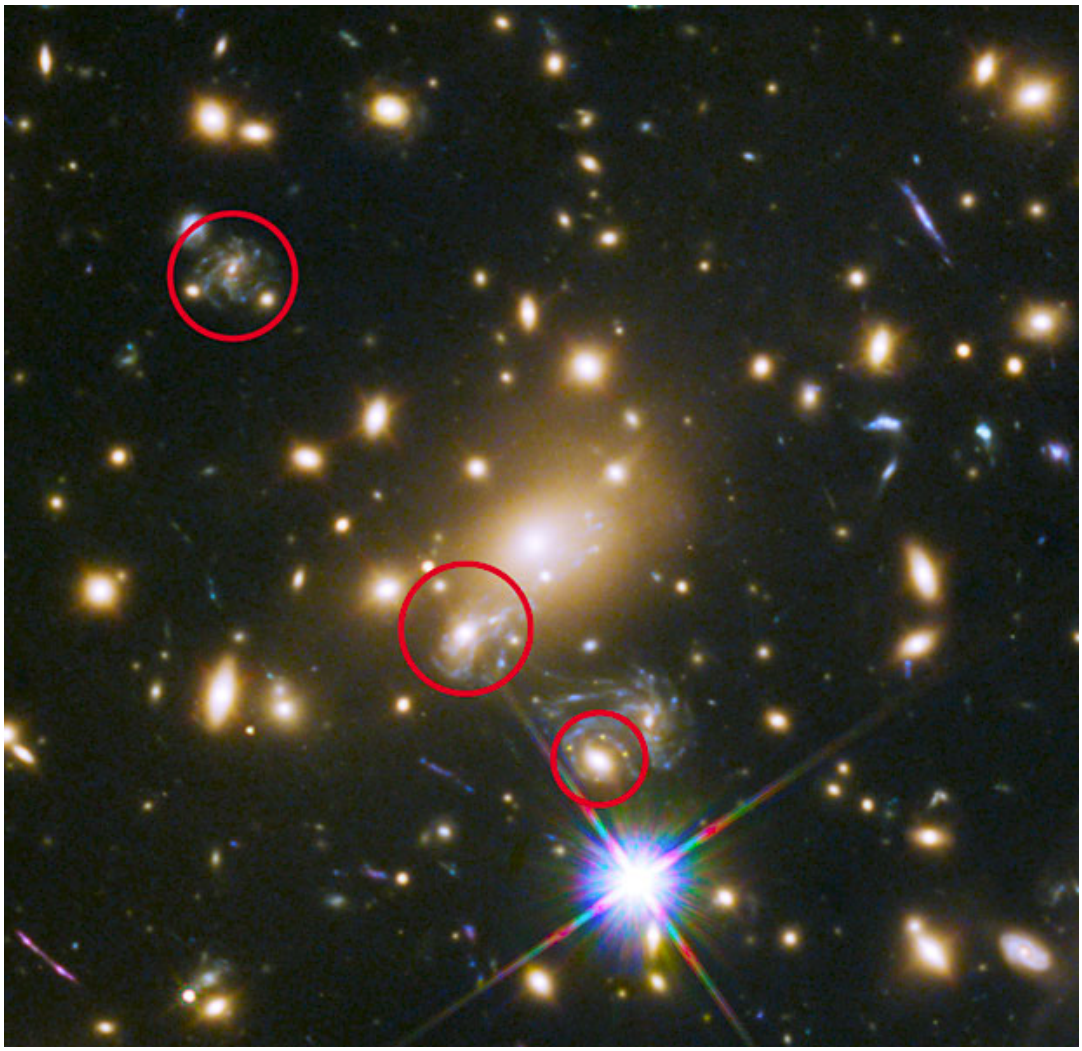

FIGURE 3.9: Inner region of the cluster MACSJ1149 ($z = 0.544$). The three red circles marks the positions of the multiple images of the same background spiral galaxy ($z = 1.489$). In the bottom-right circle are visible, as yellow dots, the four images of the Supernova Refsdal, lensed by a cluster member.

(GLASS, Treu et al., 2015) observations, it was discovered the first multiply imaged Supernova (SN), nicknamed "SN Refsdal". SN Refsdal appears as an Einstein Cross around an elliptical cluster member, and it is hosted in an arm of a background spiral galaxy at redshift 1.489 that is triply imaged too by the cluster potential. Due to time delays between different images, SN Refsdal was observed approximately one year later in one of the other two images of the spiral galaxy, while in the other image the Supernova was visible some decades ago (Fig. 3.9).

In general, galaxy-galaxy strong lensing systems add informations useful to improve the reconstruction of the cluster mass distribution. On the other hand, these events also allow to constrain the mass of the lens galaxies and of the dark matter substructures which host them. In fact, many efforts have been dedicated to characterize CDM substructures even on sub-galactic scales, in clusters or in galaxies. Previous attempts to use lensing to constrain substructures in galaxies include anomalous flux ratio between multiple images around the lens. Dalal and Kochanek, 2002

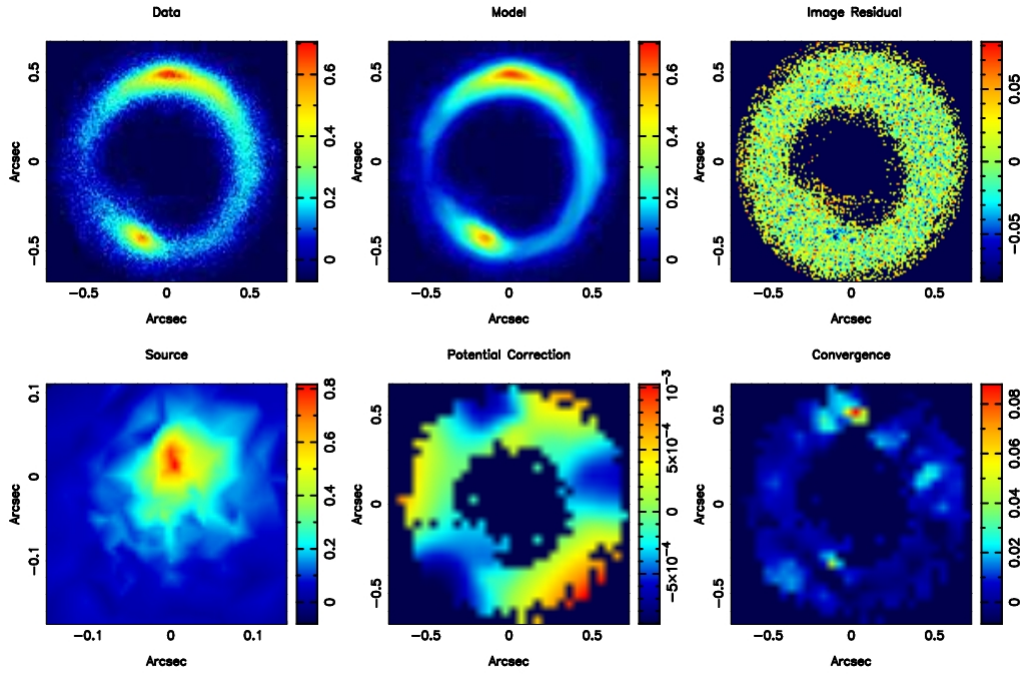

FIGURE 3.10: The detection of a dark-matter dominated satellite in the gravitational lens system B1938+666 at redshift 0.881. The data shown here are at 2.2 micron and were taken with the W. M. Keck telescope. Top-left panel: the original data set with the lensing galaxy subtracted. Top-middle panel: the final reconstruction. Top-right panel: the image residuals. Bottom-left panel: the source reconstruction. Bottom-middle panel: the potential correction from a smooth potential required by the model to fit the data. Bottom-right panel: the resulting dimensionless projected density corrections. A strong positive density correction is found on the top part of the lensed arc. From Vegetti et al., 2012.

show the potentiality of this methods on a sample of seven galactic lenses, finding a good agreement between observed mass fraction in substructures and CDM predictions. Subhalos can be identified also by studying surface brightness fluctuations in highly magnified Einstein rings, using a technique named "gravitational imaging". First of all, a smooth parametric model for the lens potential is built by using the surface brightness emission from the Einstein ring; next the best-fit model is further refined using local potential corrections defined on a regular grid, and then translated into surface density corrections. This technique is used by Vegetti et al., 2012, who reports the detection of a $1.9\times10^8\ \mathrm{M}_\odot$ dark satellite of a massive elliptical galaxy at $z = 0.881$. This galaxy act as lens for a background source at $z = 2.059$, which forms an almost complete Einstein ring with diameter ≈ 0.9 arcseconds. These images (at 1.6 and 2.2 micron) are taken using the Near Infrared Camera (NIRC2) on the W . M. Keck 10-m telescope, equipped with an adaptive optics system. This lens is shown in Fig. 3.10. Other examples of successful application of the gravitational imaging technique can be found in Vegetti et al., 2010 and Vegetti and Vogelsberger, 2014.

Moreover, important results in dark matter substructures detection are obtained with the ALMA interferometer. Hezaveh et al., 2016 reports the detection of a $10^{8.96}\ \mathrm{M}_\odot$

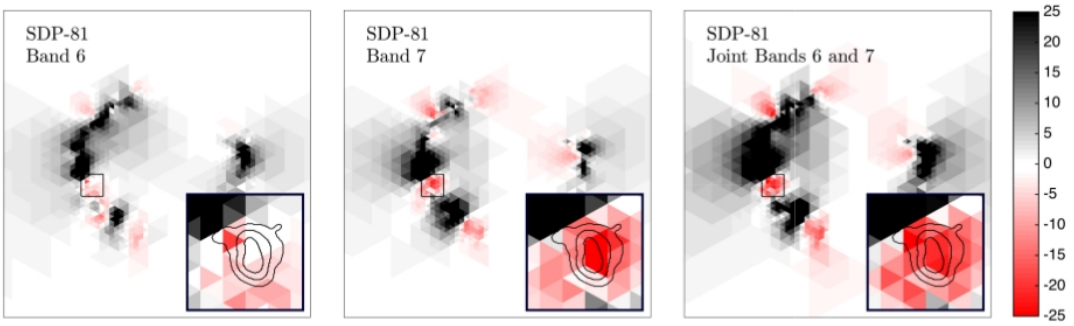

FIGURE 3.11: Maps showing the enhance to the fit of observed arc brightness provided by the addition of a substructure to the smooth lens model, as a function of the location of the substructure. Black means low improving, red means high improving. The three panels correspond to the analysis of ALMA Band 6 only (left), Band 7 only (middle), and joint Bands 6 and 7 (right). From Hezaveh et al., 2016.

subhalo in the strong lensing system SDP.81, studying the astrometric anomaly of the gravitational arc (Fig. 3.11).

3.2.3 GGSL in numerically simulated galaxy clusters

Since many galaxy-galaxy strong lensing events were observed, it is interesting to ask ourselves what is the GGSL signal predicted by cosmological simulations. In particular, here we focus on numerical simulations of galaxy clusters, considering the hydrodynamical simulations presented by Rasia et al., 2015. This clusters sample is also dubbed "Dianoga". With the aim to investigate the role of gas physics and feedback processes in the evolution of the intra cluster medium, they performed high-resolution zoomed simulations of galaxy clusters extracted from the *Magneticum* cosmological simulation. They consists of 24 massive cluster with M_{500} between 5 and $20 \times 10^{14}\ h^{-1}M_{\odot}$ and 5 poorer clusters with M_{500} in the range $0.7 - 3 \times 10^{14}\ h^{-1}M_{\odot}$ [2]. Simulations are carried out with the GADGET-3 code and include the effects of stellar and AGN feedback and of gas radiative cooling. Dark matter particles have masses of $8.3 \times 10^{8}\ h^{-1}M_{\odot}$. Using the technique described in Meneghetti et al., 2016, the Dianoga clusters have been studied using the "ray-tracing" method. By computing the deflection fields of these clusters we were able to determine their critical lines. These are shown, overlapped to the cluster convergence maps, in Fig. 3.12. The critical lines refer to sources at $z_s = 3$. As it can be seen, there are no critical lines around substructures. This means that the predicted galaxy-galaxy strong lensing signal is extremely small, since no multiple images of background sources can form around member galaxies. For comparison, Fig 5.11 shows the critical lines of the strong lensing model of the cluster MACSJ1149 by Kawamata et al., 2016. At $z_s = 3$ (right panel) many secondary critical lines are visible, even if the observed filed of view is smaller than those of Dianoga simulations. The discrepancy between these findings and observations of clusters of similar mass may indicate some limitations of the simulations. A possible explanation of the lack of GGSL in simulations could be the spatial and mass resolution of the latter. In fact, too high dark matter particle masses or too large softening lengths can make critical lines around substructures

[2] With M_{500} we mean the mass enclosed within a radius encompassing the region whose density is 500 times the critical density of the universe.

unresolvable. Alternatively, the reason they not form may have other explanations and be due to incorrect assumptions on the nature of DM or in the baryon physics.

The main goal of this thesis is to investigate with more details this apparent inconsistency between theory and observations. If this mismatch is real, we aim to find its origin. To pursue our goal, we make use of simulations of galaxy clusters realized with the semi-analytical techniques extensively exposed in the next chapter. In this way, we can build lensing maps with an arbitrary high mass and spatial resolution. During the work, we also study how the probability to observe galaxy-galaxy strong lensing events is influenced by the physical properties of clusters and substructures within them. In particular, we focus our attention on two properties of the cluster mass profile: its concentration and inner slope. Since these parameters describe how matter is distributed inside the main halo, they could affect the lensing power of substructures. Moreover, investigate how the radial distribution function and the mass function of subhalos affect the probability to observe GGSL events.

3.2.4 Weak lensing

The weak lensing regime is characterized by small values of convergence and shear, namely $\kappa, \gamma \ll 1$. In such a situation, there is no multiple imaging or high distortion of background sources: the only effect is a slightly distortion of background galaxies. Since we do not know the true shapes of the observed galaxies, informations about the weak lensing signal has to be extracted statistically.

Images of background galaxies are described by their surface brightness $I(\vec{\theta})$, where $\vec{\theta}$ is the position on the image plane. The luminosity center of the image is given by

$$\vec{\theta} = \frac{\int d^2\theta q_i[I(\vec{\theta})]\vec{\theta}}{\int d^2\theta q_i[I(\vec{\theta})]} \tag{3.17}$$

where q_i is a cut-off function that truncates the brightness profile at some isophotal level. The tensor of the second moments of the brightness distribution is given by

$$Q_{ij} = \frac{\int d^2\theta q_i[I(\vec{\theta})](\theta_i - \bar{\theta_i})(\theta_j - \bar{\theta_j})}{\int d^2\theta q_i[I(\vec{\theta})]}, \tag{3.18}$$

from which one can define the complex ellipticity

$$\epsilon = \epsilon_1 + i\epsilon_2 = |\epsilon|e^{2i\phi} = \frac{Q_{11} - Q_{22} + 2iQ_{12}}{Q_{11} + Q_{22} + 2(Q_{11}Q_{22} - Q_{12}^2)^{1/2}}. \tag{3.19}$$

The same arguments apply for the true surface brightness of the source, for which we can define the brightness tensor $Q^{(s)}$. The image distortion due to the weak lensing is described by the Jacobian matrix introduced in sec. 2.1.3, thus

$$Q^{(s)} = AQA^T = AQA. \tag{3.20}$$

The last equality is translated in terms of complex ellipticities as

$$\epsilon^{(s)} = \begin{cases} \frac{\epsilon - g}{1 - g^*\epsilon} & \text{if} \quad |g| \leqslant 1 \\ \frac{1 - g\epsilon^*}{\epsilon^* - g^*} & \text{if} \quad |g| > 1 \end{cases} \tag{3.21}$$

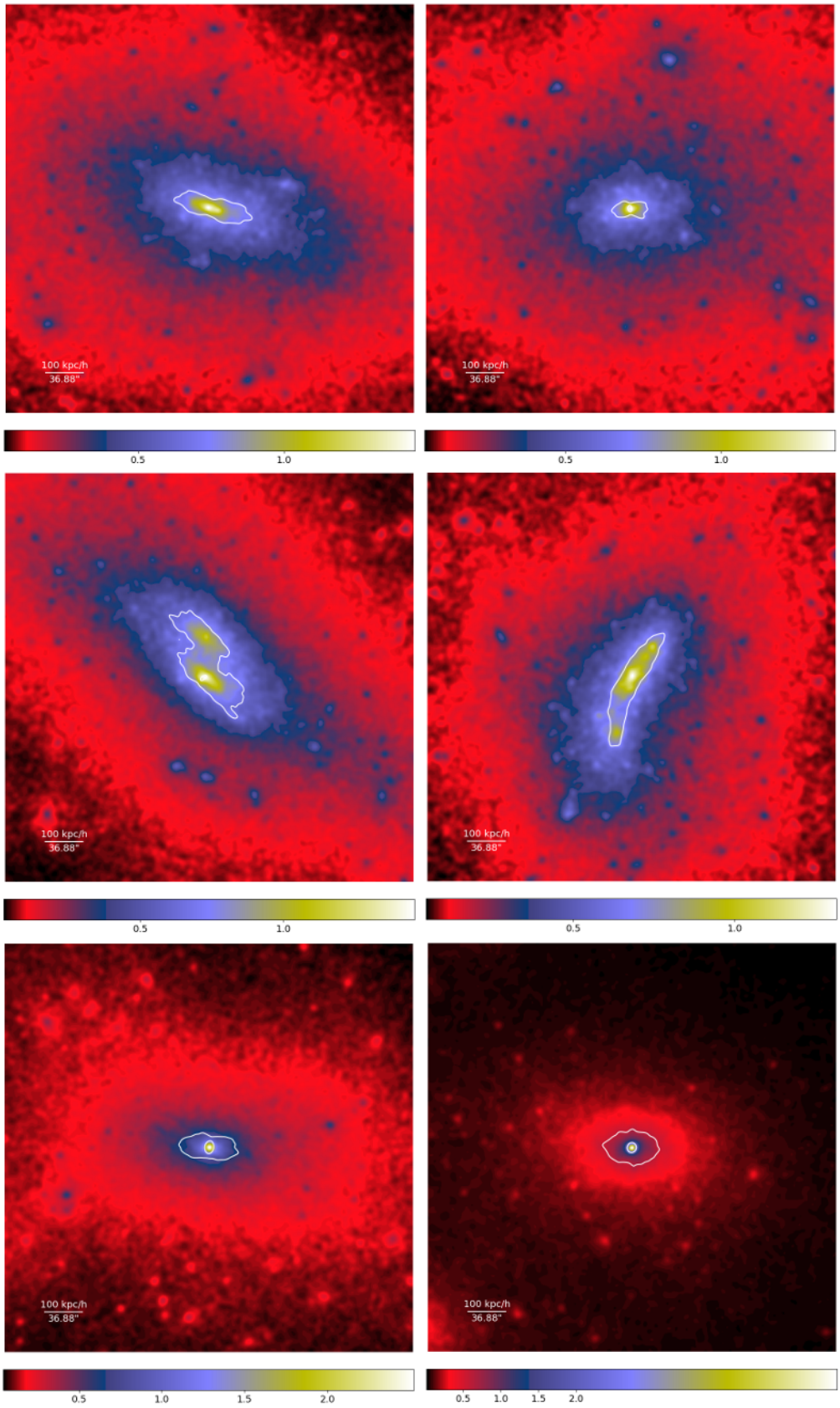

FIGURE 3.12: Convergence maps of clusters extracted from the cosmological hydrodynamical simulations of Rasia et al., 2015 for a source redshift $z_s = 3.0$. Critical lines are shown in white: even if substructures are present, they not produce secondary critical lines. The scale of each figure is shown in each panel.

where ϵ and ϵ^s are the complex ellipticities of the image and of the source and g is the complex reduced shear

$$g(\vec{\theta}) = g_1 + ig_2 = |g|e^{2i\phi} = \frac{\gamma(\vec{\theta})}{\kappa(\vec{\theta})}. \tag{3.22}$$

The symbol * denotes the complex conjugation. The inverse relation is given by

$$\epsilon = \begin{cases} \frac{\epsilon^{(s)}+g}{1+g^*\epsilon^{(s)}} & \text{if} \quad |g| \leqslant 1 \\ \frac{1+g\epsilon^{(s)*}}{\epsilon^{(s)*}+g^*} & \text{if} \quad |g| > 1. \end{cases} \tag{3.23}$$

Assuming that the intrinsic average source complex ellipticity $\epsilon^{(s)}$ is zero (namely that the phases ϕ are random for unlensed sources), we obtain that the measured average ellipticity of images is

$$\langle\epsilon\rangle = \begin{cases} g & \text{if} \quad |g| \leqslant 1 \\ \frac{1}{g^*} & \text{if} \quad |g| > 1. \end{cases} \tag{3.24}$$

Recalling Eqs. 2.14, 2.17, 2.22, which relate convergence and shear with the lensing potential, one can derive the following relation involving the Fourier-Space transformations $\hat{\kappa}$ and $\hat{\gamma}$ of κ and γ:

$$\hat{\kappa} = \kappa^{-2}\left[(\kappa_1^2 - k_2^2)\hat{\gamma_1}) + 2\kappa_1\kappa_2\hat{\gamma_2}\right]. \tag{3.25}$$

Applying the convolution theorem and transforming back to real space, we obtain

$$\kappa(\vec{\theta}) - \kappa_0 = \frac{1}{\pi}\int d^2\theta' D^*(\vec{\theta} - \vec{\theta'})\gamma(\vec{\theta'}) \tag{3.26}$$

where

$$D(\vec{\theta}) = \frac{\theta_2^2 - \theta_1^2 - 2i\theta_1\theta_2}{|\vec{\theta}|^4}. \tag{3.27}$$

Evaluating $g(\vec{\theta})$ through ellipticity measurements, studying the previous integral it is possible to find the distribution $\kappa(\vec{\theta})$ that induces the observed mean shape distortion, namely that solves the equation for the given reduced shear (Kaiser and Squires, 1993).

3.3 Galaxy clusters surveys

In the last 30 years, many cluster surveys have been made with the primary goal of using lensing to study the mass distribution in these massive structures. Strong lensing observations with extremely high level of details became possible with the advent of the Hubble Space Telescope. In particular, in the last 6 years, HST has dedicated an enormous amount of orbits to carry out deep multiband observations of cluster fields in the framework of two surveys, namely the CLASH and the Frontier Field surveys. Since these are both relevant for this thesis work, we briefly introduce them here.

3.3.1 Cluster Lensing and Supernova Survey with Hubble

The Cluster Lensing and Supernova Survey with Hubble (CLASH) (Postman et al., 2012) targeted 25 massive galaxy clusters, observing each of them in 16 passbands. The survey goals are:

- the mapping of the distribution of dark matter in galaxy clusters using strong and weak gravitational lensing;
- the detection of Type Ia supernovae out to redshift $z \approx 2$;
- the detection and characterization of galaxies at $z > 7$, thanks to the magnification power of targeted galaxy clusters;
- the study of the internal structure and evolution of the galaxies in and behind these clusters.

With these aims, CLASH has been allocated 524 HST orbits, the majority of which (474) are for cluster imaging and, simultaneously, for the parallel SN search program. An additional 50 orbits were allocated as a reserve for SN follow-up observations. This results in a magnitude limit of ≈ 27.5 in the HST i band. The cluster sample covers a wide redshift range ($0.15 < z < 0.9$, with a median of $z \approx 0.4$), spans almost an order of magnitude in mass (from ≈ 5 to $\approx 30 \times 10^{14}\,\mathrm{M}_{\odot}$), and all have X-ray temperature > 5 keV. The total area of complete 16-filter coverage in every cluster is 4.07 square arcminutes. Observations were finished in 2013. Table 3.2 presents the 25 clusters observed in the CLASH program, four of which are shown in Fig. 3.13.

Cluster Name	Redshift	Cluster Name	Redshift
Abell 209	0.209	CLJ1226+3332	0.890
Abell 383	0.189	MACS1311-0310	0.494
MACS0329-0211	0.450	RXJ1347-1145	0.451
MACS0416-2403	0.396	MACS1423+2404	0.545
MACS0429-0253	0.399	RXJ1532+3021	0.363
MACS0647+7015	0.591	MACS1720+3536	0.391
MACS0717+3745	0.548	Abell 2261	0.224
MACS0744+3927	0.686	MACS1931-2635	0.352
Abell 611	0.288	MACS2129-0741	0.570
MACS1115+0129	0.353	RXJ2129+0005	0.234
MACS1149+2223	0.544	MS2137-2353	0.315
Abell 1423	0.214	RXJ2248-4431	0.348
MACS1206-0847	0.440		

TABLE 3.2: Clusters observed with HST during the CLASH survey. From Postman et al., 2012.

3.3.2 Hubble and Spitzer Fontier Fields

The Frontier Fields (Lotz et al., 2016) are a director's discretionary time program using the HST and the Spitzer Space Telescope to observe with unprecedented depth the 6 galaxy clusters liste in Tab. 3.3, known to be powerful strong lenses. The aim of the initiative is to combine the power of these telescopes with the magnification power of the six massive clusters of galaxies to observe sources which could not be

FIGURE 3.13: Inner regions of fours clusters observed with HST during the CLASH survey. Multiple images and gravitational arc are clearly visible in all panels.

detected otherwise. This observations allow to probe galaxies with optical/near-infrared magnitudes of $\approx$ 29, and 10 - 100 times fainter in regions of high magnification. Thus, HST observations of these strongly-lensed fields can probe galaxies as intrinsically faint or fainter than those detected in the Hubble Ultra Deep Field Initiative (Rafelski et al., 2015) in a much shorter exposure time.

Images are taken in seven HST bandpasses and in two additional Spitzer filters. The program were completed in September 2016 and the collected data constitute the foundation of many studies of gravitational lensing in galaxy clusters. In fact, in order to understand many of the properties of background lensed galaxies, reliable lensing models for each cluster are required. Five independent teams, using different approaches (see section 3.2.1) but the same input dataset, consisting in an unprecedented set of strong-lensed arcs and multiple images, developed lensing models for the six clusters[3].

[3]Lensing models of Frontier Fields clusters are availiable at http://www.stsci.edu/hst/campaigns/frontier-fields/Lensing-Models

Fig. 3.14 shows three Frontier Field clusters and their relative parallel fields observed by HST.

Cluster Name	Redshift	Cluster Name	Redshift
Abell 2744	0.308	MACS1149+2223	0.544
MACS0416-2403	0.396	RXJ2248-4431	0.348
MACS0717-3745	0.545	Abell 370	0.375

TABLE 3.3: Clusters observed with HST during the Frontier Fields survey (Lotz et al., 2016).

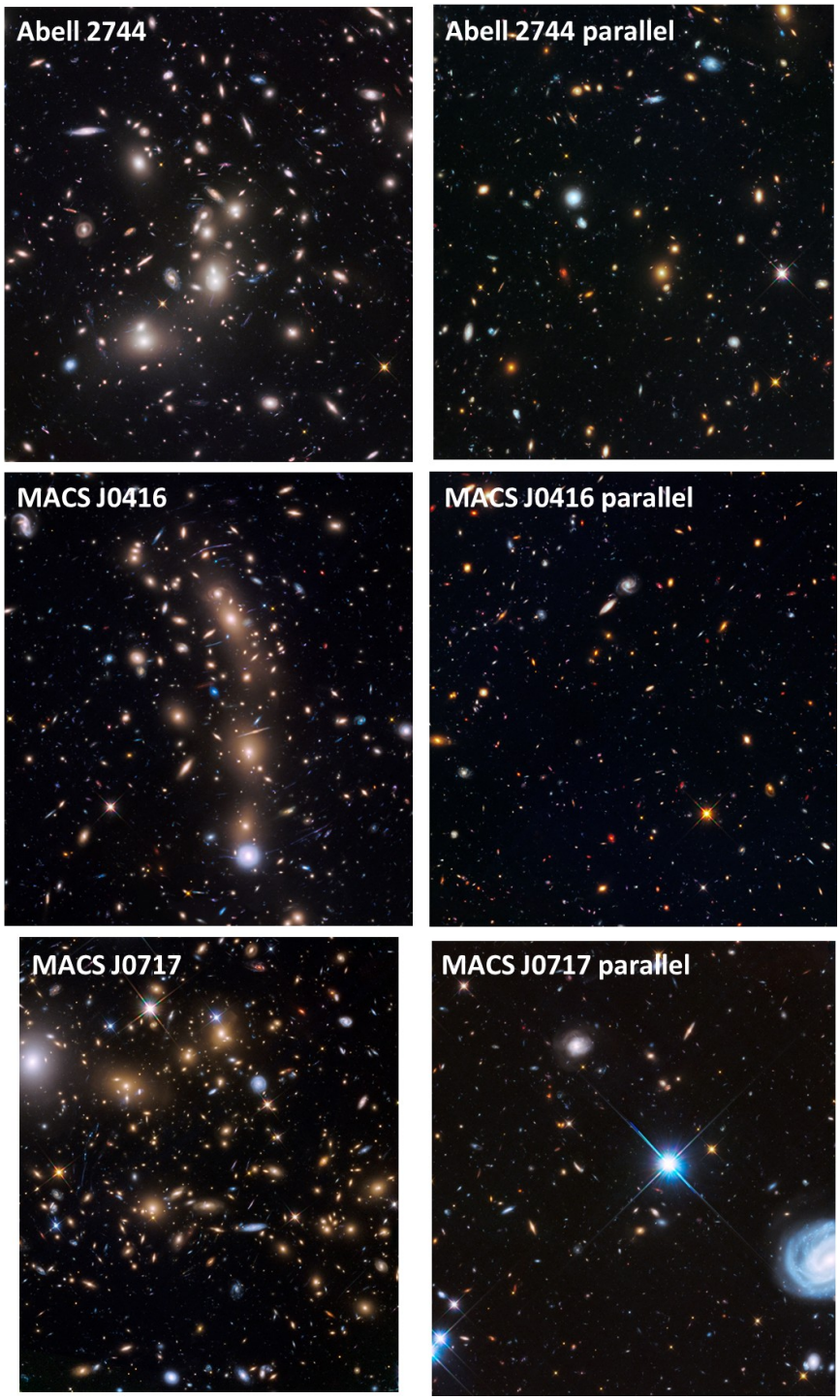

FIGURE 3.14: Three clusters (left) and their relative parallel fields (right) observed with HST during the Frontier Fields survey. The depth of these observations ($mag \approx 29$) allows to detect many more faint sources and lensing features with respect to CLASH survey (Fig. 3.13) thus to obtain better constrained lensing models.

Chapter 4

Simulations of gravitational lensing by galaxy clusters

In this chapter we describe the codes and the techniques used to produce and analyze the lensing simulations considered in this thesis work. We begin introducing the tools used to model complex lenses, then we discuss how to extract lensing informations from the produced maps. In particular, we describe a novel algorithm to locate critical lines around substructures, to map them onto caustics and to measure the galaxy-galaxy strong lensing (GGSL) cross section, the quantity we are interested in. This algorithm was integrated in a simulation pipeline, which is described in detail in the following sections.

4.1 Simulation software

4.1.1 MOKA

The first component of our simulation pipeline is the code MOKA (Matter density distributiOn Kode for gravitationAl lenses). This code is able to create realistic maps of substructured triaxial dark matter halos, whose properties are in agreement with those of galaxy clusters extracted from DM-only cosmological numerical simulations. Detailed information on this publicly available code[1] can be found in the reference paper (Giocoli et al., 2012). Here we summarize some of the features that are relevant to our project.

MOKA analytically calculates surface mass density distributions of halos formed by a smooth, triaxial matter distribution and by an ensemble of substructures. This code is particularly useful for our purposes, since maps can be calculated with an arbitrarily high resolution, both spatial and in mass. The user can choose to build halos with an NFW density profile, discussed in section 2.2.5, or with its generalization presented in section 2.2.6.

As highlighted in section 3.1.4 CDM simulations show that halo concentration is a decreasing function of mass and depends on the halo formation history. By default MOKA works with the following relation, proposed by Zhao et al., 2009:

$$c_{vir}(M_{vir}, z_L) = 4\left\{1 + \left[\frac{t(z_L)}{3.75 t_{0.04}}\right]^{8.04}\right\}^{1/8} \tag{4.1}$$

[1] MOKA can be downloaded from http://cgiocoli.wordpress.com/research- interests/moka

where $t_{0.04}$ is the time at which the main progenitor of the halo assembles 4% of its mass, z_L is the lens redshift and M_{vir} its virial mass. However, the user is free to use a tailored $c - M$ relation or to build clusters with given mass and concentration. If axial ratios are not imposed by the user, MOKA assigns a shape to the halo following the triaxiality distribution model given by Jing and Suto, 2002, based on dark matter simulations.

Substructures are introduced in the smooth halo using analytical fitting formulae to numerical simulations, and their properties are saved in catalogs readable by the user. The subhalo mass function is given in Eq. (3.12); masses m_i are assigned to substructures randomly sampling this distribution down to the minimal mass m_{min}, that can be chosen by the user. Unless otherwise specified, we used $m_{min} = 10^{10} h^{-1}$ $M_\odot$.

The subhalo cumulative spatial distribution is based on the work of Gao et al., 2004 and is given in Eq. (3.13). Substructures are placed in the main halo sampling this distribution and randomly assigning angular positions.

Substructures are modeled as SIS (see Eq. (2.37)), and the user can choose to truncate the profile at a radius $R_{sub} = G m_{sub}/2\sigma_v^2$. Many studies (Koopmans et al., 2009; Barnabè et al., 2011; Cappellari et al., 2015) shown that this profile well reproduce the total mass distribution (baryons plus dark matter) of elliptical galaxies.

It is possible to include a BCG at the halo centre, whose stellar density profile is described by the Hernquist profile

$$\rho_{star}(r) = \frac{\rho_g}{(r/r_g)(1 + r/r_g)^3} \tag{4.2}$$

with $r_g = 0.551 R_e$ and $R_e = 0.03 R_{vir}$ (Keeton, 2001), and ρ_g is the density at r_g. The total BCG stellar mass is

$$M_{star} = \frac{2 M_{star,0}}{(M_{infall/M_0})^{-\alpha''} + (M_{infall/M_0})^{-\beta''}} \tag{4.3}$$

with $\alpha'' = 0.39$, $\beta'' = 1.96$ and $\log M_{star,0} = 10.35$ and with a Gaussian scatter $\sigma_{M_{star}} = 0.148$ (Wang et al., 2006).

The total mass M_{vir} is thus subdivided as $M_{vir} = M_{smooth} + \Sigma_{i=1}^{N_tot} m_i + M_{star}$. It is possible to construct more complicated mass distribution with many smooth halos, each one populated with substructures as described above.

For every constructed mass distribution, the code computes the maps of the relevant lensing quantities defined in sections 2.1.2, 2.1.3. For example, in Fig. 4.1 we show maps of convergence and effective potential.

4.1.2 LENSTOOL

LENSTOOL (Jullo and Kneib, 2009) is a publicly available software [2] widely used to model strong lenses by fitting lensing constraints such as families of multiple images and highly distorted sources. To build these models, the user can opt for a variety of lens models with different density profiles and shapes. While the main purpose of this code is to fit observations, it can be used to produce lensing maps for customized mass distributions. In particular, we used it to study the properties of lenses based on the models produced with MOKA (total mass and substructures) but with density profiles not yet implemented in the MOKA code. To this goal, we adapted the output catalogs of MOKA to be imported by LENSTOOL.

[2] Lenstool and its manual can be found at https://projets.lam.fr/projects/lenstool/wiki

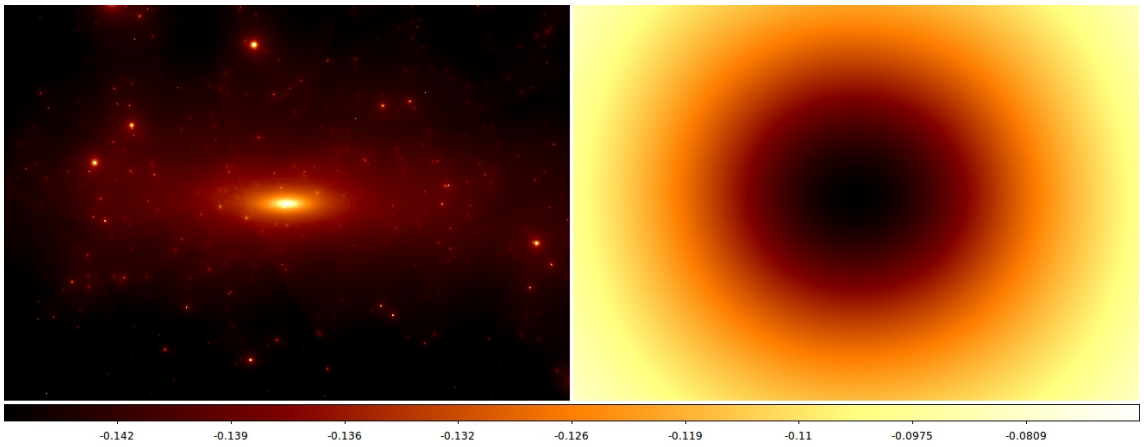

FIGURE 4.1: Convergence (left) and effective potential (right) maps calculated by MOKA, for a cluster of $10^{15}h^{-1}\,\mathrm{M}_{\odot}$ at $z = 0.5$ for a source plane at $z_S = 3.0$

4.2 A novel algorithm for galaxy-galaxy strong lensing in clusters

4.2.1 Extraction of critical lines and caustics

As we have seen earlier in this thesis, strong lensing events can be observed around galaxies in clusters. These events are the main focus of this work. We consider a galaxy or a substructure a strong lens when it has a tangential critical line which is well separated from the principal critical line of the cluster. We build an algorithm to locate these critical lines (which we call "secondary") and to compute the corresponding cross-section for strong lensing.

Thanks to equations (2.13) and (2.22), we can write convergence and shear in terms of deflection angles as

$$\kappa(\vec{x}) = \frac{1}{2}\vec{\nabla}\vec{\alpha}(\vec{x}) \tag{4.4}$$

$$\gamma_1(\vec{x}) = \frac{\partial\alpha_x(\vec{x})}{\partial x} - \frac{\partial\alpha_y(\vec{x})}{\partial y} \tag{4.5}$$

$$\gamma_2(\vec{x}) = \frac{\partial\alpha_x(\vec{x})}{\partial y} = \frac{\partial\alpha_y(\vec{x})}{\partial y} \tag{4.6}$$

so convergence and shear maps can be obtained from deflection angles maps trough partial derivatives. Thus, for every mass distribution considered, we calculate with LENSTOOL only deflection angle maps.

Tangential eigenvalue maps can be found by combining the convergence and the shear maps as shown in Eq. (2.25). Tangential critical lines correspond to the zero-level contours in this images. The zero-level contours are splitted in several groups of points, which correspond to the primary and secondary critical lines in the lens plane. For each group of points we follow the path around the corresponding lens, reconstructing all the critical lines. An example of the result of this procedure is shown in the left panel of Fig. 4.2, where the primary and the secondary critical lines identified in a simulation are shown in different colors. The implementation of this algorithm makes usage of several methods taken from the *matplotlib* graphical

PYTHON package[3]. Once the critical lines are reconstructed, we can use the lens equation (2.11) to map each of them on the source plane. This involves to interpolate the deflection angle maps at the location of the critical points. In the right panel of Fig. 4.2 we show the caustics corresponding to the critical lines shown in the left panel. The match between caustics and critical lines can be made using the color code. The above procedure can be applied to maps computed for different source redshifts.

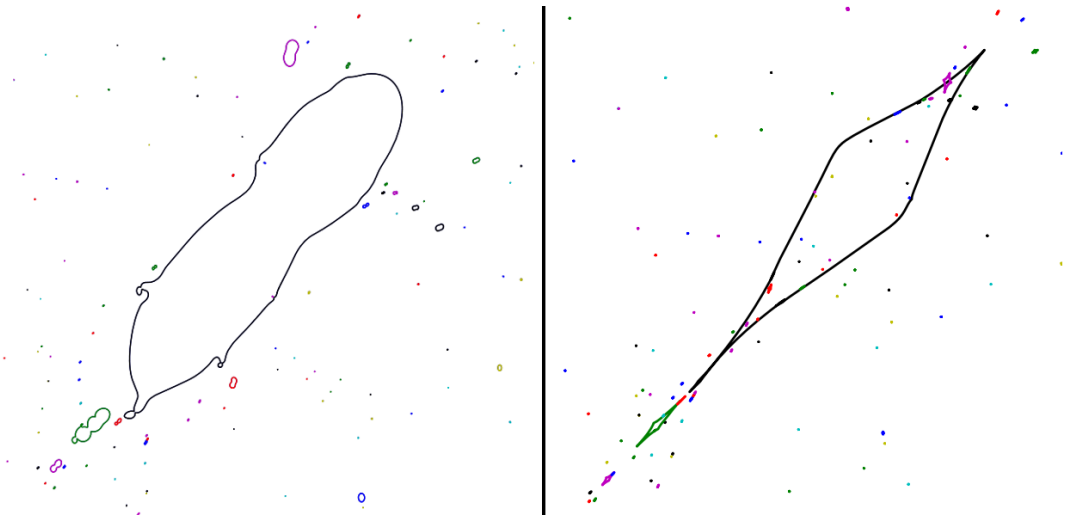

FIGURE 4.2: Left: critical lines in the central region of a simulated galaxy cluster of $10^{15}h^{-1}M_{\odot}$. Right: zoom on the corresponding caustics on the source plane. The match between critical lines and caustics can be done using the color code.

In order to check the reliability of the procedure, we have performed some tests to ensure that caustics are well reconstructed. In particular, since we are interested in reconstruct caustics due to critical lines around substructures, it is fundamental to determine what is the resolution required to study the substructures we are interested in. Results of these tests are summarized in Fig. 4.3. The code is able to locate critical lines with areas of a few pixel, but the shape of the corresponding caustics obtained through the mapping onto the source plane it is not trustworthy when not many pixels are involved. We consider 50 pixel as the smallest critical line area that permits to obtain truthful caustics. The conversion between pixels and angular separation on the sky determines the minimum angular extension of critical lines which are well resolved.

Since we are interested in comparing predictions of our models with observations, it is important to understand if every caustic pinpointed by our algorithm is able to product an observable strong lensing event. In fact, a caustic too small with respect to the source extension do not produce any detectable distortion in the image; on the other hand, irrespective of caustic properties, a critical line with limited extension produces effects (an Einstein ring or multiple images) not resolvable in observations. We chose to consider as "observable" any strong lensing event for which multiple images separation (or Einstein ring diameter) is greater than $d = 1.0''$. Any critical line with effective radius (see Eq. 3.14) smaller than $d/2$ is excluded. This

[3]http://matplotlib.org/

choice automatically reject those critical lines which are too small to be mapped into realistic caustics if the map resolution is better than ≈ 0.15 arcsec/pixel.

4.2.2 Galaxy-galaxy strong lensing cross-section

As presented in the previous chapter, we are interested in understand how galaxy clusters properties affect the observed distribution of galaxy-galaxy strong lensing events, and if from these observations we can extract some constraints on the formers. A galaxy-galaxy strong lensing event happens when a background source is located on, or inside, the tangential caustic formed by a cluster member. In order to quantify the probability to have an event of this kind, we define the *galaxy-galaxy strong lensing cross-section* $\sigma_{gg}(z_s)$ as the total area enclosed by the caustics formed by substructures on the source plane at redshift z_s:

$$\sigma_{gg}(z_s) = \sum_i A_i(z_s), \tag{4.7}$$

where A_i is the area of the i-th caustic on the source plane at redshift z_s formed by a cluster member. Measuring this quantity in simulations, we can quantify the probability to have galaxy-galaxy strong lensing events in clusters with different properties.

Critical lines and caustics are represented into the code as polygons, so their area A can be calculated with the Shoelace formula (also known as Gauss area formula):

$$A = \frac{1}{2}\Big|\sum_{i=1}^{n-1} x_i y_{i+1} + x_n y_1 - \sum_{i=1}^{n-1} xi + 1 y_i - x_1 y_n\Big| \tag{4.8}$$

$$= \frac{1}{2}\Big|\sum_{i=1}^{n} x_i (y_{i+1} - y_{i-1})\Big| \tag{4.9}$$

where n is the number of the polygon's vertex. This formula is valid for any non-self-intersecting polygon, convex or concave. Its demonstration is based on the decomposition of the polygon into triangles, but can be seen also as a special case of the Green's theorem. Computation involving geometrical quantities were implemented with the aid of the PYTHON package *Shapely*[4].

4.2.3 Primary and secondary critical lines

In order to calculate the cross-section for strong lensing events around subhalos, we need to identify which caustics are due to substructures and which are due to the smooth, extended halo. In other words, we need to select only critical lines around substructures (secondary critical lines) and to exclude from the computation critical lines due to the large-scale matter distribution (primary critical lines).

If we had a single, smooth, large-scale halo, we would have a single critical line within which $\lambda_{t,halo} = 1 - \kappa_{halo} - \gamma_{halo} < 0$ and $\lambda_{t,halo} > 0$ outside. Adding a substructure to this halo, the total convergence and shear are the sum of the their respective κ and γ:

$$\kappa_{tot} = \kappa_{halo} + \kappa_{sub} \tag{4.10}$$

$$\gamma_{tot} = \gamma_{halo} + \gamma_{sub} \tag{4.11}$$

[4]http://toblerity.org/shapely/manual.html

so critical lines correspond to those points on which

$$\lambda_{t,tot} = 1 - \kappa_{tot} - \gamma_{tot} = 0. \tag{4.12}$$

Generally, if the substructure is inside the main halo's critical line where $\kappa_{halo} + \gamma_{halo} > 1$, one has $\kappa_{tot} + \gamma_{tot} > 1$. Conversely, if the substructure is outside the primary critical line, where $\kappa_{halo} + \gamma_{halo} < 1$, it can happen that due to the presence of the substructure $\kappa_{tot} + \gamma_{tot} > 1$, so it is possible the formation of a critical line where $\lambda_{t,tot} = 0$. Therefore, secondary critical lines are located only outside the primary critical line, which is the only one containing the point on which the main halo is centered. In this work, we consider as strong lenses only those substructures which forms secondary critical lines located outside the main critical line. In this way, when a secondary critical lines and the primary critical line merge, the corresponding secondary caustic (which is called "resonant" in this case) is immediately excluded from the computation of the cross-section. A source located inside a resonant caustic can be multiply imaged, giving rise to a GGSL event, but our algorithm reject these cases.

4.2.4 Substructures near the primary critical line

In particular situations, a secondary critical line inside the primary can form. For this to be possible, the contribute to the total shear of the substructure must be negative, in order to have $\kappa_{tot} + \gamma_{tot} < 1$ inside the primary critical line. This is shown in Figs. 4.4 and 4.5. Here, a $10^{12}\,\mathrm{M}_{\odot}$ SIS, indicated with a red dot, is moved on the lens plane along a straight line crossing the primary critical line due to an elliptical NFW halo of $10^{15}\,\mathrm{M}_{\odot}$. When the substructure is well inside the primary critical line (Fig. 4.4, top and middle panels), his presence do not affect much the lensing properties of the main halo and there is not the creation of an additional critical line. When the subhalo is near the position of the unperturbed critical line (bottom panel of Fig. 4.4, top panel of Fig. 4.5) a secondary critical line, internal to the primary, and the corresponding caustic arise, but they disappear when the substructure is moved away from the main halo. The primary critical line first undergoes an outstanding deformation (middle panel of Fig. 4.5) and then the substructure forms and independent secondary critical line (bottom panel of Fig. 4.5). As the subhalo moves away, its critical line shrinks. The same happens to caustics.

Even if we are especially interested in secondary critical lines and caustics, the algorithm keeps track of the area of the primary critical line of any given cluster. Thus, we are able to classify clusters depending on their Einstein radius.

The working principles of our novel algorithm are summarized in Fig. 4.6.

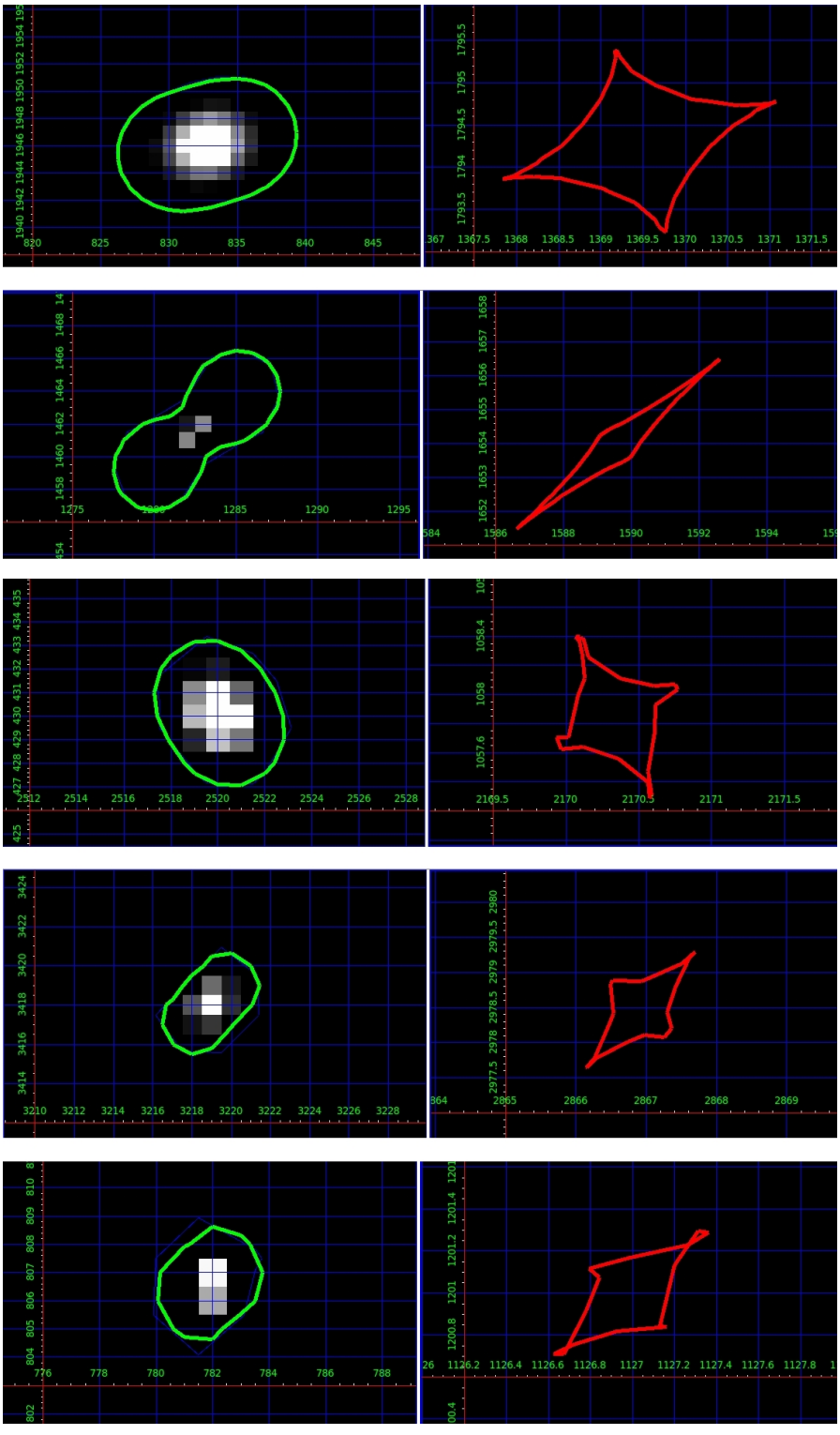

FIGURE 4.3: Caustics (right) obtained mapping on the source plane critical lines (left) with different areas. Green numbers in both figures of each panel indicate pixels. Top panel shows a critical line with area $A \sim 100$ pixel. The corresponding caustic is well resolved and its area can be accurately calculated. The same happens in the second panel with a critical line with area $A \sim 50$ pixel. At lower resolution are often obtained caustics not well resolved, with areas of a few pixel and non realistic shapes, as shown in the last three panels (where critical lines have area of approximately 25, 15 and 10 pixel respectively).

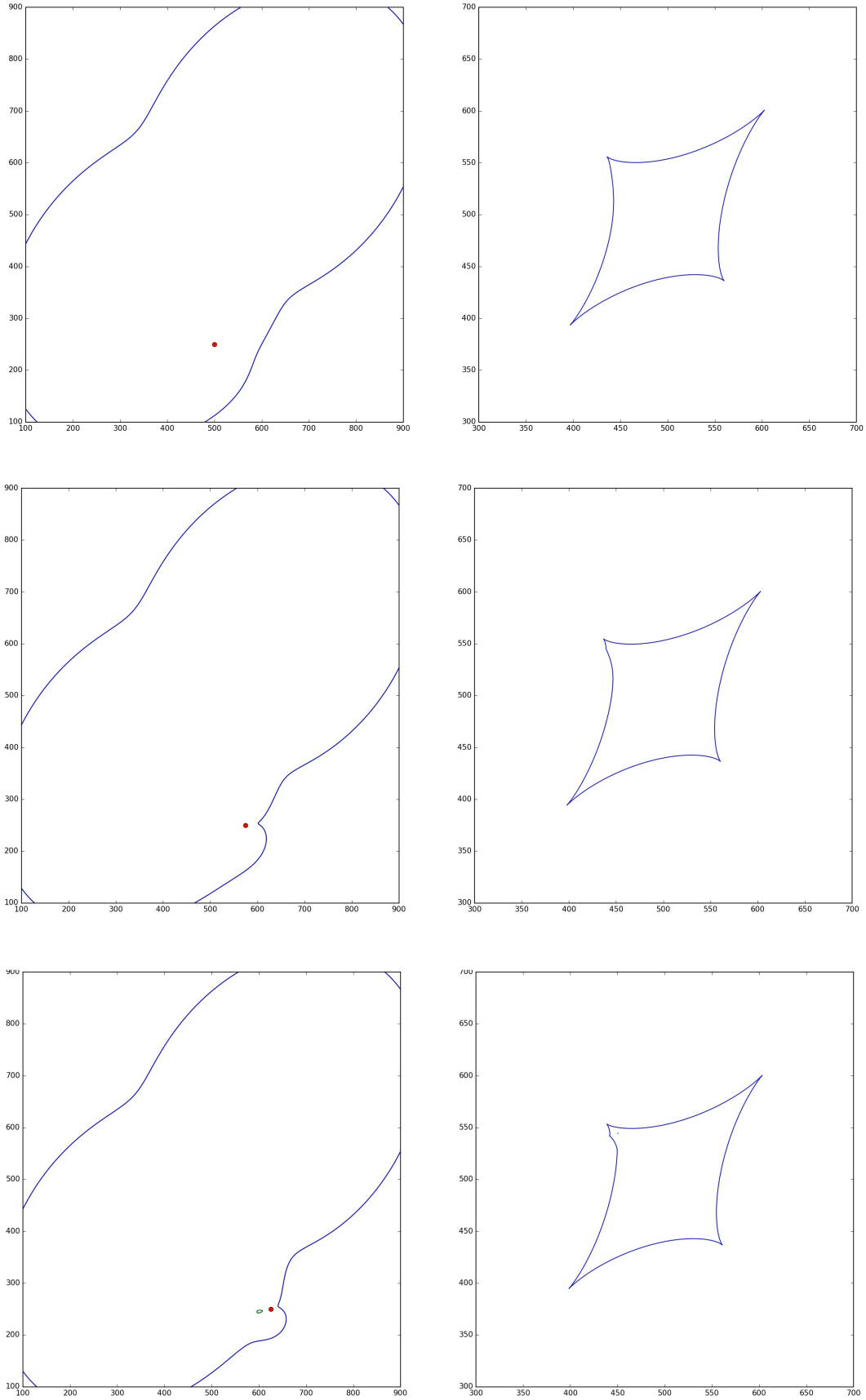

FIGURE 4.4: Evolution of critical lines (left column) and caustics (right column) moving a $10^{12}\,\mathrm{M}_{\odot}$ SIS (whose position is indicated with a red dot) with respect to an elliptical NFW halo of $10^{15} M_{\odot}$.

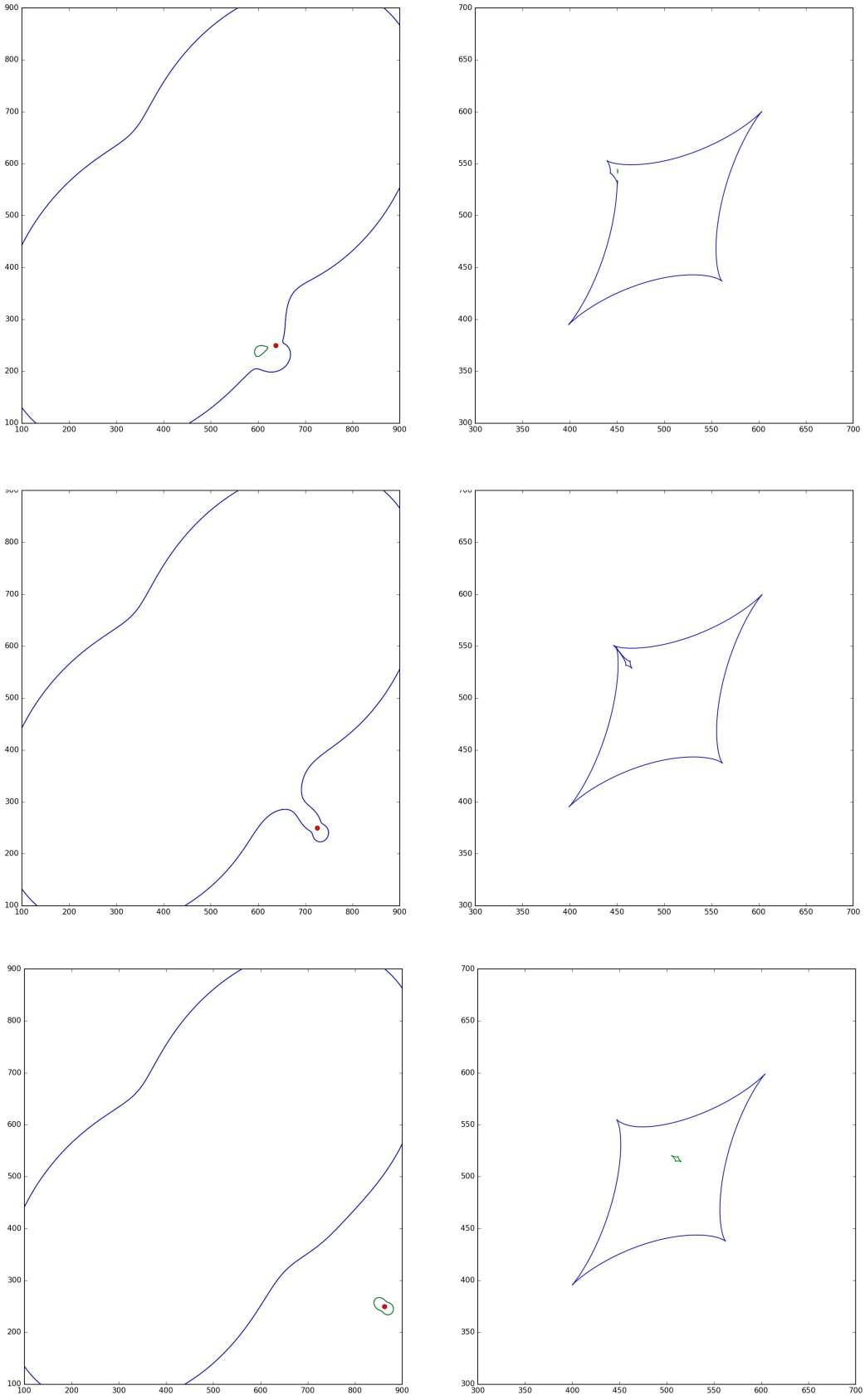

FIGURE 4.5: Evolution of critical lines (left column) and caustics (right column) moving a $10^{12}\,\mathrm{M}_{\odot}$ SIS (whose position is indicated with a red dot) with respect to an elliptical NFW halo of $10^{15} M_{\odot}$.

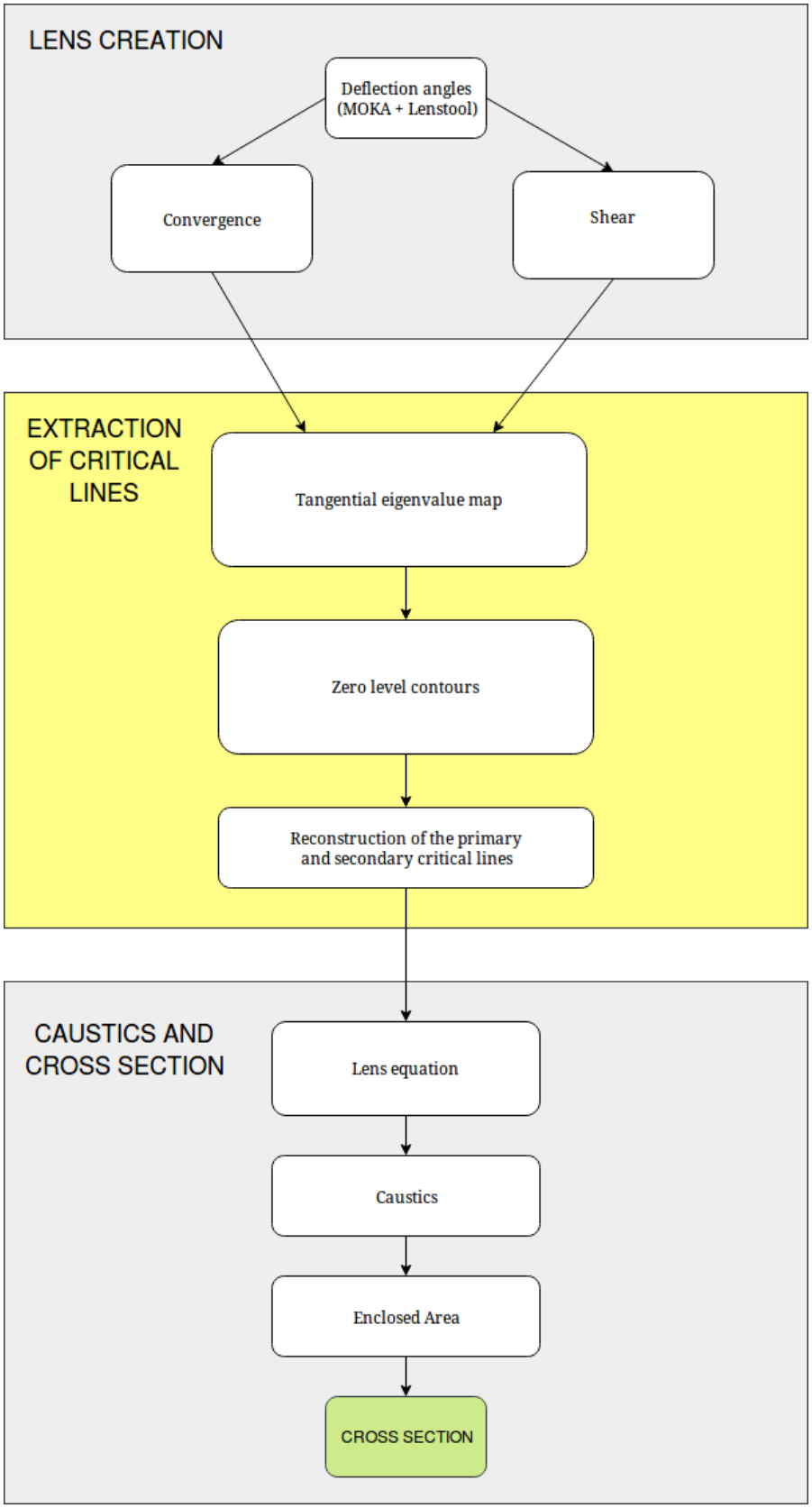

FIGURE 4.6: Flux diagram representing the various steps of our algorithm for the calculation of the galaxy-galaxy strong lensing cross-section.

Chapter 5

Results

This chapter presents the results on the galaxy-galaxy strong lensing cross-section in galaxy clusters. After introducing the cross-section, we investigate whether this quantity is sensitive to some physical property of galaxy clusters. In particular, we realize many sets of simulations varying the inner slope and the concentration of the cluster mass profile and the radial distribution and the mass function of substructures. Finally we test our findings on a real cluster, MACSJ1149, and we test the reliability of two strong lensing models of MACSJ1149 and MACSJ1206, calculating the number of expected GGSL events and comparing them with observations.

All cross-section measurements are made on lensing maps with a resolution of 0.04 arcsec/pixel, obtained simulating 160×160 arcseconds^2 fields-of-view covered with a 4000 × 4000 pixels grid. As discussed in section 4.2, this resolution is required to resolve well the critical curves with diameters of 1 arcsec, which we have taken as the lower limit for the detection of strong lensing events.

5.1 General considerations on cross-section

As presented in Eq. (4.7), we define the galaxy-galaxy strong lensing cross-section $\sigma_{gg}(z_s)$ as the area enclosed by secondary caustics on the source plane at redshift z_s. Since substructures are embedded in a complex environment, their lensing properties depend on their position in the cluster. Fig. 5.1 shows how the cross-section changes moving the same substructure with respect to the cluster main halo. Starting with a subhalo located well outside the main halo critical line, we moved the substructure on a straight line approaching the cluster center. Since the cluster mass density is a decreasing function of radius, moving the substructure towards the cluster center means moving it where the convergence is higher. As explained in Sect. 2.1.3, this cause an enlargement of the secondary critical line and thus of the corresponding caustic, entailing a growth of the cross-section. However, as exposed in Sect. 4.2.3 and 4.2.4, when the substructure enter the main halo critical line, secondary critical lines can not exist, and the cross-section drops to zero. Small secondary critical lines just inside the primary one can form if the substructure gives a negative contribution to the total shear, but the corresponding caustics are always tiny and their contribution to the cross-section is therefore negligible. For example, the area of the caustic relative to the internal critical line visible in the top-right panel of Fig.5.1 is of the order of 10^{-5} arcsec. When the subhalo exits from the primary critical line, its cross-section is again significant, and then decreases when the substructure moves away. Summarizing, for a given substructure, its contribution to the total cross-section is higher when it is located near, but outside, the primary

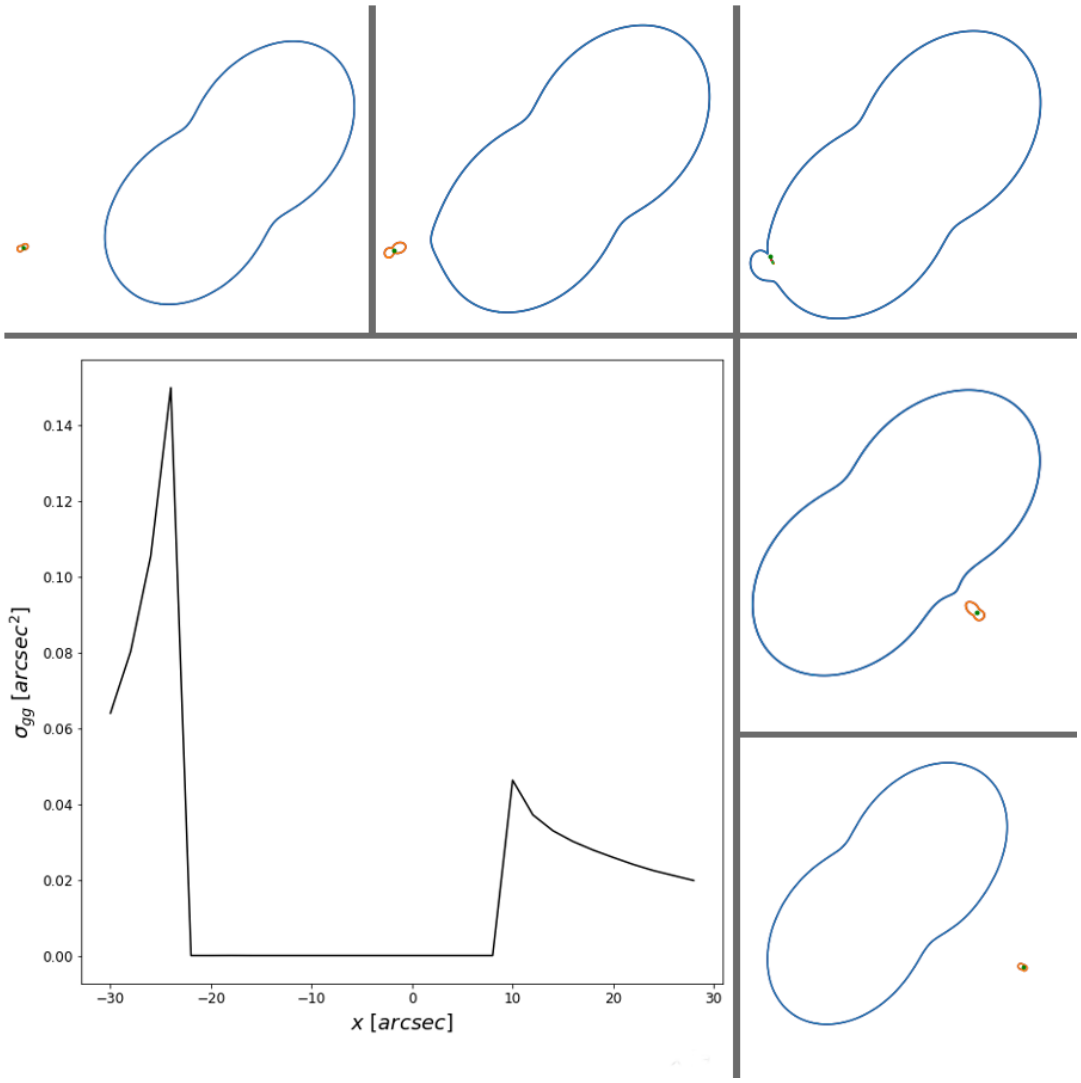

FIGURE 5.1: Dependence of the cross-section on substructure position. Small panels, clockwise from top left: critical lines configuration of a system composed by a $10^{15} M_\odot$ elliptical NFW halo positioned in the center of the field and a 10^{12} $M_\odot$ SIS substructure, whose position is indicated with a green dot. When the substructure enters the primary critical line, a small secondary critical line is formed inside the primary (third panel). Big panel: galaxy-galaxy strong lensing cross-section measured for the different substructure positions relative to the cluster center. Cross-section is higher when the substructure is near but outside the primary critical line and drops to zero when the substructure is inside. The asymmetry of the cross-section profile is due to the asymmetry of the main halo with respect to the vertical axis.

critical line. It becomes negligible as the substructure falls inside the primary critical line.

The size of critical lines grows when the source redshift z_s increase, since both convergence and shear are increasing functions of the lensing distance, whose trend is shown in Figs. 2.4 and 2.5. This fact corresponds to an increase of caustics sizes, namely a growth of the cross-section. The evolution of the total galaxy-galaxy strong

lensing cross section in galaxy clusters with respect to z_s generally follows this behaviour, but it is mitigated by the growth of the primary critical line. In fact, since it size increases with the source redshift, the region where secondary critical lines can not form expands too. That is, the contribution to the total cross-section by a particular substructure for a given source redshift $z_{s,1}$ might be erased for $z_{s,2} > z_{s,1}$. An example is given in Fig. 5.2.

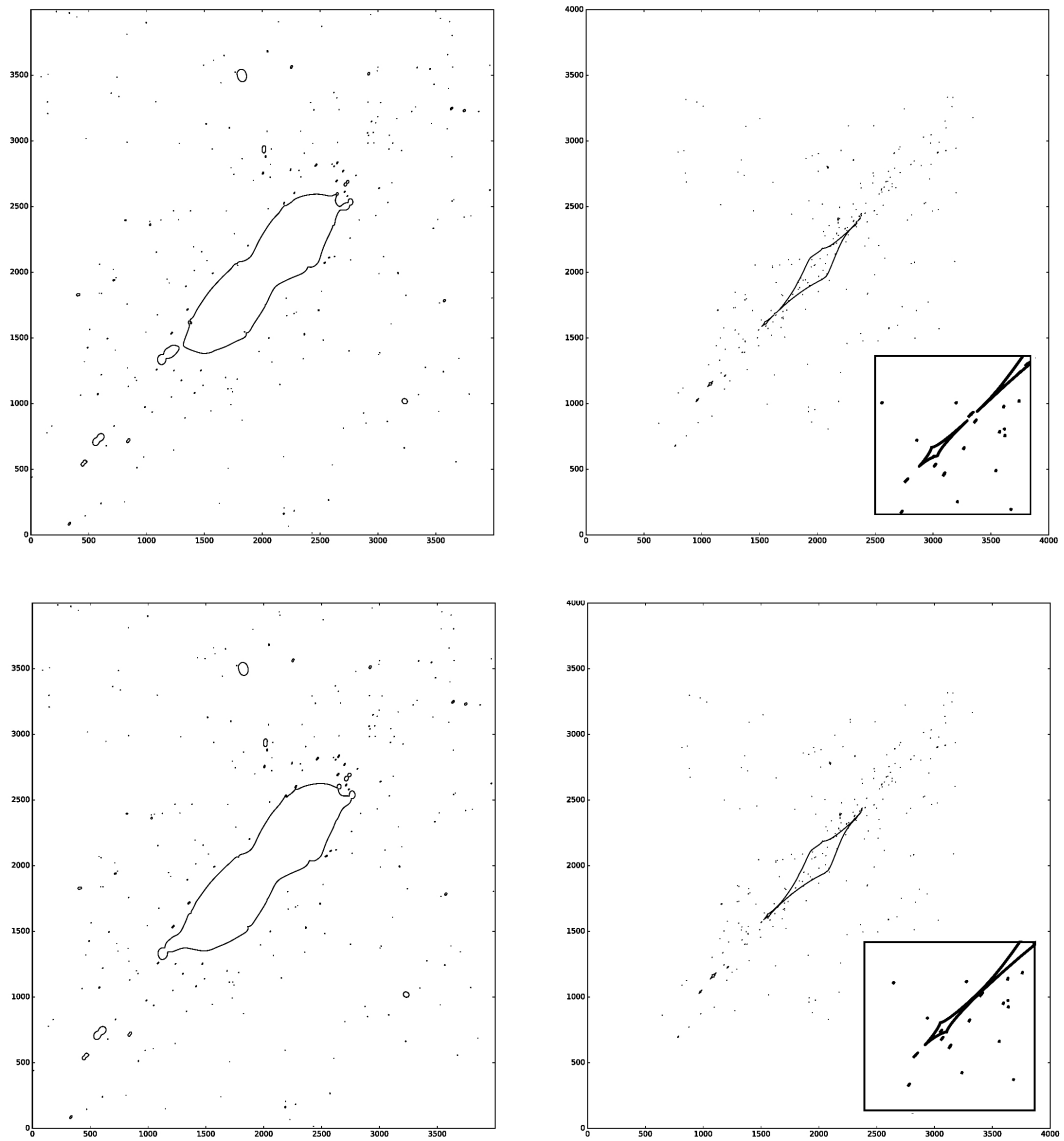

FIGURE 5.2: Critical lines and caustics for $z_s = 3$ (top panel) and $z_s = 3.5$ (bottom panel) for a simulated NFW cluster of $10^{15}h^{-1}\ M_\odot$ located at $z_L = 0.5$. The field of view is 160×160 arcsec^2. The biggest secondary critical line present when $z_s = 3$, located just outside the primary one, disappears when $z_s = 3.5$, due to the enlargement of the latter. The same happens to the corresponding caustics, which gives no more contribution to the total cross-section.

5.2 The effect of the inner slope of the mass profile

As discussed in section 3.1.3, the mean, radially-averaged density profile of galaxy clusters found in cosmological simulations can be described by the NFW profile (2.50). However, dark matter distribution of single halos can be fitted more accurately with the generalized NFW profile (2.60), in which the additional slope parameter β is introduced.

As explained in section 3.2.1, the strong lensing modeling of galaxy clusters usually allows to determine with great accuracy the position of the primary critical line, and thus to measure its Einstein radius θ_E. Assuming to know θ_E of a particular cluster, it is interesting to investigate if the slope of its gNFW profile has some effect on the probability of observing GGSL events. Fixing the Einstein radius allows to highlight the role of secondary critical lines. Moreover, in this way we can investigate if the GGSL cross-section can give us additional information useful to improve a real strong lensing model.

In order to examine this possibility, we consider 11 values of β in the range $[0.5 - 1.5]$ and we create 100 simulated clusters for each value. In order to keep θ_E fixed with varying β, we adjust the cluster virial mass, from $\approx 2.8 \times 10^{15} h^{-1} M_\odot$ for $\beta = 0.5$ to $\approx 2.8 \times 10^{14} h^{-1} M_\odot$ for $\beta = 1.5$. As reference case, we consider simulated clusters with NFW profile ($\beta = 1$) of $8 \times 10^{14} h^{-1}\ M_\odot$ and concentration $c_{vir} = 3.7$ at redshift $z_L = 0.5$ (these values satisfy the $c - M - z$ relation given in Eq. (3.11)). The mean Einstein radius is $14.86''$ for a source plane at $z_s = 3$, corresponding to ≈ 90 kpc on the lens plane, indicated by a dashed line in the left panel of Fig. 5.3. The same plot shows the family of gNFW profiles which produce the same θ_E. The right panel of the same figure illustrates how the measured GGSL cross-section varies as a function of β: the mean value is indicated as a blue, solid line, while shaded bands indicate the 68%, 95% and 100% intervals. All values are relative to a source plane at redshift $z_s = 3$.

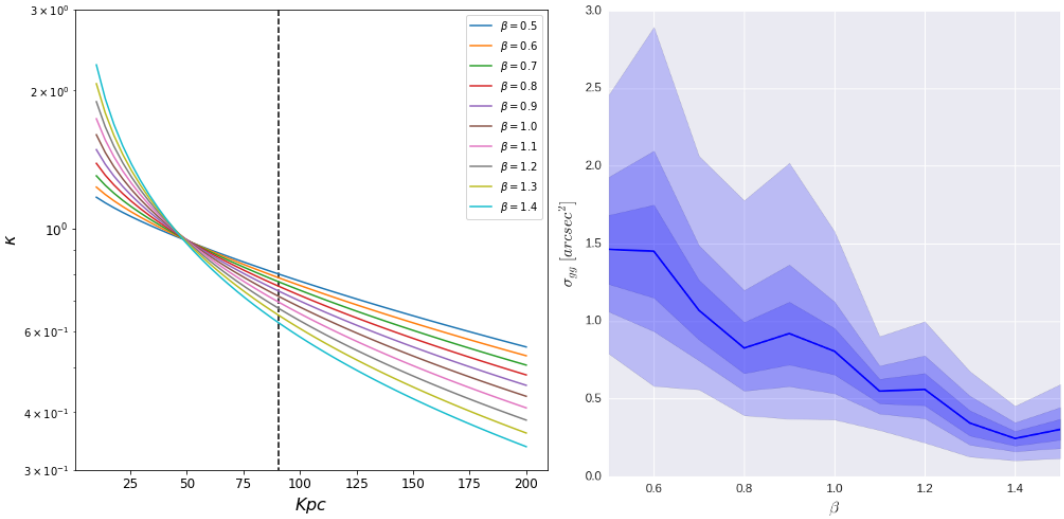

FIGURE 5.3: Left: convergence profiles of gNFW clusters with different values of the slope parameter β but with the same Einsten radius, indicated by the vertical dashed line. Right: measured GGSL cross-section as a function of the slope β of the gNFW profile. The solid line indicates the mean value, shaded bands indicates the 68%, 95%, 100% intervals. All values are relative to a source plane at redshift $z_s = 3$.

The measured cross-section increase with decreasing β, tripling its mean value from $\beta = 1.5$ to $\beta = 0.5$. In other words, at fixed Einstein radius, clusters with a shallower profile produce more GGSL events. In fact, as can be seen in Fig. 5.3, outside the Einstein radius, where the GGSL signal forms, the convergence is higher for shallower profiles. This means that at fixed distance from the cluster centre, substructures are located in a denser environment and thus are able to produce larger and more abundant critical lines and caustics. Moreover, in order to keep θ_E fixed, clusters with a shallower profile have a larger total mass. That is, they host on average more substructures, and a larger fraction of the total cluster mass is stored in subhalos (see Sect. 3.1.5).

5.3 The effect of the halo concentration

The shape of the NFW profile depends also on the concentration parameter $c_{vir} = R_{vir}/R_s$. Analogously to the procedure previously described, we produced several realizations of simulated clusters with varying concentration and total mass, while preserving the extension of the primary critical line. Again, the reference clusters has mass of $8 \times 10^{14} h^{-1}\ M_\odot$ and concentration $c_{vir} = 3.7$ at redshift $z_L = 0.5$. The left panel of Fig. 5.4 shows the convergence profiles in the different cases (solid lines) and the mean Einstein radius for $z_s = 3$ (dashed line). The right panel displays the measured cross-section as a function of c_{vir}: the shaded bands indicates the 68%, 95% and 100% intervals, while the solid line represent the mean value. We vary the concentration in the range $c_{vir} = [3.05 - 4.65]$ and, to keep θ_E constant, the mass M_{vir} in the range $[1 \times 10^{15} - 6.5 \times 10^{14}]\ h^{-1} M_\odot$.

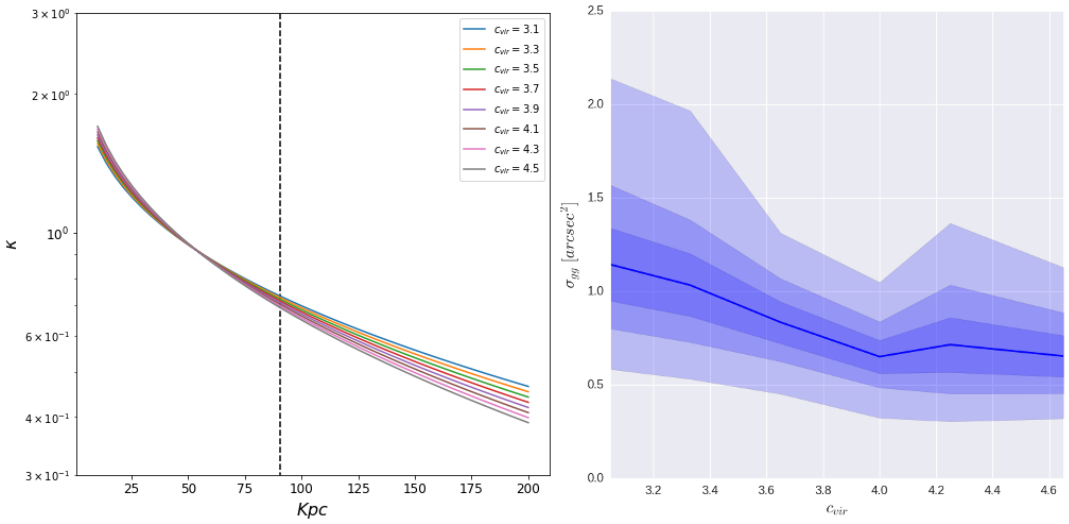

FIGURE 5.4: Left: convergence profiles of NFW clusters with different concentration c_{vir} but with the same Einsten radius, indicated by the vertical dashed line. Right: measured GGSL cross-section as a function of the concentration c_{vir} of the NFW profile. The solid line indicates the mean value, shaded bands indicates the 68%, 95%, 100% intervals. All values are relative to a source plane at redshift $z_s = 3.0$.

As we can see, in the range of halo concentrations we considered, c_{vir} do not affect substantially the convergence profiles near the Einstein radius. The consequence of this fact is that secondary critical lines and caustic are not particularly

affected by the main halo concentration, thus the GGSL cross-section varies only by $\approx 30\%$. Contrary to the inner slope, the concentration of the cluster profile can not be considered a quantity able to strongly affect the abundance of GGSL events.

5.4 The effect of the substructures mass function

As exposed in section 3.1.5, the subhalo mass function (SHMF) measured from numerical simulation of structures formation has the form of a power law at low masses with an exponential cut-off at high masses. MOKA implements the SHMF (3.12) derived by Giocoli et al., 2010, which we report here:

$$\frac{1}{M_{vir}}\frac{dN(M_{vir}, c_{vir}, z_l)}{dm} = A(1+z_l)^{1/2}\frac{c^*}{c_{vir}}m^{\alpha}exp\left[-\tilde{\beta}\left(\frac{m}{M_{vir}}\right)^3\right]. \tag{5.1}$$

$A = 9.33 \cdot 10^{-4}$ is a normalization factor, $\tilde{\beta} = 12.2715$ controls the exponential cut-off and $\alpha = -0.9$ is the power-law index. c^* is the mean concentration of a halo with mass M_{vir} at redshift z_l. The mass fraction in substructures f is given by

$$f = \frac{M_{subs}}{M_{vir}} = \frac{1}{M_{vir}}\int_{m_{min}}^{M_{vir}} dm \frac{dN}{dm} m. \tag{5.2}$$

Aiming at studying the influence of the SHMF on the GGSL cross-section, we produce two kinds of simulations. In the first simulations set we study the effect of massive subhalos on the total GGSL signal by varying A and $\tilde{\beta}$ keeping constant the mass fraction in substructures f. On the other hand, in the second one we vary the values of α and A keeping f fixed. In this way, one can study the effect of small substructures. Simulations consist of 100 clusters for each value of α and $\tilde{\beta}$ considered. The clusters have a mass $M_{vir} = 10^{15} h^{-1}\, M_{\odot}$, a concentration $c_{vir} = 3.5$, a minimum subhalo mass of $10^{10} h^{-1}\, M_{\odot}$ and a redshift $z_L = 0.5$. The resulting mass fraction in subhalos is 0.168.

Fig. 5.5 shows the different SHMF obtained varying $\tilde{\beta}$ and the resulting cross-section, whose mean value (solid line) drops monotonically with increasing $\tilde{\beta}$, halving from $\tilde{\beta} = 10$ to $\tilde{\beta} = 10^8$. The effect is particularly evident for $\tilde{\beta} > 10^4$, when the high-mass tail of the SHMF starts to deviate significantly from the standard case. This confirms our suspects: massive substructures are the main contributors to the GGSL cross-section, and their absence drastically diminish the chances of observing strong lensing events by cluster substructures. On the contrary, Fig. 5.6 shows that the GGSL cross-section is not particularly sensitive to the low-mass end of the SHMF: even if we increase the number of small substructures, due to their low mass they have not a significant impact on the probability of GGSL events. The cross-section is fairly constant in the range $0.2 < \alpha < 0.7$, and drops by a factor ≈ 2 only for $0.7 < \alpha < 1.0$ when, in order to preserve f, the abundance of subhalos with low mass cause the suppression of massive substructures.

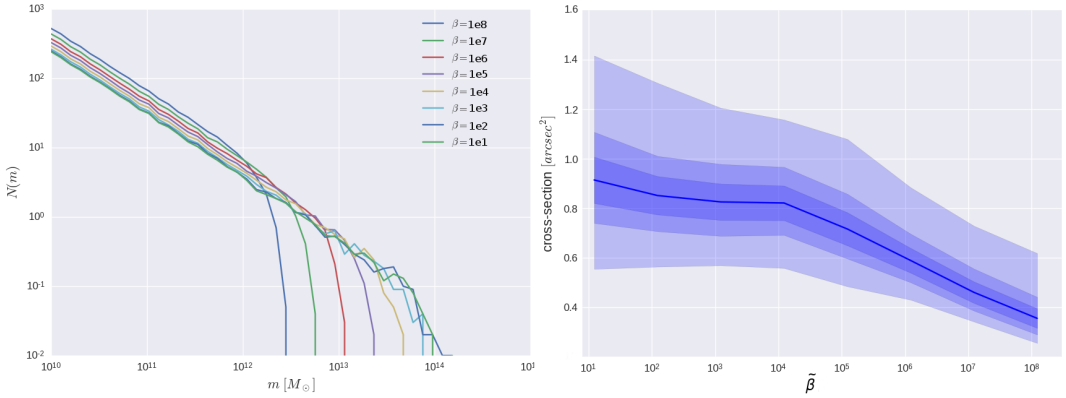

FIGURE 5.5: Left: subhalo mass function (5.1) for different values of the cutoff parameter $\tilde{\beta}$. The graph displays the mean number of substructures in 100 MOKA simulations in each mass bin. Right: measured GGSL cross-section as a function of $\tilde{\beta}$. The solid line indicates the mean value, shaded bands indicates the 68%, 95%, 100% intervals. All values are relative to a source plane at redshift $z_s = 3.0$.

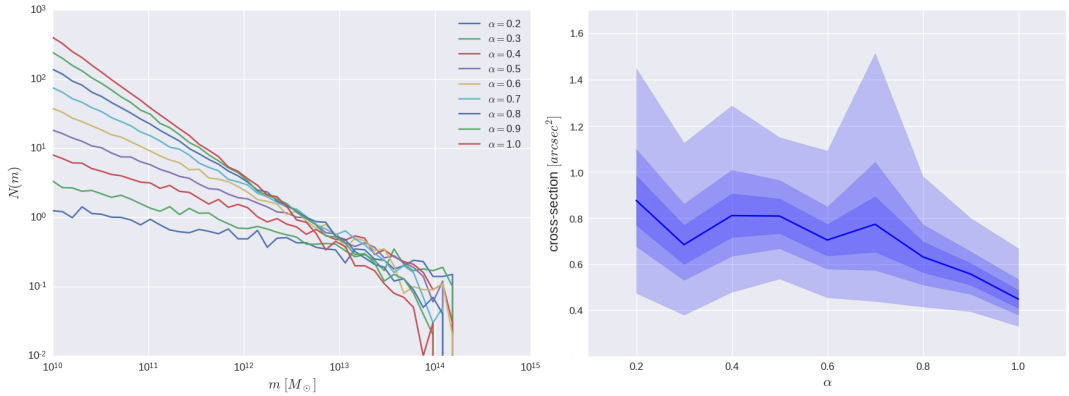

FIGURE 5.6: Left: subhalo mass function (5.1) for different values of the power-law index α. The graph displays the mean number of substructures in 100 MOKA simulations in each mass bin. Right: measured GGSL cross-section as a function of α. The solid line indicates the mean value, shaded bands indicates the 68%, 95%, 100% intervals. All values are relative to a source plane at redshift $z_s = 3.0$.

5.5 The effect of the substructure radial distribution function

The last property we consider is the radial distribution of subhalos inside the cluster. Galaxy clusters found in cosmological simulations exhibit a radial distribution function of substructures described by Eq. (3.13), which we report here:

$$\frac{n(< d)}{N_{tot}} = \frac{(1 + ac_{vir})d^b}{(1 + ac_{vir}d^2)}. \tag{5.3}$$

d is the distance to the host halo centre in units of the virial radius, N_{tot} is the total number of subhalos in the host, $a = 0.244$ and $b = 2.75$. In order to study the impact of the substructure radial distribution on GGSL cross-section, we have constructed many realizations of simulated clusters with different values of the parameter b. Fig.

5.7 shows the resulting cumulative subhalo radial distributions: diminishing b substructures are moved from the outskirts toward the cluster center.

From the right panel of the same figure, it is evident that the mean GGSL cross-section (solid line) has a significant dependence on b: in clusters with more centrally distributed subhalos it is more likely to observe strong lensing events by cluster members. The mean cross section increases by a factor ≈ 5 from $\beta = 1.55$ to $\beta = 2.75$ This fact has a trivial explanation: since the region from which the majority of the strong lensing signal forms is near the cluster primary critical line, a higher concentration of substructures in this region increases the signal itself.

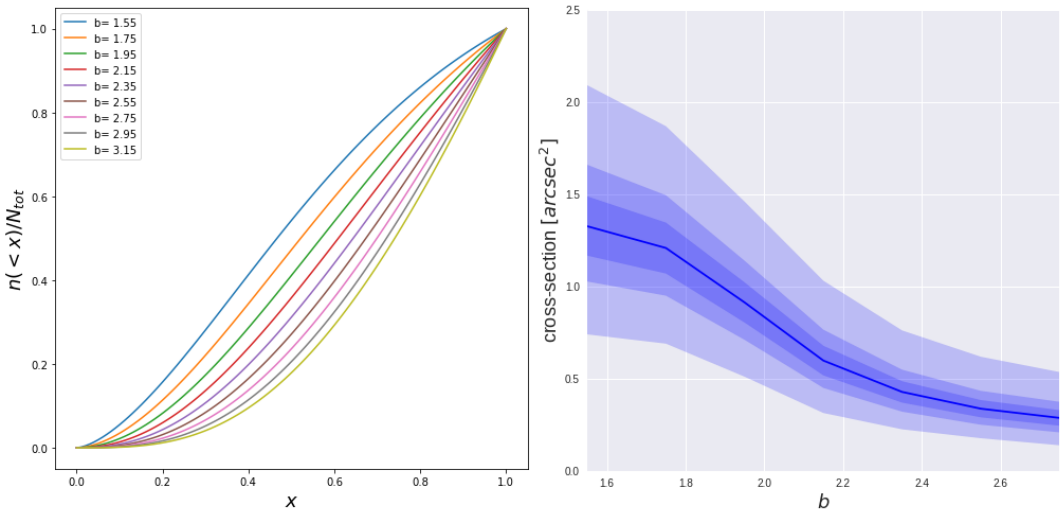

FIGURE 5.7: Left: cumulative radial distribution of substructures for different values of the parameter b of Eq. 5.3. Radial distances x are measured in unit of the virial radius of the cluster. Right: measured GGSL cross-section as a function of b. The solid line indicates the mean value, shaded bands indicates the 68%, 95%, 100% intervals. Values are relative to a source plane at redshift $z_s = 3.0$.

5.6 Application to a real cluster: MACS1149

As discussed in the previous sections, the GGSL cross-section is particularly sensitive to the subhalo radial distribution, to subhalo mass function and to the inner slope of the cluster mass profile. Here we consider a real cluster: MACSJ1149.

5.6.1 Previous works on MACSJ1149

The galaxy cluster MACSJ1149 has celestial coordinates 11:49:36.3, +22:23:58.1 (R.A., Dec.) and at redshift z=0.544. During the past years it was observed in the framework of several cluster surveys, in many bands. Thanks to its X-ray luminosity, it was discovered by the MAssive Cluster Survey (MACS, Ebeling, Edge, and Henry, 2001). Subsequently, more recent observations in the same band revealed the presence of at least four merging DM halos (Ogrean et al., 2016). Its complex morphology

has been studied in more details thanks to optical images and spectroscopic observations taken with the Hubble Space Telescope (HST) as part of the Grism Lens-Amplified Survey from Space (GLASS, Treu et al., 2015), Cluster Lensing And Supernova survey with Hubble (CLASH, Postman et al., 2012) and Hubble Frontier Field initiative (HFF, Lotz et al., 2016). Spectroscopy of many sources is available also from the Multi-Unit Spectroscopic Explorer (MUSE) instrument on the Very Large Telescope (VLT) and from observations with the DEep Imaging Multi-Object Spectrograph (DEIMOS) on the Keck-II Telescope.

During November 2014, thanks to GLASS observations, it was discovered in this cluster the first multiply imaged Supernova (SN) (Kelly et al., 2015), nicknamed "SN Refsdal". SN Refsdal appears as an Einstein Cross around an elliptical cluster member, and it's hosted in an arm of a background spiral galaxy at redshift 1.489 that is multiply imaged by the cluster potential. Due to time delays between different images, the SN Refsdal reappeared approximately one year later in one of the other two images of the spiral galaxy. In the last image the SN was visible some decades ago. Accurate analysis of HST images revealed also the presence of 108 multiple images from 36 sources.

Thanks to the abundance of constraints (cluster member positions and velocity dispersion, multiple image positions, time delays) MACSJ1149 was used as a testbed for comparing different gravitational lensing modeling strategies, as described in Treu et al., 2016. Many groups have attempted to reproduce the lensing peculiarity of this cluster, using different optimization softwares and different hypothesis in describing its mass distribution. In this work, we have taken as reference model the one proposed in Kawamata et al., 2016. This lensing model was built using the software GLAFIC (Oguri, 2010) with a parametric approach (see Sect. 3.2.1). Cluster members were selected using photometric redshifts available from HST data and through the study of the cluster red sequence, and modeled as pseudo-Jaffe ellipsoids (PJE, Keeton, 2001) with null core radius, a profile almost identical to the truncated SIE. In order to reduce the number of free parameters, substructure velocity dispersions σ_i and truncation radii $r_{t,i}$ were computed using scaling relations linking these quantities to the measured luminosities L_i. In particular, they are given by:

$$\sigma_i = \sigma_* L_i^{1/4} \tag{5.4a}$$

$$r_{t,i} = r_{t,*} L_i^{\eta} \tag{5.4b}$$

where σ_*, $r_{t,*}$ and η are the parameters to optimize. The elliptical galaxy responsible for the splitting of the images of the Supernova Refsdal was modeled independently. Its free parameters are the velocity dispersion and the truncation radius of the profile. The ellipticity and position angle of each galaxy are derived from the HST images and fixed. The total number of cluster member considered in the modeling is 171. The main dark matter halos were modeled with elliptical NFW profiles, with M_{vir}, position, ellipticity $e = 1 - a/b$, position angle θ_e and concentration c_{vir} as free parameters. These NFW components were placed at the positions of brightest cluster galaxies. The best fitting model predicts four main halos. The model includes also an external shear and an internal multipole perturbation to the potential, describing an asymmetry of the latter. Best fitting model parameters relevant for this discussion are summarized in Table 5.1.

The model constraints consist of positions of multiple images of background sources with known spectroscopic redshifts, positions of knots in the lensed galaxy that hosts the SN Refsdal, and positions of the supernova images. Model predictions

Component	Model	Mass ($10^{14}h^{-1}M\odot$)	e	θ_e (deg)	c_{vir}	Δx (arcsec)	Δy (arcsec)
Main halo 1	NFW	8.26	0.49	126.37	3.82	-0.21	-0.12
Main halo 2	NFW	1.61	0.67	76.36	6.66	[16.38]	[47.36]
Main halo 3	NFW	0.64	0.70	158.13	2.57	-22.93	-32.21
Main halo 4	NFW	0.16	0.68	150.23	[10.00]	[-44.77]	[-54.86]
		σ_* (km s^{-1})	$r_{t,*}$ (arcsec)	η			
Subshalos	PJE	233.07	2.88	0.26			
		σ (km s^{-1})	e	θ_e (deg)	r_t (arcsec)	Δ_x (arcsec)	Δ_y (arcsec)
Galaxy	PJE	232.08	[0.30]	[47.50]	1.26	[3.22]	[-11.11]

TABLE 5.1: Best fit parameters for the lensing model of MACSJ1149 by Kawamata et al., 2016. Coordinates are relative to the cluster BCG. Numbers in square brackets were fixed during the model optimization. For uncertainties on the best fit parameters, see Kawamata et al., 2016.

on positions and time delays of the reappearence of SN Refsdal are fully consistent with the observed values. We take the cross-section of this model as reference.

MACSJ1149 is one of the 20 clusters considered in the thorough analysis by Umetsu et al., 2016. In this work, strong lensing, weak lensing (shear and magnification data) obtained with HST during the CLASH survey and with the wide-field Suprime-Cam on the Subaru Telescope are used to derive the total cluster mass profile to $\approx 1000''$ (Fig. 5.9). Fitting an NFW model, the cluster has a virial mass $M_{vir} = 25.02 \pm 5.53 \times 10^{14} M_\odot$ and a concentration $c_{vir} = 2.1 \pm 0.6$ (reported as M_{200c} and c_{200c} by Umetsu et al., 2016).

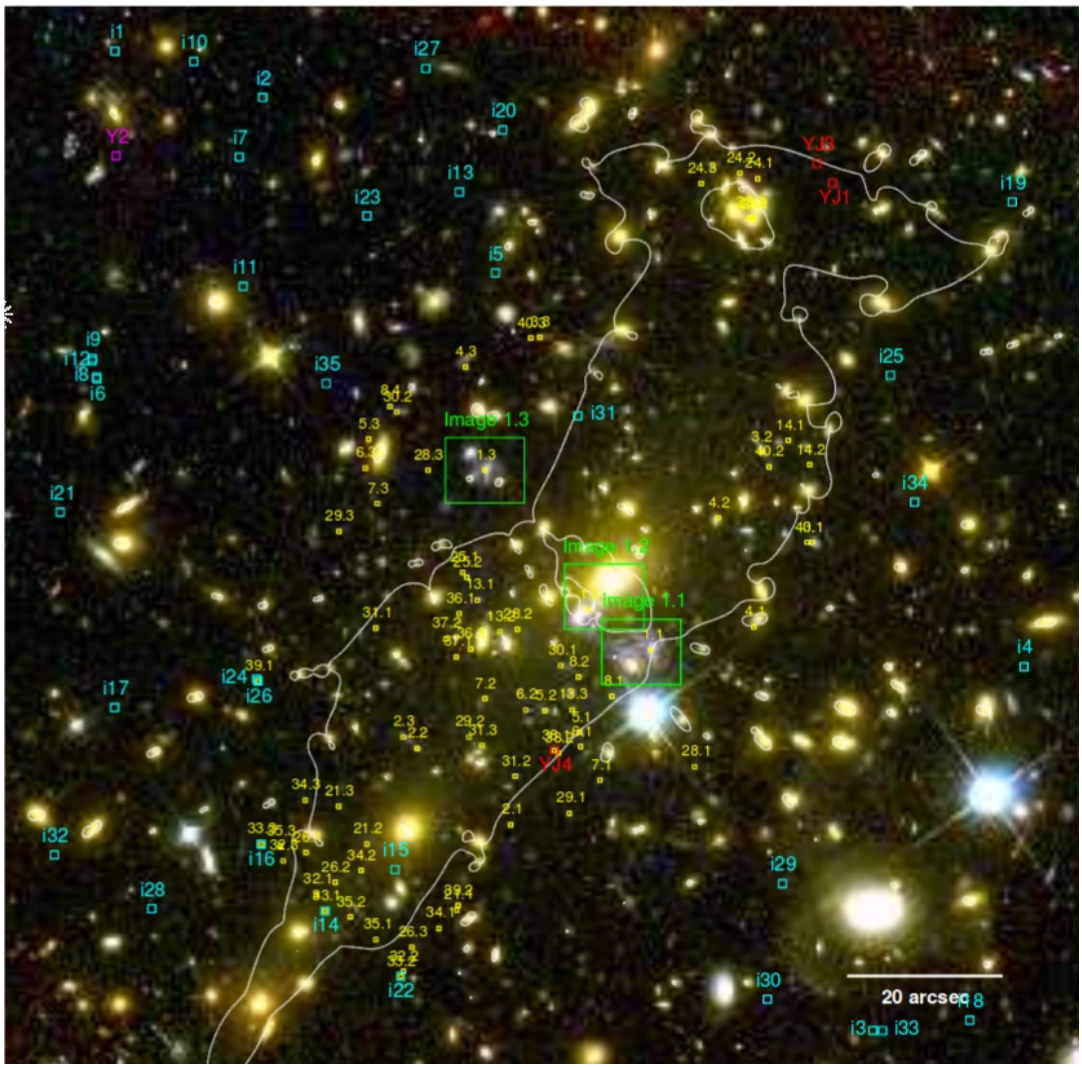

FIGURE 5.8: Multiple images systems used for mass modeling (yellow squares) and radial and tangential critical curves for a source at z=8.0 for the best fitting model of MACSJ1149 by Kawamata et al., 2016.

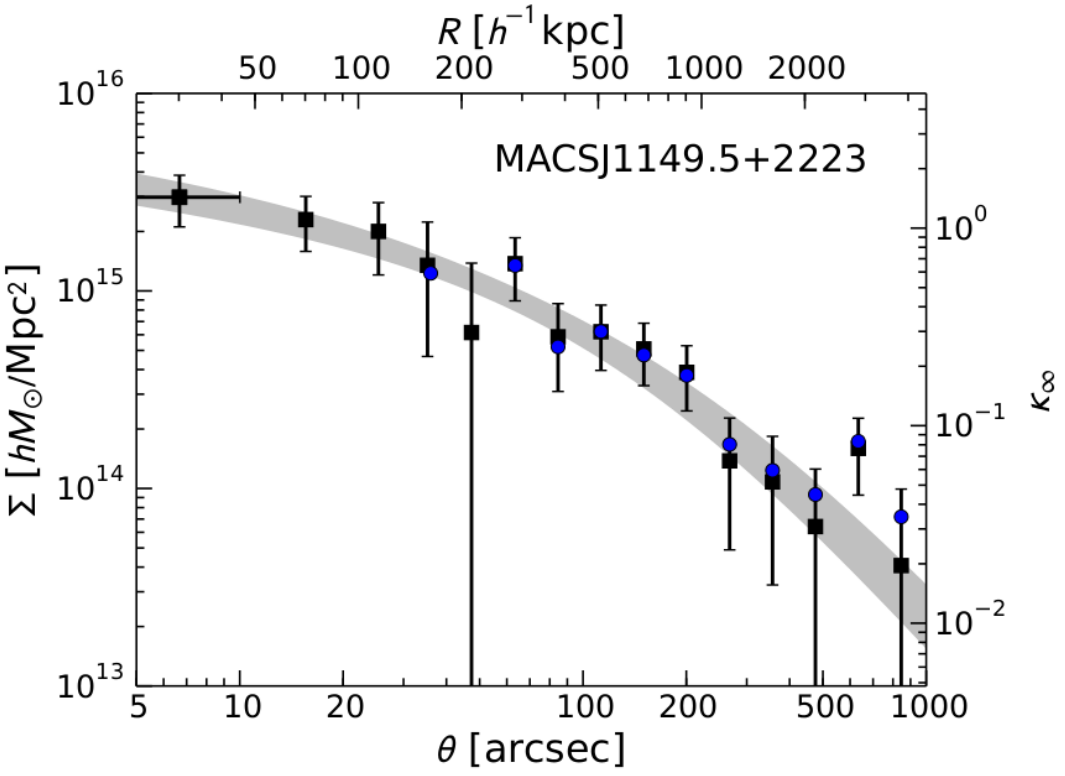

FIGURE 5.9: Surface mass density profile of MACSJ1149 derived by Umetsu et al., 2016 from a joint analysis of HST strong/weak-shear lensing and ground-based weak shear/magnification lensing data (black squares). Error bars represent the 1σ uncertainty. The gray area shows the best-fit NFW profile (1σ uncertainty).

5.6.2 Full constrained simulations of MACSJ1149

In order to study the effect of different cluster properties on the cross-section, we have carried out three sets of 100 simulations each. In the first one, which we refer to as "full constrained" set, the large-scale distribution of matter (the four main halos) and the positions of the 171 substructures are fixed to the values of the reference model. However, subhalo masses are generated according to the theoretical SHMF in the ΛCDM cosmology. We generate 171 subhalos, we order them in mass, and we place them at the observed locations of the cluster galaxies in MACSJ1149. While doing this, we make sure that the most massive subhalos correspond to the brightest galaxies. Thus, we build many realizations of simulated clusters with the same properties of MACSJ1149, except for the SHMF. A difference between observed and theoretical SHMFs could entail a mismatch between measured cross-sections in the two cases.

The left panel of Fig. (5.10) shows the distributions of observed (blue) and simulated (magenta) substructures velocity dispersion distributions. Shaded band indicates 68%,95% and 100% intervals. The model has an excess of substructures with central velocity dispersion of about 150 km/s. In some simulations, we find substructures with masses higher than observed. The right panel of the same figure shows a comparison between the convergence profiles and the Einstein radius of model (red) and simulations (blue). Simulations show an excess of convergence in the inner $10''$. However, this region is well inside the Einstein radius, thus it has not

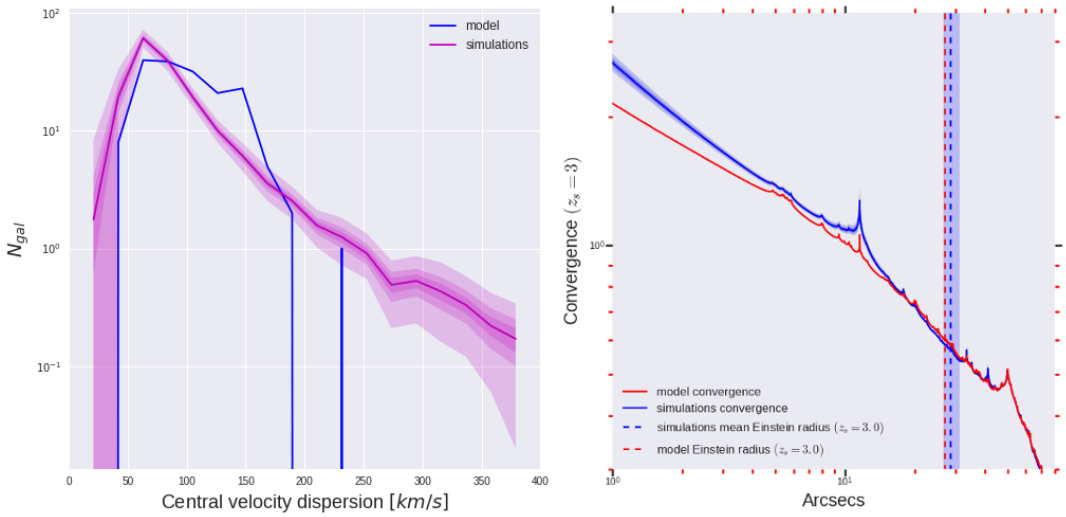

FIGURE 5.10: Left: Comparison between the substructures velocity dispersions distribution of the reference model of MACSJ1149 (blue solid line) and of the full constrained simulations (magenta, solid line: mean values; shaded magenta bands: 68%,95% and 100% intervals). Right: comparison between the convergence radial profile of the reference model of MACSJ1149 (red solid line) and of the full constrained simulations (blue, solid line: mean profile; shaded blue bands: 68%,95% and 100% intervals). Vertical, red, dashed line indicates the circularized Einstein radius of the model, calculated as $R_E = \sqrt{S/\pi}$, where S is the area of the primary critical line. The vertical, blue, dashed line and the vertical blue band indicate respectively the mean value and the full interval covered by the same quantity in simulations.

influence on the cross-section. In the region relevant for our analysis, simulations convergence profiles are compatible with those of the model.

The GGSL cross-section of the reference model and of simulations are shown in Fig. 5.12. Despite the differences between the SHMFs in the two cases, the measured cross-section are compatible in the source redshift range $[1.0-8.0]$. Both simulations and model exhibit a drop in the cross-section between $z_s = 2.0$ and $z_s = 3.0$. This is due to the effect described in Sect. 5.1 and it is caused by the relative positions of main halos and massive substructures, identical in the two cases. The effect on critical lines is shown in Fig. 5.11.

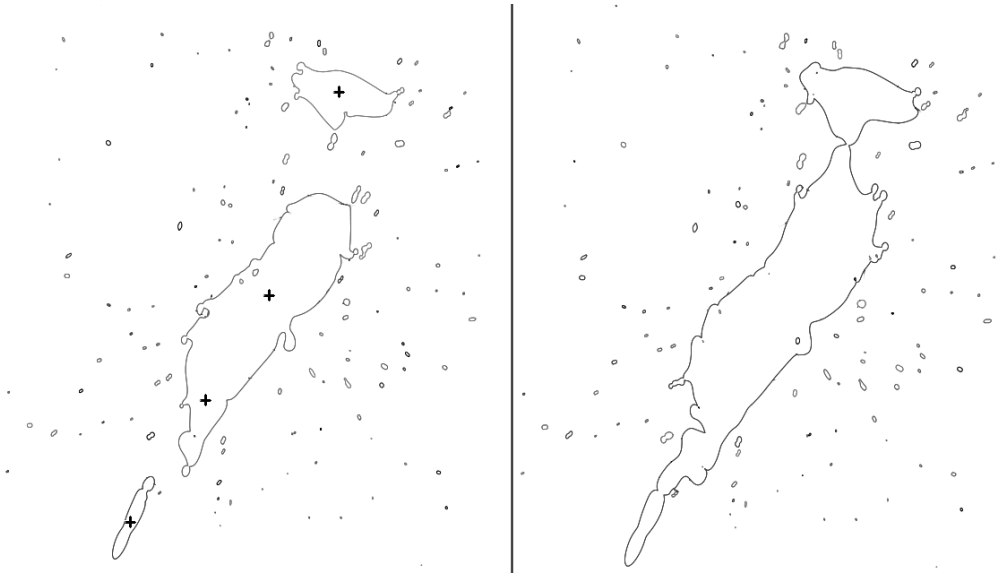

FIGURE 5.11: Critical lines of the reference model of MACSJ1149 for $z_s = 2.2$ (left) and $z_s = 3.0$ (right). Black crosses in the left panel show the position of the centers of the four main halos. Increasing source redshift, the primary critical lines (those which contain the centers of the four main halos) expand and merge, causing the disappearance of secondary critical lines and of their corresponding caustics, causing a decrease of the cross-section.

5.6.3 Constrained simulations of MACSJ1149

In the second set of simulations we populate the cluster with subhalos that not only follow the SHMF in ΛCDM cosmology, but also reproduce their radial distribution. The differences in the measured cross-section between this simulation set and the previous one are due to the substructures radial distribution only. We call these simulations "constrained".

The cumulative radial distribution of model and simulations are displayed in Fig. (5.13). Inside the considered radius of 80 arcsec (about 500 Kpc at $z = 0.544$), simulated clusters (magenta band) have always less subhalos with respect to observations (blue curve): ≈ 130 substructures against the 171 observed cluster members. This fact is in agreement with findings of Natarajan et al., 2017 (see Fig. 1.7, upper right panel). Consistently with results of section 5.5, the lack of substructures in simulations makes their cross section always substantially lower with respect to the model (Fig. 5.14). The cross-section of the reference model (blue curve) is ≈ 4 times higher than the mean cross-section of simulated clusters (magenta curve). Moreover,

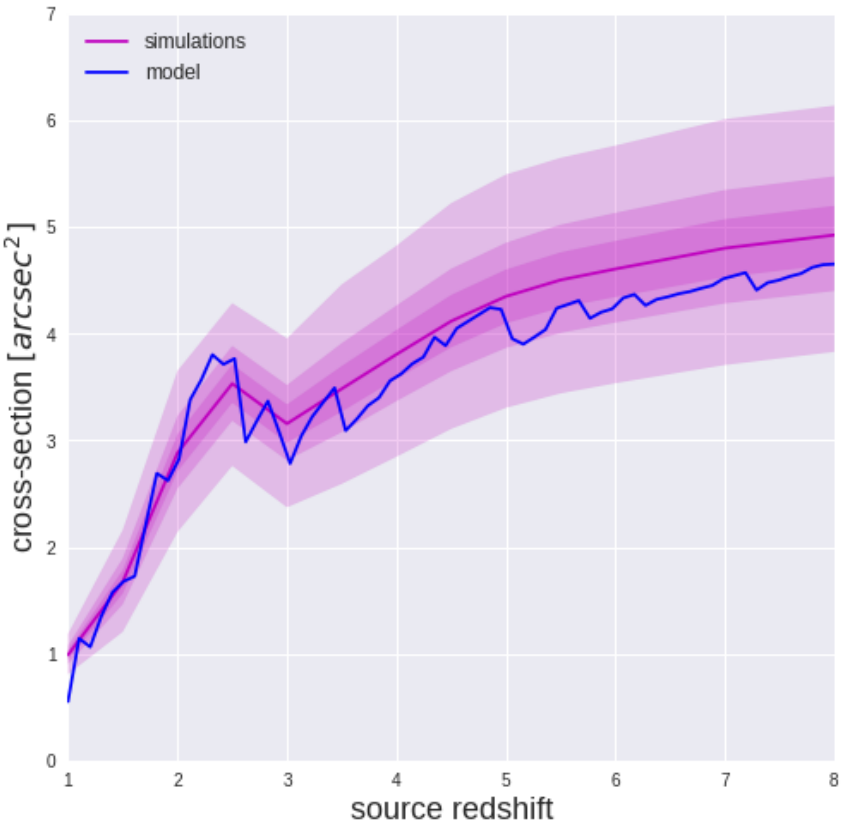

FIGURE 5.12: Measured galaxy-galaxy strong lensing cross-section of the reference model of MACSJ1149 (blue line) and of full constrained simulations (magenta). Bands of different hues indicates the 68%, 95% and 100% intervals. The dark magenta line is the mean value of the measured cross section in simulations.

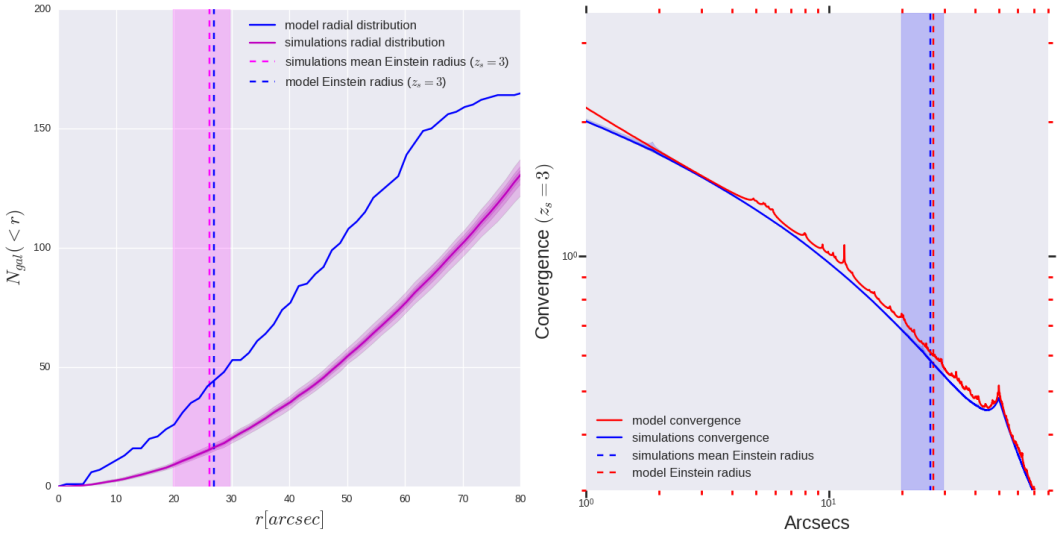

FIGURE 5.13: *Left*: comparison between the cumulative radial distribution of substructures in the reference model of MACSJ1149 (blue solid line) and in constrained simulations (magenta, solid line: mean value; shaded blue bands: 68%,95% and 100% intervals). Vertical, blue, dashed line indicates the circularized Einstein radius of the model, calculated as $R_E = \sqrt{S/\pi}$, where S is the area of the primary critical line. The vertical, magenta, dashed line and the vertical magenta band indicate respectively the mean value and the full interval covered by the same quantity in simulations. *Right*: Comparison between the convergence radial profile of the reference model of MACSJ1149 (red solid line) and of the constrained simulations (blue, solid line: mean profile; shaded blue bands: 68%,95% and 100% intervals). Vertical, red, dashed line indicates the circularized Einstein radius of the model, while the vertical, blue, dashed line and the vertical blue band indicate respectively the mean value and the full interval covered by the same quantity in simulations.

the model cross-section is always ≈ 2 times higher than the maximum cross-section found in simulations (pale magenta band).

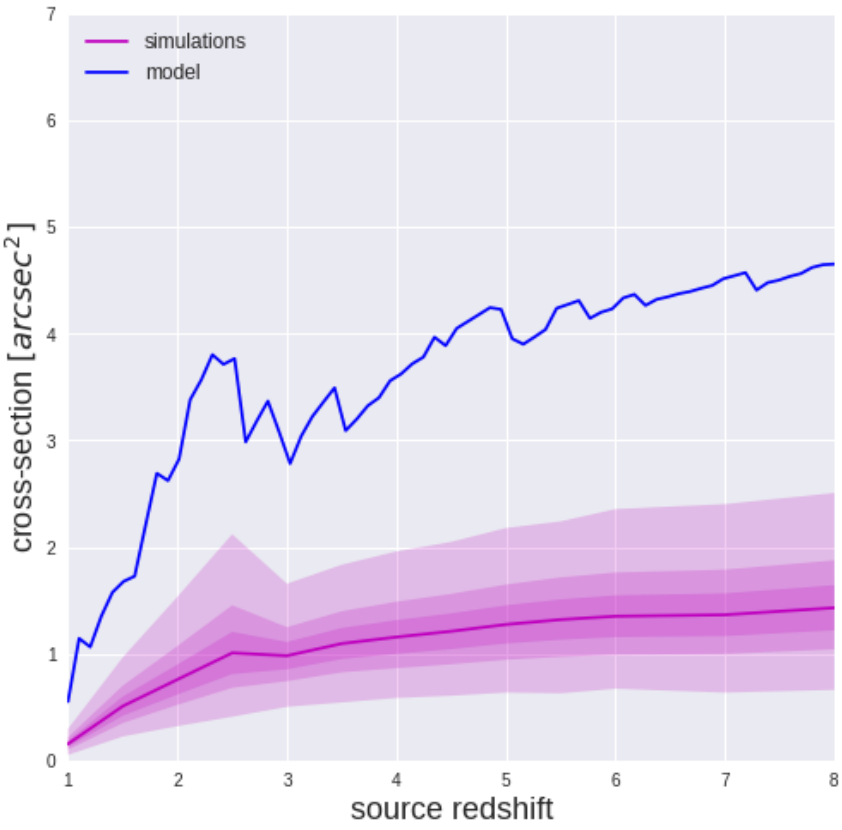

FIGURE 5.14: Measured galaxy-galaxy strong lensing cross-section of the reference model of MACSJ1149 (blue line) and of constrained simulations (magenta). Bands of different hues indicates the 68%, 95% and 100% intervals. The dark magenta line is the mean value of the measured cross section in simulations.

5.6.4 Unconstrained simulations of MACSJ1149

In the third simulations set, which we call "unconstrained", we have replaced the four main NFW halos of the model with a single, spherical NFW halo with virial mass and concentration as measured by Umetsu et al., 2016 (see section 5.6.1). Substructures are treated as in constrained simulations. Since MACSJ1149 has a complex geometry, replacing its four main halos with a single spherical halo can alter significantly the morphology of primary critical lines. This is evident in Fig. 5.15, in which the pale blue band shows the large spread in Einstein radii found in simulations.

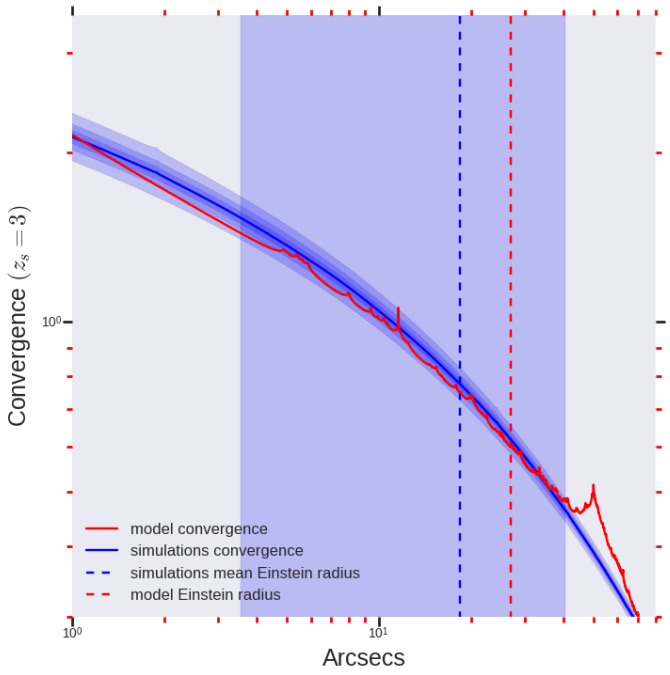

FIGURE 5.15: Comparison between the convergence radial profile of the reference model of MACSJ1149 (red solid line) and of the unconstrained simulations (blue, solid line: mean profile; shaded blue bands: 68%,95% and 100% intervals). Vertical, red, dashed line indicates the circularized Einstein radius of the model, calculated as $R_E = \sqrt{S/\pi}$, where S is the area of the primary critical line. The vertical, blue, dashed line and the vertical blue band indicate respectively the mean value and the full interval covered by the same quantity in simulations.

The cross-section of unconstrained clusters (Fig. 5.16, magenta bands) is slightly smaller than in the constrained case, suggesting that the radial distribution of substructures has a significantly higher impact on the total cross section than the shape of the main halo.

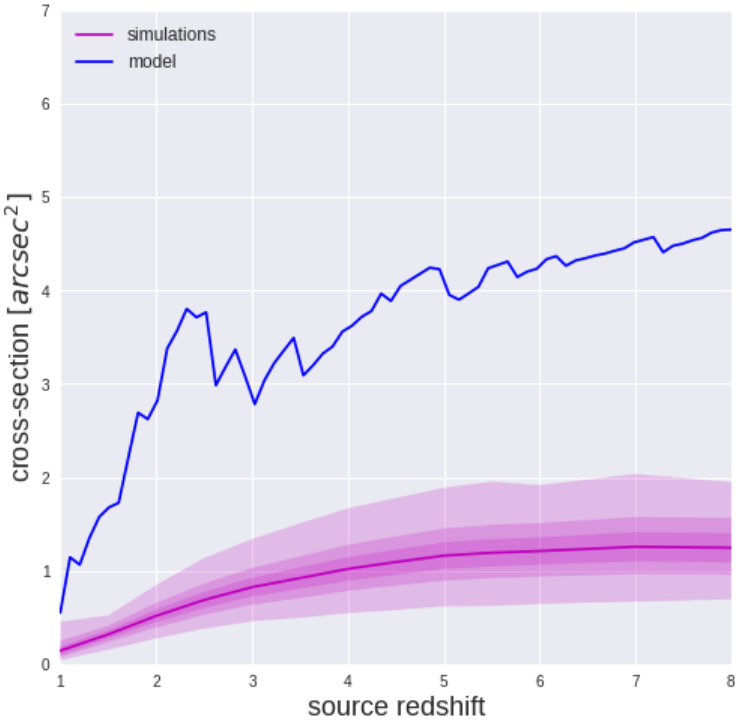

FIGURE 5.16: Measured galaxy-galaxy strong lensing cross-section of the reference model of MACSJ1149 (blue line) and of unconstrained simulations (magenta). Bands of different hues indicates the 68%, 95% and 100% intervals. The dark magenta line is the mean value of the measured cross section in simulations.

5.7 Expected number of GGSL events

The previous results rely on the accuracy of the reference strong lensing model of MACSJ1149 by Kawamata et al., 2016. A simple validation test of this model is to verify if the expected number of observable GGSL events in this cluster is consistent with observations.

In order to calculate the number of expected GGSL events in a particular cluster, we need to know the distribution of sources both in redshift and in magnitude and to account for the magnification effect of the cluster. More precisely, the number N_{gg} of observable GGSL events involving sources at redshift z_s with magnified magnitude m_μ is given by the product of the GGSL cross-section and the number density of sources at redshift z_s with magnified magnitude m_μ. The latter quantity is obtained from the unlensed distribution of sources N_s at redshift z_s taking into account the two contrasting effect induced by the presence of the cluster lens. First, the lens "bright up" sources, that is it amplifies their fluxes bringing faint sources above the observational flux limit. We describe this effect through the magnification probability distribution $P(\mu, z_s)$. Second, since the magnification amplify not only the sources but also the area in between them, the number density of source is diluted. We describe this effect through the function $f(z_s)$. The net effect is called *magnification bias*. Summarizing, the number N_{gg} of observable GGSL events is given

by

$$N_{gg}(z_s, m_\mu) = \sigma_{gg}(z_s)\frac{N_{ls}(z_s, m_\mu)}{A} \tag{5.5a}$$

$$= \sigma_{gg}(z_s)\frac{N_s(z_s, m)}{A} * P(\mu, z_s) * f(z_s) \tag{5.5b}$$

where $N_{ls}(z_s, m_\mu)$ is the number of lensed sources at redshift z_s with amplified magnitude m_μ observed in a portion of the sky of area A. A more precise description of the functions $f(z_s)$ and $P(\mu, z_s)$ is given in the next sections.

5.7.1 Calculation for MACSJ1149

We calculate the GGSL cross-section σ_{gg} of MACSJ1149 using the reference model by Kawamata et al., 2016. Since we do not know the true, unlensed source distribution behind MACSJ1149, we have to assume one on the basis of existing galaxy survey data. In order to do meaningful comparison with CLASH observations (limiting magnitude ≈ 27.5 in the F814W band), we need to apply the magnification probability distribution to a deep catalog like the Hubble Ultra Deep Field (HUDF) catalog (Rafelski et al., 2015, Fig. 5.17), which has a limiting magnitude of 29.5 in the HST F775W band (effective wavelength of 7693 Å). Unfortunately, HUDF has a very small field (11.4 arcmin^2 only) so it is likely affected by cosmic variance. The wide-field survey COSMOS (1.73 deg^2) (Ilbert et al., 2009, Fig. 5.18) is much wide, but the photometric redshift catalog has a limiting magnitude of ≈ 25 only (Subaru i^+ band, effective wavelength of 7629 Å).

In order to exploit both the dept of HUDF and the width of the COSMOS field, we have decided to combine them. If one simply correct the HUDF counts accounting for the smaller field finds, for $m < 25$ and $z > 0.544$, $\approx 22\%$ less galaxies with respect to COSMOS. Due to the greater robustness of COSMOS counts, we re-sample the HUDF catalog in order to match the COSMOS magnitude distribution. In particular, we describe the COSMOS magnitude distribution using the fitting functional

$$N(m) = B \times 10^{A \times m} \tag{5.6}$$

as done by Leauthaud et al., 2007 for $20 < i^+ < 26$, and extending it down to the HUDF magnitude limit. Here N has units of number deg^{-2} 0.5 mag^{-1}, $A = 0.332$ and $\log B = -3.543$. Thus, in each magnitude bin between $25 < m < 29.5$ we adjust the number of the HUDF sources randomly sampling the observed distribution and replicating the extracted sources. In this way, we construct the redshift and magnitude distribution of unlensed sources $N_s(z_s, m)$. The left panel of Fig. 5.19 shows the magnitude distribution of all sources in this new catalog, irrespective of their redshift, compared to the functional in Eq. 5.6.

The magnification probability $P(\mu, z_s)$ is obtained from maps of magnification on the source plane. The magnification on the source plane does not coincide with the magnification on the image plane defined in (2.26): the former is the total magnification of the source flux, while the latter describes the magnification of each image of the source. The magnification on the source plane can be derived from the magnification on the lens plane tracing light rays back to the source plane and adding up magnifications relative to all images of the same source. We derive maps of this quantity for the reference model of MACSJ1149, for different redshifts of the source plane, using a *FORTRAN* code. Then, $P(\mu, z_s)$ is simply given by the fraction of

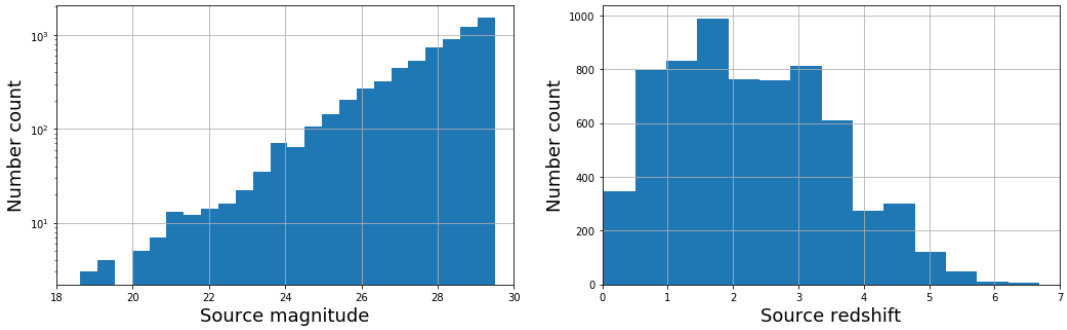

FIGURE 5.17: Hubble Ultra Deep Field catalog. Left: magnitude distribution of detected sources. Right: redshift distribution of detected sources.

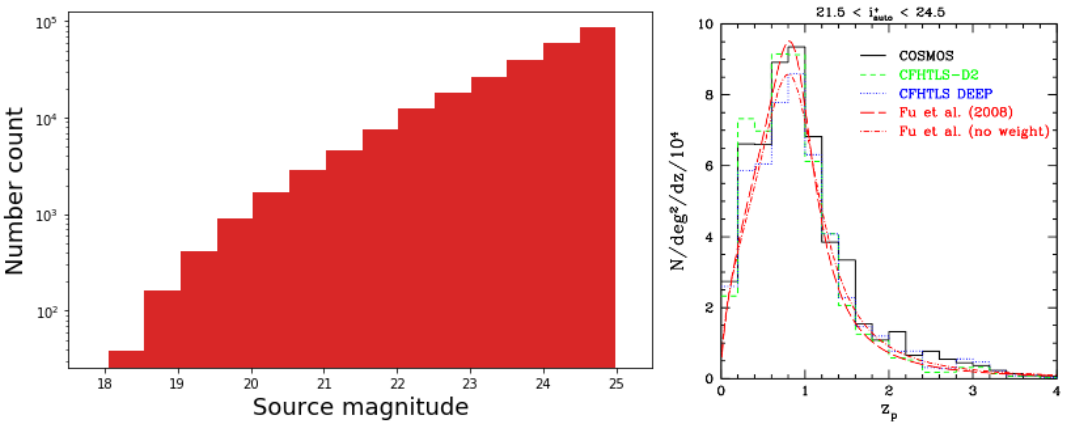

FIGURE 5.18: COSMOS photometric catalog. Left: magnitude distribution of detected sources. Right: photometric redshift distribution of detected sources (black solid line) from Ilbert et al., 2009.

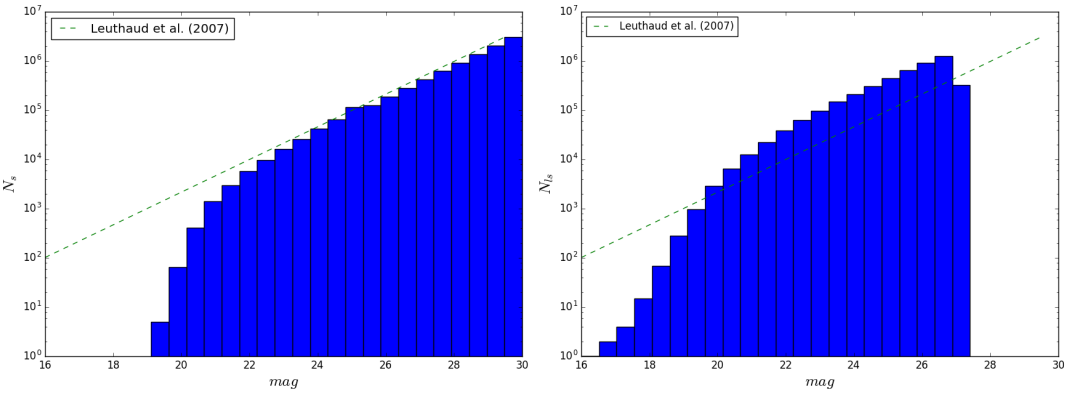

FIGURE 5.19: Magnitude distribution of sources in the unlensed (left) and lensed (right) "COSMOS+HUDF" catalog obtained considering the lensing properties of MACSJ1149, as explained in the text. The dashed line is the fitting functional (5.6) used to construct the unlensed catalog for $mag > 25$.

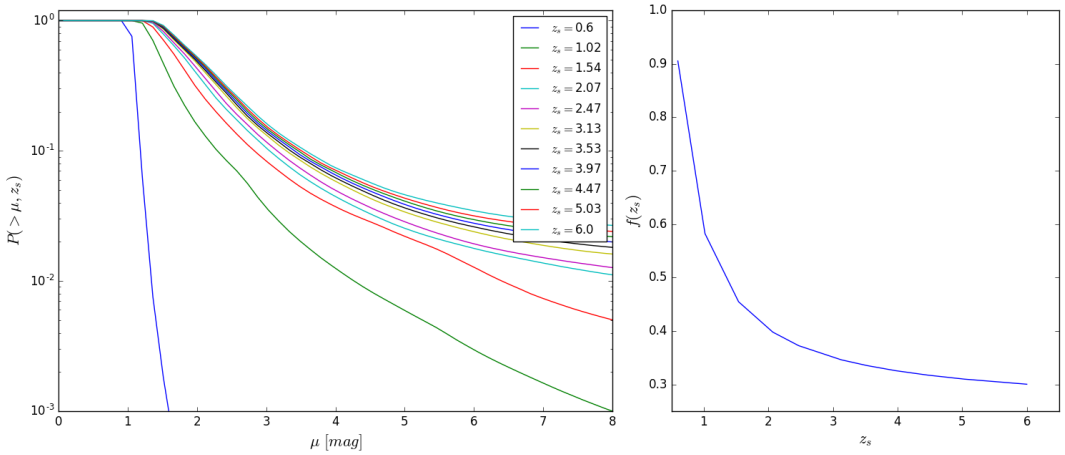

FIGURE 5.20: Left: probability to have a source magnified more than μ for different values of source redshift z_s. Right: fraction of the source plane f mapped into the observed lens plane, for different source plane redshifts z_s. Both panels are relative to MACSJ1149.

pixels with magnification μ in the map calculated for the source redshift z_s. The left panel of Fig. 5.28 displays $P(>\mu, z_s) = \int_{\mu}^{\infty} P(\mu, z_s)d\mu$. A random sampling of this probability distribution allows us to assign a new, amplified magnitude to each source in the combined COSMOS+HUDF catalog, thus obtaining the lensed sources magnitude distribution. As shown in the right panel of Fig.5.19, the high lensing power of MACSJ1149 amplifies almost all considered sources up to magnitudes ≈ 27.5, the value we take as the lower limit for detection. If we had a deeper unlensed catalog, probably more faint sources would be brightened up above this limit. For this reason, our calculation will give a lower limit to the number of expected GGSL events.

The function $f(z_s)$ can be easily estimated by the same maps of magnification on the source plane as

$$f(z_s) = \frac{A_s(z_s)}{A} \tag{5.7}$$

where A is the area of the observed portion of the sky and A_s is the corresponding area on the source plane. We considered a region of $160 \times 160''$ centered on the cluster center. The behavior of f as a function of z_s is shown in the right panel of Fig. 5.20. Some examples of magnification maps are shown in Fig. 5.29.

Now it is possible to apply (5.5b) and calculate the number of expected observable GGSL events in a CLASH-like observation. Since we are interested in the total number of events, independently of source redshift and magnitude, we integrate N_{gg} over z and m, obtaining:

$$N_{tot} = \int_{0.544}^{6} dz_s \int_{0}^{27.5} dm_\mu N_{gg}(z_s, m_\mu) \approx 0.29. \tag{5.8}$$

MACSJ1149 hosts one known GGSL event, the one involving SN Refsdal described in Sect. 3.2.2. This result may indicate some defect in the considered lensing model, in particular in the assumed scaling relations used for substructures modeling (see Sect. 5.6.1). However this number has to be taken as a lower limit since, as explained before, the unlensed catalog we consider is not enough deep to correctly

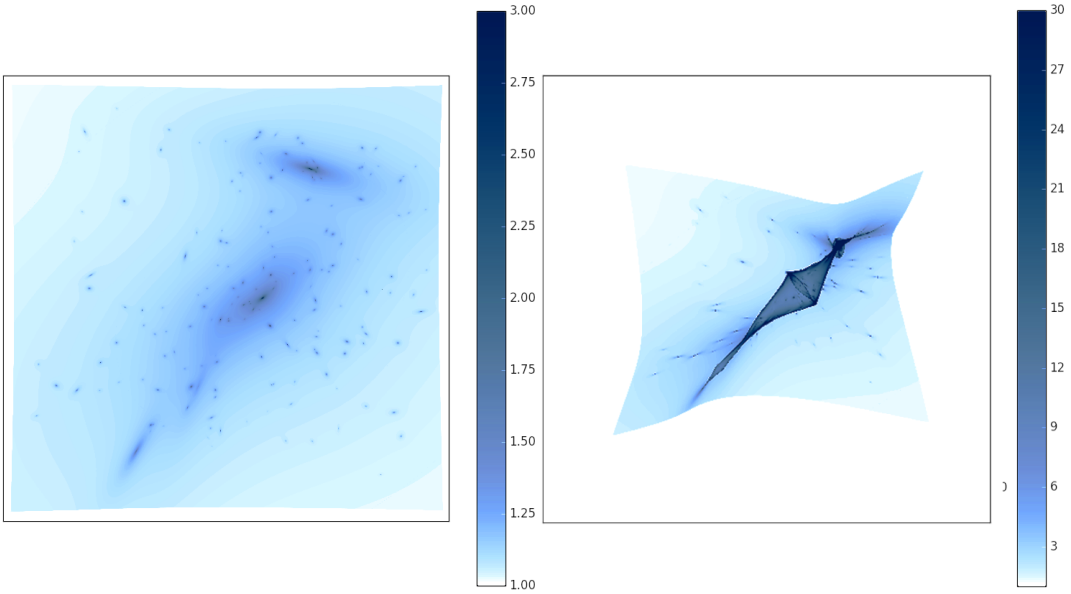

FIGURE 5.21: magnification on the source plane (left: $z_s = 0.6$; right: $z_s = 6.0$) for the cluster MACSJ1149. Higher magnifications arise at caustics. The white portion of the map near borders, clearly visible in the right panel, is the fraction 1-$f(z_s)$ of the source plane that is not visible to the observer due to lensing. In other words, only the remaining fraction f of the source plane is mapped into the observed field. On higher redshift source planes one has generally higher magnifications but lower values of f (see also Fig. 5.20). Both maps have sides of 160", centered on the cluster center.

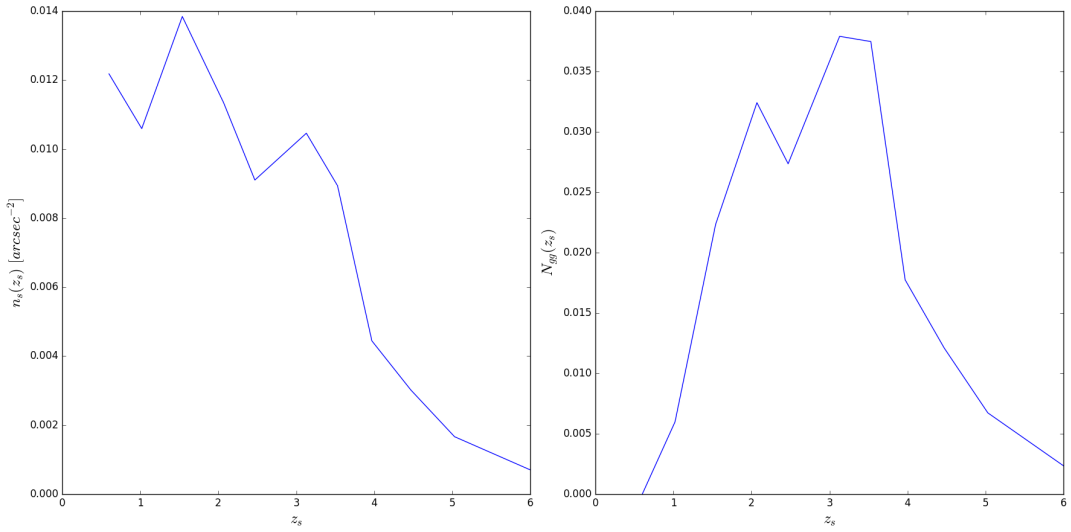

FIGURE 5.22: Left: number density of background sources derived applying the procedure described in the text to our COSMOS+HUDF catalog truncated at $mag \leqslant 27.5$. Right: number of expected GGSL events in MACSJ1206 in each source redshift bin. The anomaly at $z_s \approx 2.5$ reflects the redshift distribution of the HUDF catalog.

reproduce the density of sources with observable magnitude up to ≈ 27.5. Moreover, the reliability of the modeling approach used by Kawamata et al., 2016 was proven also by Meneghetti et al., 2016, who perform a comparison between different mass reconstruction algorithms. As displayed in Fig. 5.23, GLAFIC is one of the codes which better reproduces the true substructure mass distribution.

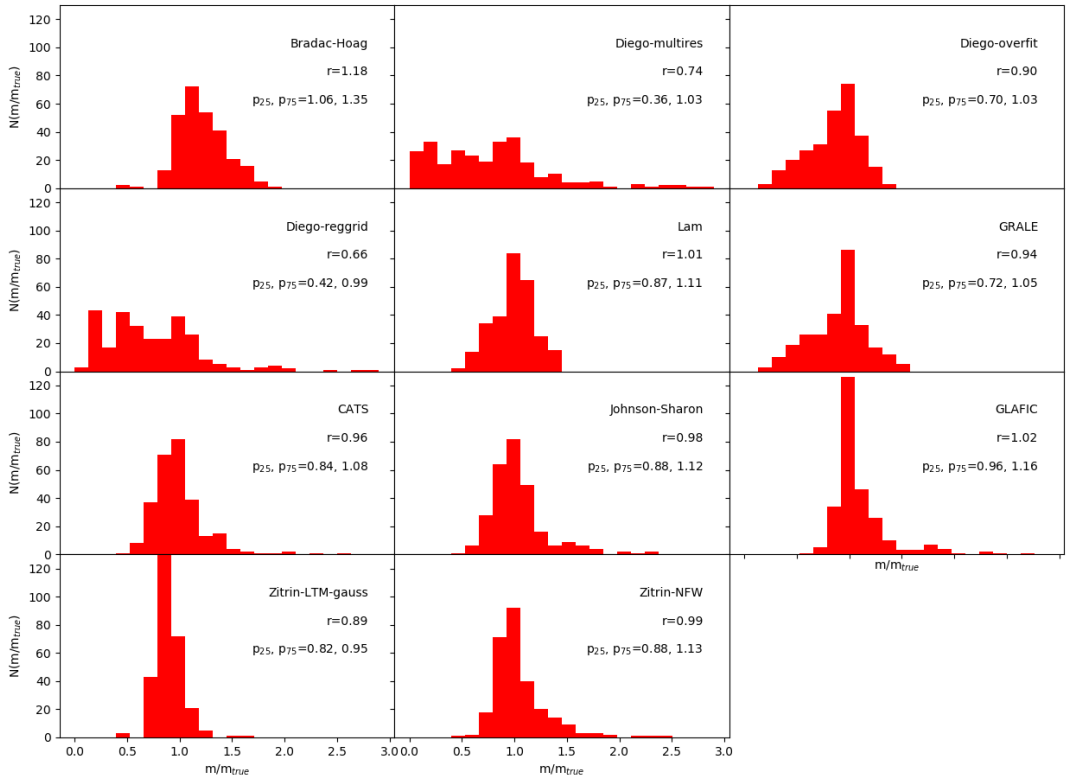

FIGURE 5.23: Comparison between different mass reconstruction algorithms (Meneghetti et al., 2016). Red histograms show the distributions of the ratios between reconstructed and true substructures masses. In each panel is shown the median r and the 25-th and 75-th percentiles of the distribution. The best algorithms are those with r close to unity and narrow distributions of m/m_{true}. The models relevant to our discussion are those labeled as "CATS" and "Johnson-Sharon", created with LENSTOOL, and the GLAFIC model.

5.7.2 Calculation for MACSJ1206

We have applied the same kind of test to the cluster MACSJ1206. This cluster (Fig. 5.24), discovered during the MAssive Cluster Survey (MACS, Ebeling, Edge, and Henry, 2001), is an X-Ray luminous cluster of galaxies located at coordinates $12:06:12.15$ (R.A.), $-08:48:03.4$ (Dec) and at redshift $z = 0.44$. As MACSJ1149, it was included in the CLASH survey (Postman et al., 2012). From the comprehensive analysis by Umetsu et al., 2016 (Fig 5.25), MACSJ1206 has a virial mass of $M_{vir} = 18.17 \pm 4.23 \times 10^{14} M_{\odot}$ and a concentration $c_{vir} = 3.7 \pm 1.1$ (reported as M_{200c} and c_{200c} by the authors). In this work, we take as reference model for MACSJ1206 the strong lensing model by Caminha et al. (in preparation).

The model, obtained with LENSTOOL code, consists of three large-scale PIEMD halos and 265 PIEMD substructures. Substructures were modeled using the following scaling relations, corresponding to a constant mass-to-light ratio:

$$\sigma_i = \sigma_* L_i^{1/4} \tag{5.9a}$$

$$r_{t,i} = r_{t,*} L_i^{1/2} \tag{5.9b}$$

$$r_{c,i} = r_{c,*} L_i^{1/2} \tag{5.9c}$$

where L_i are substructures measured luminosities and σ_i, $r_{t,i}$ and $r_{c,i}$ are substructures velocity dispersions and truncation and core radii. The best fit values for σ_* and $r_{t,*}$ are $\sigma_* = 280.472158$ km/s and $r_{t,*} = 3.015359''$; $r_{c,*}$ was set to $0.01''$. The model includes also an external shear due to the surrounding distribution of matter.

The procedure used to obtain the number of expected observable GGSL events in MACSJ1206 is the same described for MACSJ1149. We calculate the GGSL cross-section σ_{gg} of MACSJ1206 using the reference model by Caminha et al. (in preparation). The result is shown in Fig. 5.26, compared to the cross-section of the reference model of MACSJ1149. The lensed COSMOS+HUDF catalog magnitude distribution of sources is shown in the right panel of Fig. 5.27. The magnification probability distribution for this cluster is shown in Fig. 5.28, together with the function $f(z_s)$. Examples of magnification maps for this cluster are shown in Fig. 5.29. The resulting number of expected observable GGSL events in MACSJ1206 is

$$N_{tot} = \int_{0.440}^{6.0} dz_s \int_{0.0}^{27.5} dm_\mu N_{gg}(z_s, m_\mu) \approx 1.22. \tag{5.10}$$

MACSJ1206 hosts at least 2 GGSL events (see Sect. 3.2.2) thus, similarly to what found for MACSJ1149, the model predicts a smaller number of observable GGSL events than observed. This fact may indicate some error in the modeling procedure, like the assumption of a constant mass-to-light ratio for galaxies. However, as for MACSJ1149, some inaccuracy could come from the method we employed to construct our COSMOS+HUDF catalog. The good performances of LENSTOOL in cluster modeling was proved by Meneghetti et al., 2016, as shown in Fig. 5.23.

FIGURE 5.24: True color image of the cluster MACS1206, obtained from HST data collected during the CLASH survey (credits: NASA/ESO).

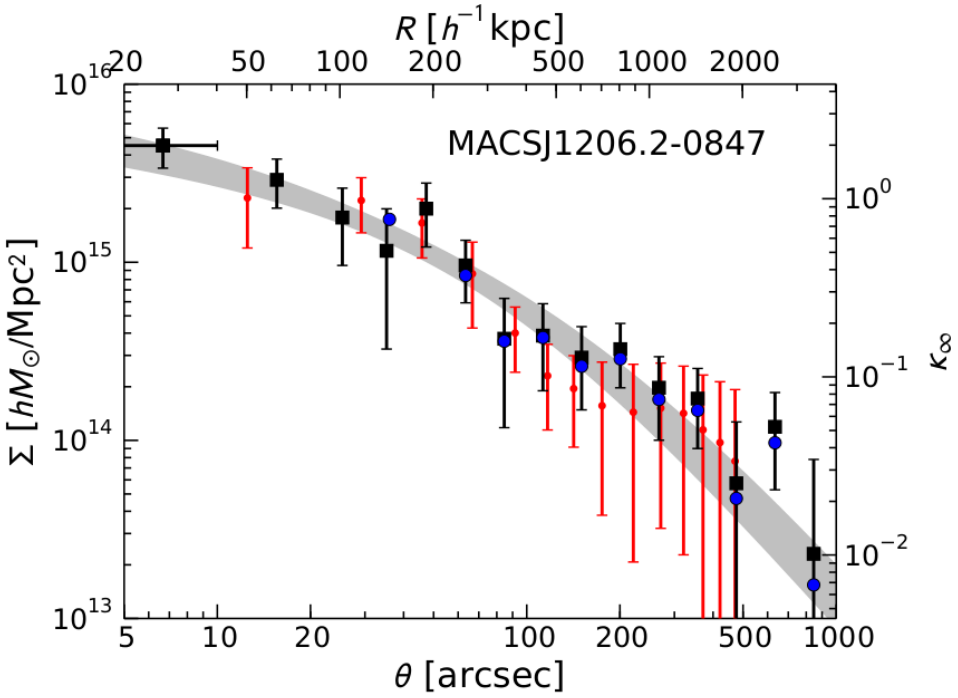

FIGURE 5.25: Surface mass density profile of MACSJ1206 derived by Umetsu et al., 2016 from a joint analysis of HST strong/weak-shear lensing and ground-based weak shear/magnification lensing data (black squares). Red dots are relative to the lensing model by Merten et al., 2015. Error bars represent the 1σ uncertainty. The gray area shows the best-fit NFW profile (1σ uncertainty).

FIGURE 5.26: Galaxy-galaxy strong lensing cross-section for the reference models of MACSJ1206 (Caminha et al., in preaparation) and MACSJ1149 (Kawamata et al., 2016).

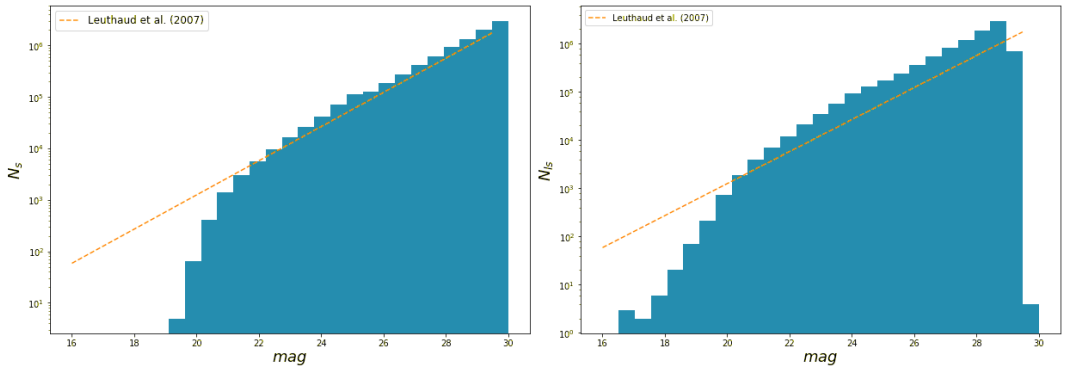

FIGURE 5.27: Magnitude distribution of sources in the unlensed (left) and lensed (right) "COSMOS+HUDF" catalog obtained considering the lensing properties of MACSJ1206, as explained in the text. The dashed line is the fitting functional (5.6) used to construct the unlensed catalog for $mag > 25$.

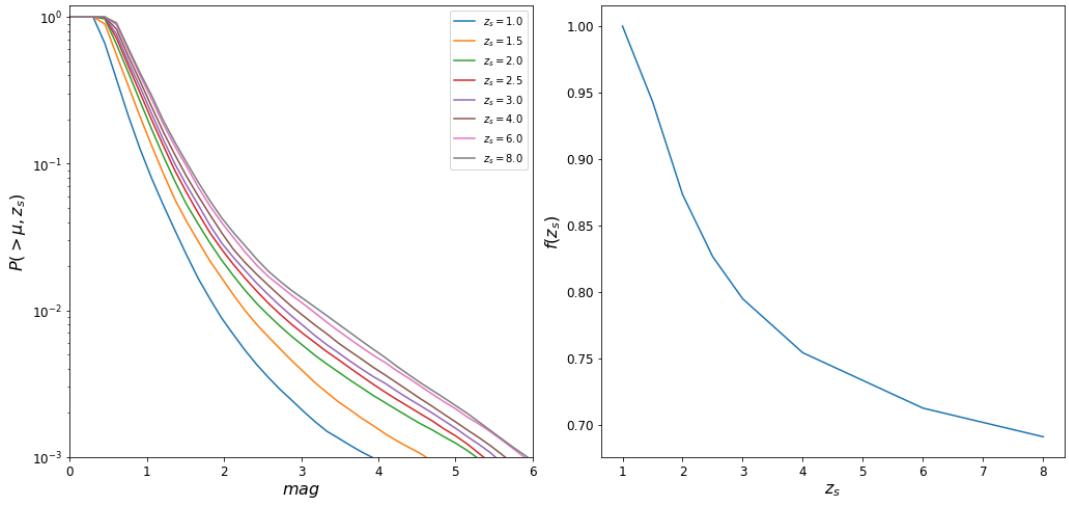

FIGURE 5.28: Left: probability to have a source magnified more than μ for different values of source redshift z_s. Right: fraction of the source plane f mapped into the observed lens plane, for different source plane redshifts z_s. Both panels are relative to MACSJ1206.

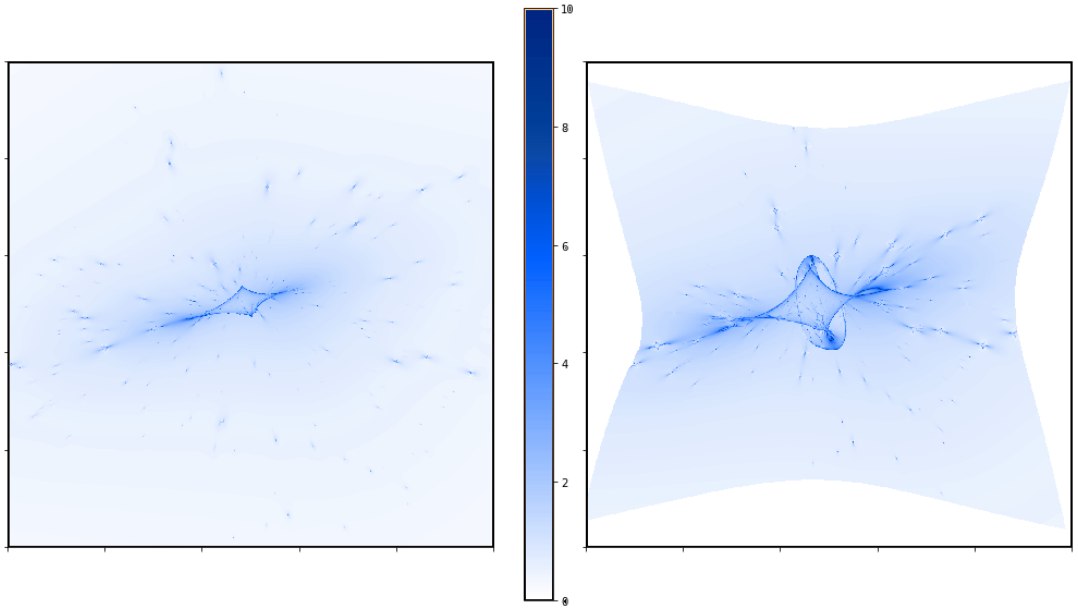

FIGURE 5.29: magnification on the source plane (left: $z_s = 1.0$; right: $z_s = 8.0$) for the cluster MACSJ1206. Higher magnifications arise at caustics. The white portion of the map near borders, clearly visible in the right panel, is the fraction 1-$f(z_s)$ of the source plane that is not visible to the observer due to lensing. In other words, only the remaining fraction f of the source plane is mapped into the observed field. On higher redshift source planes one has generally higher magnifications but lower values of f (see also Fig. 5.28). Both maps have sides of 160″, centered on the cluster center.

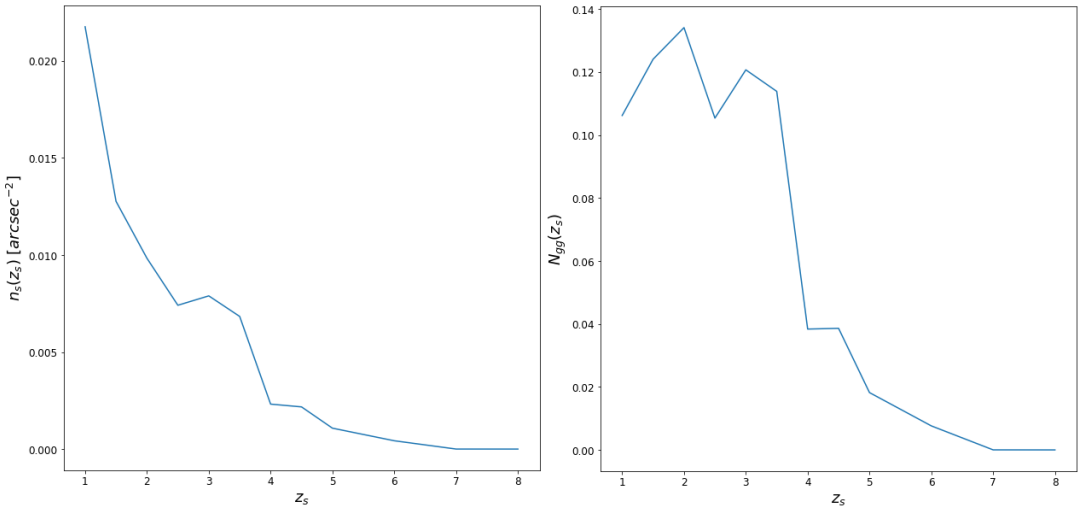

FIGURE 5.30: Left: number density of background sources derived applying the procedure described in the text to our COSMOS+HUDF catalog truncated at $mag \leqslant 27$. Right: number of expected GGSL events in MACSJ1206 in each source redshift bin. The anomaly at $z_s \approx 2.5$ reflects the redshift distribution of the HUDF catalog.

Chapter 6

Conclusions

Thanks to the availability of deep observations of massive galaxy clusters, like those provided by the CLASH and Frontier Fields surveys, several strong lensing events between a cluster member and a background source were discovered and studied in detail. Their characterization give us useful constraints for the mass modeling of the lens galaxy and of the whole cluster. However, in the state-of-the-art hydrodynamical simulations of galaxy clusters, the paucity of critical lines around substructures suggest that this kind of event is very rare. This apparent contrast between theory and observations is the reason which lead us to analyze the phenomenology of GGSL events in galaxy clusters. In particular, we studied how the physical properties of galaxy clusters affect the likelihood to observe GGSL events. We quantified this probability defining the GGSL cross-section as the area of tangential caustics formed by substructures. In fact, a source located inside such a tangential caustics is multiply imaged around a cluster member.

Firstly, we looked for a possible relation between the galaxy-galaxy strong lensing cross-section and the inner slope and concentration of the cluster mass profile. Then, we considered the subhalos mass function (SHMF) and radial distribution. In order to pursue our goal, we built simulated galaxy cluster varying the aforementioned physical parameters. This was possible using the softwares MOKA and LENSTOOL. Combining the capabilities of these two semi-analytic codes, it was possible to generate lensing maps of realistic clusters obeying the ΛCDM paradigm with arbitrary resolution, both spatial and in substructures mass. To measure the galaxy-galaxy strong lensing cross-section, we created a novel algorithm able to locate tangential critical lines around substructures (which we call "secondary critical lines"), map them onto the corresponding caustics and measure the area enclosed. The results obtained in this first part of the thesis can be summarized as follows.

- The largest contribution to the galaxy-galaxy strong lensing cross-section comes from massive substructures near, but outside, the main critical line of the cluster. Conversely, secondary critical lines inside the primary critical line can form only in particular situations, and the sizes of the corresponding caustics are always negligible in the computation of the cross section.
- The inner slope of the cluster mass profile influences the galaxy-galaxy strong lensing cross-section. In particular, fixing the cluster Einstein radius, shallower profiles favour the occurrence of galaxy-galaxy strong lensing events. In this case, substructures outside the Einstein radius are embedded in a higher convergence environment, which facilitates the creation of secondary critical lines.
- The halo concentration has a similar effect, although its amplitude is smaller.
- The galaxy-galaxy strong lensing cross-section is sensitive to the substructures mass function, and in particular to the high-masses cutoff. Clusters with less

massive substructures have a smaller cross-section, upholding what we said in the first point. Conversely, the cross-section does not show a clear dependence to the low-mass end of the subhalos mass function.

- The substructures radial distribution function has a larger impact on the cross-section. In clusters with more abundant substructures in the central regions it is more likely to observe galaxy-galaxy strong lensing events.

In the second part of the thesis we tested our the previous results on a real cluster: MACSJ1149. We took as reference a lensing model obtained exploiting CLASH and Frontier Field observation, and we measured its cross-section. Then we built several simulations of MACSJ1149 varying some properties with respect to the reference model. First, we substitute the observed subhalo mass function with the ΛCDM one. Second, we changed the positions of subhalos inside the cluster, using the radial distribution function found in cosmological simulations. Finally, we substitute the complex large scale dark matter distribution found in the modeling with a simple Navarro-Frenk-White dark matter halo. In all these three cases we measured the resulting cross-section. We found the following results.

- The difference between the observed subhalo mass function in MACSJ1149 (provided by the reference lensing model) and the standard ΛCDM SHMF used in simulations it is not enough to see a difference in the measured cross-sections.
- The observed radial distribution of substructures in the inner region of MACSJ1149 is notably different from what found in cosmological simulation for clusters of the same mass. Namely, our simulations of MACSJ1149, obtained using the same large-scale mass distribution of the reference model but positioning substructures following ΛCDM prescriptions, contain much less subhalos in the inner region. According to what previously discussed, our simulations exhibit a substantially smaller cross-section for GGSL.
- Substituting the large-scale mass distribution of the model with a single NFW halo we observe only a small decrease of the cross-section compared to the previous case. That is, in this case the shape of the large-scale dark matter distribution does not affect much the cross-section.

Finally, we use our method to check the validity of the reference model of MACSJ1149 and of an analogous strong lensing model of the cluster MACSJ1206. This has been done comparing the number of observable galaxy-galaxy strong lensing events predicted by models and the number of observed GGSL events. In order to complete this task, it was necessary to assume a distribution of sources behind the clusters and to calculate the magnification effect on these sources caused by the clusters themselves. The first issue was faced considering a combination of the COSMOS and Hubble Ultra Deep Field catalogs. Amplification maps on different source planes were calculated directly from the lensing maps of the clusters. From them we have extracted a magnification probability function that we applied to our sources catalog, finding a number density of sources with observed magnitude above a fixed observational limit. Multiplying this quantity by the clusters GGSL cross-section, we find a lower limit to the expected number of observable events. In both cases, models slightly underestimate the number of events. This fact may indicate some defect in the modeling procedure, for example in the scaling relations assumed for substructures. However, also the combination of the COSMOS and HUDF catalogs

and the procedure of magnification of sources fluxes are not exempt from uncertainties.

Given the simplicity and the flexibility of our novel algorithm (the cross-section calculations needs deflection angles maps only) we expect to be able, in the near future, to apply a similar analysis to all CLASH and Frontier Fields clusters, extending our study to a more statistically significant sample of clusters.

Bibliography

Abell, G. O. (1958). "The Distribution of Rich Clusters of Galaxies." In: *Astrophysical Journal Supplement* 3, p. 211. DOI: 10.1086/190036.

Bahcall, Neta A. (1999). *Formation of structure in the universe*. Cambridge University Press.

Barnabè, M. et al. (2011). "Two-dimensional kinematics of SLACS lenses - III. Mass structure and dynamics of early-type lens galaxies beyond $z\sim0.1$". In: *Monthly Notices of the Royal Astronomical Society* 415, pp. 2215–2232. DOI: 10.1111/j.1365-2966.2011.18842.x. arXiv: 1102.2261.

Bartelmann, Matthias (1996). "Arcs from a universal dark-matter halo profile". In: *Astronomy and Astrophysics* 313, pp. 697–702. URL: http://adsabs.harvard.edu/abs/1996A%26A...313..697B.

Bartelmann, Matthias and Peter Schneider (1999). "Weak Gravitational Lensing". In: *arXiv*. URL: https://arxiv.org/pdf/astro-ph/9912508v1.pdf.

Berry, Michael V. (1989). *Principles of Cosmology and Gravitation*. IOP Publishing.

Biviano, A. et al. (2013). "CLASH-VLT: The mass, velocity-anisotropy, and pseudo-phase-space density profiles of the z = 0.44 galaxy cluster MACS J1206.2-0847". In: *Astronomy and Astrophysics* 558, A1, A1. DOI: 10.1051/0004-6361/201321955. arXiv: 1307.5867.

Bradley, L. D. et al. (2014). "CLASH: A Census of Magnified Star-forming Galaxies at z ˜ 6-8". In: *Astrophysical Journal* 792, 76, p. 76. DOI: 10.1088/0004-637X/792/1/76. arXiv: 1308.1692.

Caminha, G. B. et al. (2016). "A refined mass distribution of the cluster MACS J0416.1−2403 from a new large set of spectroscopic multiply lensed sources". In: *ArXiv e-prints*. arXiv: 1607.03462.

Cappellari, M. et al. (2015). "Small Scatter and Nearly Isothermal Mass Profiles to Four Half-light Radii from Two-dimensional Stellar Dynamics of Early-type Galaxies". In: *Astrophysical Journal Letters* 804, L21, p. L21. DOI: 10.1088/2041-8205/804/1/L21. arXiv: 1504.00075.

Cavaliere, A. and R. Fusco-Femiano (1976). "X-rays from hot plasma in clusters of galaxies". In: *Astronomy and Astrophysics* 49, pp. 137–144.

Dalal, N. and C. S. Kochanek (2002). "Direct Detection of Cold Dark Matter Substructure". In: *Astrophysical Journal* 572, pp. 25–33. DOI: 10.1086/340303. eprint: astro-ph/0111456.

Diaferio, A. and M. J. Geller (1997). "Infall Regions of Galaxy Clusters". In: *Astrophysical Journal* 481, pp. 633–643. DOI: 10.1086/304075. eprint: astro-ph/9701034.

Diego, J. M. et al. (2016). "A free-form prediction for the reappearance of supernova Refsdal in the Hubble Frontier Fields cluster MACSJ1149.5+2223". In: *Monthly Notices of the Royal Astronomical Society* 456, pp. 356–365. DOI: 10.1093/mnras/stv2638. arXiv: 1504.05953.

Dressler, A. (1980). "Galaxy morphology in rich clusters - Implications for the formation and evolution of galaxies". In: *Astrophysical Journal* 236, pp. 351–365. DOI: 10.1086/157753.

Ebeling, H., A. C. Edge, and J. P. Henry (2001). "MACS: A Quest for the Most Massive Galaxy Clusters in the Universe". In: *Astrophysical Journal* 553, pp. 668–676. DOI: 10.1086/320958. eprint: astro-ph/0009101.

Elíasdóttir, Á. et al. (2007). "Where is the matter in the Merging Cluster Abell 2218?" In: *ArXiv e-prints*. arXiv: 0710.5636.

Ettori, S. et al. (2010). "Mass profiles and c-M_{DM} relation in X-ray luminous galaxy clusters". In: *Astronomy and Astrophysics* 524, A68, A68. DOI: 10.1051/0004-6361/201015271.

Gao, L. et al. (2004). "The subhalo populations of ΛCDM dark haloes". In: *Monthly Notices of the Royal Astronomical Society* 355, 819–834. URL: http://adsabs.harvard.edu/abs/2004MonthlyNoticesoftheRoyalAstronomicalSociety.355..819G.

Gao, L. et al. (2012). "The Phoenix Project: the dark side of rich Galaxy clusters". In: *Monthly Notices of the Royal Astronomical Society* 425, pp. 2169–2186. DOI: 10.1111/j.1365-2966.2012.21564.x. arXiv: 1201.1940 [astro-ph.CO].

Giocoli, C. et al. (2010). "The substructure hierarchy in dark matter haloes". In: *Monthly Notices of the Royal Astronomical Society* 404, pp. 502–517. DOI: 10.1111/j.1365-2966.2010.16311.x. arXiv: 0911.0436.

Giocoli, Carlo et al. (2012). "MOKA: a new tool for strong lensing studies". In: *Monthly Notices of the Royal Astronomical Society* 421, 3343–3355.

Grillo, C. et al. (2014). "CLASH: Extending Galaxy Strong Lensing to Small Physical Scales with Distant Sources Highly Magnified by Galaxy Cluster Members". In: *Astrophysical Journal* 786, 11, p. 11. DOI: 10.1088/0004-637X/786/1/11. arXiv: 1403.0573.

Grillo, C. et al. (2015). "CLASH-VLT: Insights on the Mass Substructures in the Frontier Fields Cluster MACS J0416.1-2403 through Accurate Strong Lens Modeling". In: *Astrophysical Journal* 800, 38, p. 38. DOI: 10.1088/0004-637X/800/1/38. arXiv: 1407.7866.

Hezaveh, Y. D. et al. (2016). "Detection of Lensing Substructure Using ALMA Observations of the Dusty Galaxy SDP.81". In: *Astrophysical Journal* 823, 37, p. 37. DOI: 10.3847/0004-637X/823/1/37. arXiv: 1601.01388.

Ilbert, O. et al. (2009). "Cosmos Photometric Redshifts with 30-Bands for 2-deg^2". In: *Astrophysical Journal* 690, pp. 1236–1249. DOI: 10.1088/0004-637X/690/2/1236. arXiv: 0809.2101.

Jaffe, A. H. et al. (2001). "Cosmology from MAXIMA-1, BOOMERANG, and COBE DMR Cosmic Microwave Background Observations". In: *Physical Review Letters* 86, pp. 3475–3479. DOI: 10.1103/PhysRevLett.86.3475. eprint: astro-ph/0007333.

Jing, Y.P. and Yasushi Suto (2002). "Triaxial Modeling of Halo Density Profiles with High-Resolution N-Body Simulations". In: *Astrophysical Journal* 574, pp. 538–553. URL: http://adsabs.harvard.edu/abs/2002AstrophysicalJournal...574..538J.

Jullo, E. et al. (2007). "A Bayesian approach to strong lensing modelling of galaxy clusters". In: *New Journal of Physics* 9, p. 447. DOI: 10.1088/1367-2630/9/12/447. arXiv: 0706.0048.

Jullo, Eric and Jean Paul Kneib (2009). "Multiscale cluster lens mass mapping - I. Strong lensing modelling". In: *Monthly Notices of the Royal Astronomical Society* 395, pp. 1319–1332.

Kaiser, N. and G. Squires (1993). "Mapping the dark matter with weak gravitational lensing". In: *Astrophysical Journal* 404, pp. 441–450. DOI: 10.1086/172297.

Kawamata, R. et al. (2016). "Precise Strong Lensing Mass Modeling of Four Hubble Frontier Field Clusters and a Sample of Magnified High-redshift Galaxies". In: *Astrophysical Journal* 819, 114, p. 114. DOI: 10.3847/0004-637X/819/2/114. arXiv: 1510.06400.

Keeton, C. R. (2001). "A Catalog of Mass Models for Gravitational Lensing". In: *ArXiv Astrophysics e-prints*. eprint: astro-ph/0102341.

Kelly, P. L. et al. (2015). "Multiple images of a highly magnified supernova formed by an early-type cluster galaxy lens". In: *Science* 347, pp. 1123–1126. DOI: 10.1126/science.aaa3350. arXiv: 1411.6009.

Kneib, J.-P. and P. Natarajan (2011). "Cluster lenses". In: *The Astronomy and Astrophysics Review* 19, 47, p. 47. DOI: 10.1007/s00159-011-0047-3. arXiv: 1202.0185 [astro-ph.CO].

Koopmans, L. V. E. et al. (2009). "The Structure and Dynamics of Massive Early-Type Galaxies: On Homology, Isothermality, and Isotropy Inside One Effective Radius". In: *Astrophysical Journal Letters* 703, pp. L51–L54. DOI: 10.1088/0004-637X/703/1/L51. arXiv: 0906.1349 [astro-ph.CO].

Leauthaud, A. et al. (2007). "Weak Gravitational Lensing with COSMOS: Galaxy Selection and Shape Measurements". In: *Astrophysical JournalS* 172, pp. 219–238. DOI: 10.1086/516598. eprint: astro-ph/0702359.

Lee, Dong-Wook and Sang-Joon Kim (2014). "The effective cross-sections of a lensing galaxy: singular isothermal sphere with external shear". In: *Monthly Notices of the Royal Astronomical Society* 443, pp. 328–342. URL: https://arxiv.org/pdf/1408.6611.pdf.

Lotz, J. M. et al. (2016). "The Frontier Fields: Survey Design". In: *ArXiv e-prints*. arXiv: 1605.06567.

Meneghetti, M. et al. (2014). "The MUSIC of CLASH: Predictions on the Concentration-Mass Relation". In: *Astrophysical Journal* 797, 34, p. 34. DOI: 10.1088/0004-637X/797/1/34. arXiv: 1404.1384.

Meneghetti, M. et al. (2016). "The Frontier Fields Lens Modeling Comparison Project". In: *ArXiv e-prints*. arXiv: 1606.04548.

Meneghetti, Massimo. *Introduction to Gravitational Lensing - Lecture scripts*. URL: http://www.ita.uni-heidelberg.de/~massimo/sub/Lectures/gl_all.pdf.

Merritt, D. (1984). "Relaxation and tidal stripping in rich clusters of galaxies. II. Evolution of the luminosity distribution". In: *Astrophysical Journal* 276, pp. 26–37. DOI: 10.1086/161590.

Merten, J. et al. (2015). "CLASH: The Concentration-Mass Relation of Galaxy Clusters". In: *Astrophysical Journal* 806, 4, p. 4. DOI: 10.1088/0004-637X/806/1/4. arXiv: 1404.1376.

Mollerach, Silvia and Esteban Roulet (2002). *Gravitational Lensing and Microlensing*. World Scientific.

Munari, E. et al. (2016). "Numerical Simulations Challenged on the Prediction of Massive Subhalo Abundance in Galaxy Clusters: The Case of Abell 2142". In: *Astrophysical Journal Letters* 827, L5, p. L5. DOI: 10.3847/2041-8205/827/1/L5. arXiv: 1607.01023.

Natarajan, P. et al. (2017). "Mapping substructure in the HST Frontier Fields cluster lenses and in cosmological simulations". In: *Monthly Notices of the Royal Astronomical Society* 468, pp. 1962–1980. DOI: 10.1093/mnras/stw3385. arXiv: 1702.04348.

Navarro, Julio F., Carlos S. Frenk, and Simon D.M. White (1995). "The Structure of Cold Dark Matter Halos". In: *arXiv*. URL: https://arxiv.org/abs/astro-ph/9508025.

Newman, A. B. et al. (2009). "The Distribution of Dark Matter Over Three Decades in Radius in the Lensing Cluster Abell 611". In: *Astrophysical Journal* 706, pp. 1078–1094. DOI: 10.1088/0004-637X/706/2/1078. arXiv: 0909.3527.

Newman, A. B. et al. (2011). "The Dark Matter Distribution in A383: Evidence for a Shallow Density Cusp from Improved Lensing, Stellar Kinematic, and X-ray Data". In: *Astrophysical Journall* 728, L39, p. L39. DOI: 10.1088/2041-8205/728/2/L39. arXiv: 1101.3553.

Ogrean, G. A. et al. (2016). "Frontier Fields Clusters: Deep Chandra Observations of the Complex Merger MACS˜J1149.6+2223". In: *Astrophysical Journal* 819, 113, p. 113. DOI: 10.3847/0004-637X/819/2/113. arXiv: 1603.06010.

Oguri, Masamune (2010). "The Mass Distribution of SDSS J1004+4112 Revisited". In: *Publ. Astron. Soc. Japan*.

Ostriker, J. P. and M. A. Hausman (1977). "Cannibalism among the galaxies - Dynamically produced evolution of cluster luminosity functions". In: *Astrophysical Journal Letters* 217, pp. L125–L129. DOI: 10.1086/182554.

Padmanabhan, T. (2002). "Cosmological Constant - The Weight of the Vacuum". In: *arXiv*. URL: https://ned.ipac.caltech.edu/level5/Sept02/Padmanabhan/paper.pdf.

Parry, W. G. et al. (2016). "Dark matter fraction of low-mass cluster members probed by galaxy-scale strong lensing". In: *Monthly Notices of the Royal Astronomical Society* 458, pp. 1493–1503. DOI: 10.1093/mnras/stw298. arXiv: 1602.02753.

Peter Coles, Francesco Lucchin (2002). *Cosmology - The Origin and Evolution of Cosmic Structure*. John Wiley & Sons.

Planck Collaboration et al. (2016). "Planck 2015 results. XIII. Cosmological parameters". In: *AAP* 594, A13, A13. DOI: 10.1051/0004-6361/201525830. arXiv: 1502.01589.

Polisensky, E. and M. Ricotti (2011). "Constraints on the dark matter particle mass from the number of Milky Way satellites". In: *Physical Review D* 83.4, 043506, p. 043506. DOI: 10.1103/PhysRevD.83.043506. arXiv: 1004.1459 [astro-ph.CO].

Postman, M. et al. (2012). "The Cluster Lensing and Supernova Survey with Hubble: An Overview". In: *Astrophysical Journals* 199, 25, p. 25. DOI: 10.1088/0067-0049/199/2/25. arXiv: 1106.3328.

Rafelski, M. et al. (2015). "UVUDF: Ultraviolet Through Near-infrared Catalog and Photometric Redshifts of Galaxies in the Hubble Ultra Deep Field". In: *AJ* 150, 31, p. 31. DOI: 10.1088/0004-6256/150/1/31. arXiv: 1505.01160.

Rasia, E. et al. (2015). "Cool Core Clusters from Cosmological Simulations". In: *Astrophysical Journal Letters* 813, L17, p. L17. DOI: 10.1088/2041-8205/813/1/L17. arXiv: 1509.04247.

Riess, A. G. et al. (1998). "Observational Evidence from Supernovae for an Accelerating Universe and a Cosmological Constant". In: *AJ* 116, pp. 1009–1038. DOI: 10.1086/300499. eprint: astro-ph/9805201.

Rines, K. and A. Diaferio (2006). "CIRS: Cluster Infall Regions in the Sloan Digital Sky Survey. I. Infall Patterns and Mass Profiles". In: *The Astronomical Journal* 132, pp. 1275–1297. DOI: 10.1086/506017. eprint: astro-ph/0602032.

Rosati, P., S. Borgani, and C. Norman (2002). "The Evolution of X-ray Clusters of Galaxies". In: *Annual Review of Astronomy and Astrophysics* 40, pp. 539–577. DOI: 10.1146/annurev.astro.40.120401.150547. eprint: astro-ph/0209035.

Sand, D. J. et al. (2004). "The Dark Matter Distribution in the Central Regions of Galaxy Clusters: Implications for Cold Dark Matter". In: *Astrophysical Journal* 604, pp. 88–107. DOI: 10.1086/382146. eprint: astro-ph/0309465.

Schneider, P., J. Ehlers, and E. E. Falco (1992). *Gravitational Lenses*, p. 112. DOI: 10.1007/978-3-662-03758-4.

Treu, T. et al. (2015). "The Grism Lens-Amplified Survey from Space (GLASS). I. Survey Overview and First Data Release". In: *Astrophysical Journal* 812, 114, p. 114. DOI: 10.1088/0004-637X/812/2/114. arXiv: 1509.00475.

Treu, T. et al. (2016). ""Refsdal" Meets Popper: Comparing Predictions of the Reappearance of the Multiply Imaged Supernova Behind MACSJ1149.5+2223". In: *Astrophysical Journal* 817, 60, p. 60. DOI: 10.3847/0004-637X/817/1/60. arXiv: 1510.05750.

Umetsu, K. et al. (2016). "CLASH: Joint Analysis of Strong-lensing, Weak-lensing Shear, and Magnification Data for 20 Galaxy Clusters". In: *Astrophysical Journal* 821, 116, p. 116. DOI: 10.3847/0004-637X/821/2/116. arXiv: 1507.04385.

Umetsu, Keiichi (2010). "Weak Gravitational Lensing". In: *arXiv*. URL: https://arxiv.org/pdf/1002.3952.pdf.

Vegetti, S. and M. Vogelsberger (2014). "On the density profile of dark matter substructure in gravitational lens galaxies". In: *Monthly Notices of the Royal Astronomical Society* 442, pp. 3598–3603. DOI: 10.1093/mnras/stu1284. arXiv: 1406.1170.

Vegetti, S. et al. (2010). "Detection of a dark substructure through gravitational imaging". In: *Monthly Notices of the Royal Astronomical Society* 408, pp. 1969–1981. DOI: 10.1111/j.1365-2966.2010.16865.x. arXiv: 0910.0760.

Vegetti, S. et al. (2012). "Gravitational detection of a low-mass dark satellite galaxy at cosmological distance". In: *Nature* 481, pp. 341–343. DOI: 10.1038/nature10669. arXiv: 1201.3643.

Wang, L. et al. (2006). "Modelling galaxy clustering in a high-resolution simulation of structure formation". In: *Monthly Notices of the Royal Astronomical Society* 371, pp. 537–547. DOI: 10.1111/j.1365-2966.2006.10669.x. eprint: astro-ph/0603546.

Weinberg, D. H. et al. (2015). "Cold dark matter: Controversies on small scales". In: *Proceedings of the National Academy of Science* 112, pp. 12249–12255. DOI: 10.1073/pnas.1308716112. arXiv: 1306.0913.

Weinberg, Steven (1972). *Gravitation and Cosmology - Principles and Applications of the General Theory of Relativity*. John Wiley & Sons.

Wyithe, J. S. B., E. L. Turner, and D. N. Spergel (2001). "Gravitational Lens Statistics for Generalized NFW Profiles: Parameter Degeneracy and Implications for Self-Interacting Cold Dark Matter". In: *Astrophysical Journal* 555. URL: http://iopscience.iop.org/article/10.1086/321437.

Zhao, D. H. et al. (2009). "Accurate Universal Models for the Mass Accretion Histories and Concentrations of Dark Matter Halos". In: *Astrophysical Journal* 707, p. 354. URL: http://adsabs.harvard.edu/abs/2009AstrophysicalJournal...707..354Z.

Zitrin, A. et al. (2015). "Hubble Space Telescope Combined Strong and Weak Lensing Analysis of the CLASH Sample: Mass and Magnification Models and Systematic Uncertainties". In: *Astrophysical Journal* 801, 44, p. 44. DOI: 10.1088/0004-637X/801/1/44. arXiv: 1411.1414.